2017

TURBULENT TRANSITION SIMULATION AND PARTICULATE CAPTURE MODELING WITH AN INCOMPRESSIBLE LATTICE BOLTZMANN METHOD

John R. Murdock
Michigan Technological University, jrmurdoc@mtu.edu

TURBULENT TRANSITION SIMULATION AND PARTICULATE CAPTURE MODELING WITH AN INCOMPRESSIBLE LATTICE BOLTZMANN METHOD

By

John R. Murdock

A DISSERTATION

Submitted in partial fulfillment of the requirements for the degree of

DOCTOR OF PHILOSOPHY

In Mechanical Engineering-Engineering Mechanics

MICHIGAN TECHNOLOGICAL UNIVERSITY

2017

This dissertation has been approved in partial fulfillment of the requirements for the Degree of DOCTOR OF PHILOSOPHY in Mechanical Engineering-Engineering Mechanics.

Department of Mechanical Engineering-Engineering Mechanics

Dissertation Advisor:	*Dr. Song-Lin Yang*
Committee Member:	*Dr. Franz X. Tanner*
Committee Member:	*Dr. Kazuya Tajiri*
Committee Member:	*Dr. Youngchul Ra*
Department Chair:	*Dr. William W. Predebon*

Dedication

To my wife

who provided the utmost support for this endeavor from the outset - without which I would neither be who I am nor would this work be what it is today.

Contents

List of Figures

List of Tables

Preface

Portions of this dissertation have been published, presented, or are currently in review or preparation for publication.

Chapter 4 presents a paper published in the *International Journal of Computational Engineering Research* titled "Alternative and explicit derivation of the lattice Boltzmann equation for the unsteady incompressible Navier-Stokes equation" [1]. The authors are Dr. Song-Lin Yang and John R. Murdock. Dr. Yang provided the initial literature review and guidance on numerical and mathematical techniques, as well as text editing and simulation review. John R. Murdock provided algorithm implementation and simulation, data analysis, final derivations, and paper creation and submission.

These same authors presented findings at *The Thirteenth International Conference on Mesoscopic Methods in Engineering and Science* titled "Applications and advantages of the newly derived definitive incompressible lattice Boltzmann equation" [2]. The division of contributions follow those of the previous paragraph. Data from this presentation appears in sections of chapters 4, 5, 6, and 7.

Chapter section 5.1 presents a paper published in *Advances in Applied Mathematics and Mechanics* titled "Transition flow with an incompressible lattice Boltzmann

method" [3]. The authors are John R. Murdock, Jacob C. Ickes, and Dr. Song-Lin Yang. The iLBE basis for this study comes from research by John R. Murdock and Dr. Song-Lin Yang described in the first paragraph of this preface. Algorithm development for the base LBM simulation was performed by John R. Murdock, while Jacob C. Ickes developed the majority of data output and statistical post-processing algorithms and implementation. Both developed the research objectives and design of numerical experiments. Jacob C. Ickes produced the majority of the text, and John R. Murdock and Dr. Song-Lin Yang provided editing and minor text additions.

Chapter 6 presents a paper published in the *ASME Journal of Fluids Engineering* titled "An efficient method of generating and characterizing filter substrates for lattice Boltzmann analysis" [4]. The authors are John R. Murdock, Aamir Ibrahim, and Dr. Song-Lin Yang. The iLBE basis for this study comes from research by John R. Murdock and Dr. Song-Lin Yang described in the first paragraph of this preface. Algorithm research and development as well as post processing was performed by John R. Murdock. Aamir Ibrahim developed the new semi-empirical model. These same authors both produced the text and data content, while Dr. Song-Lin Yang provided technical consultation and document editing additions.

Acknowledgments

Support from several people and organizations made this research work possible. I would like to thank all of them for their guidance and resources.

I would like to thank my advisor Dr. Song-Lin Yang for guiding me as well as representing my work to others with his resources, and in conjunction with Dr. Craig Friedrich, advocating for me. I would also like to thank my committee members Dr. Franz X. Tanner, Dr. Kazuya Tajiri, and Dr. Youngchul Ra for their time, intellectual challenges, and input.

Several MTU organizations were instrumental in providing efficient and necessary research tools. For many simulations the high-performance computing cluster *Superior* and its knowledgeable computing experts were essential. Additionally, I thank the graduate school for helping to professionally prepare and present my research work.

I would also like to thank my family for their unique contributions and support. My wife for temporarily sacrificing to give me the time. My grandfather for placing such importance and value on higher education. My father for sparking my interest in fluid and thermal sciences, and my mother for her continual encouragement in all of my pursuits.

Nomenclature

List of Abbreviations

BC	Boundary Condition
BFS	Backward Facing Step
BGK	Bhatnagar Gross Krook
CFD	Computational Fluid Dynamics
CHT	Conjugate Heat Transfer
CPU	Computer Processing Unit
CT	Computed Tomography
DDF	Double Distribution Function
DNS	Direct Numerical Simulation
DPF	Diesel Particulate Filter
EDF	Equilibrium Distribution Function
FDM	Finite Difference Method
FVM	Finite Volume Method
GB	Gebart Brinkmann
GK	Gebart Kubawara
GPGPU	General Purpose Graphics Processing Unit
LBE	Lattice Boltzmann Equation

iLBE	Incompressible Lattice Boltzmann Equation
LBM	Lattice Boltzmann Method
iLBM	Incompressible Lattice Boltzmann Method
LDC	Lid Driven Cavity
LES	Large Eddy Simulation
LGA	Lattice Gas Automata
MPI	Message Passing Interface
MRT	Multiple Relaxation Time
MS	Multi-Speed
Msu/s	Million site updates per second
MTU	Michigan Technological University
N-S	Navier-Stokes
OpenACC	Open Accelerators
OpenMP	Open Multi-Processing
PDE	Partial Differential Equation
PDF	Probability Distribution Function
PM	Particulate Matter
PMF	Probability Mass Function
PNNL	Pacific Northwest National Laboratory
POD	Proper Orthogonal Decomposition
RANS	Reynolds Averaged Navier Stokes

REV	Representative Elementary Volume
SGS	Subgrid Scale
SRS	Scale Resolving Simulation
SRT	Single Relaxation Time
SST	Shear Stress Transport
TDF	Triple Distribution Function
TFLOPS	Tera Floating Point Operations per Second
WALE	Wall Adapting Local Eddy Viscosity

List of Symbols

α	Thermal Diffusivity
β	Bulk Modulus
c	Lattice Velocity, $\frac{\delta x}{\delta t}$
$\boldsymbol{c}_i$	Lattice Velocity Vector Component
c_s	Lattice Speed of Sound
C_p	Pressure Coefficient
δ	Discrete Unit
D	Mass Diffusivity
D_p	Hydraulic Diameter
DdQq	d-Dimension, q-Velocity Discretization

ϵ	Turbulent Energy Dissipation
η	Kolmogorov Length Scale
f	Friction Factor
f_i	Distribution Function
κ	Permeability
k	Turbulent Kinetic Energy
Kn	Knudsen Number
$\boldsymbol{\xi}$	Continuous Velocity Space
$\mathbf{\Lambda}$	Collision Relaxation Time Matrix
m	Moment Distribution Function
Ma	Mach Number
ν	Kinematic Viscosity
ϕ	Porosity
Pe	Peclet Number
Pr	Prandtl Number
Ra	Rayleigh Number
Re, Re_L	Reynolds Number, characteristic length
Re_x	Reynolds Number, entrance length
R_h	Hydraulic Radius
ρ	Density
S_{ij}	Strain Rate Tensor

Sc	Schmidt Number
τ	Collision Relaxation Time
T	Temperature or Tortuosity
u	Velocity
w	Lattice Weight
Y	Species Mass Fraction
$\langle\rangle$	Ensemble Average

Abstract

Derivation of an unambiguous incompressible form of the lattice Boltzmann equation is pursued in this dissertation. Further, parallelized implementation in developing application areas is researched. In order to achieve a unique incompressible form which clarifies the algorithm implementation, appropriate ansatzes are utilized. Through the Chapman-Enskog expansion, the exact incompressible Navier-Stokes equations are recovered. In initial studies, fundamental 2D and 3D canonical simulations are used to evaluate the validity and application, and test the required boundary condition modifications. Several unique advantages over the standard equation and alternative forms found in literature are found, including faster convergence, greater stability, and higher fidelity for relevant flows.

Direct numerical simulation and large eddy simulation of transitional and chaotic flows are one application area explored with the derived incompressible form. A multiple relaxation time derivation is performed and implemented in a 2D cavity (direct simulation) and a 3D cavity (large eddy simulation). The Kolmogorov length scale, a function of Reynolds number, determines grid resolution in the 2D case. Comparison is made to the extensive literature on laminar flows and the Hopf bifurcation, and final transition to chaos is predicted. Steady and statistical properties in all cases are in good agreement with literature. In the 3D case the relatively new Vreman subgrid

model provides eddy viscosity modeling. By comparing the center plane to the direct numerical simulation case, both steady and unsteady flows are found to be in good agreement, with a coarse grid, including prediction of the Hopf bifurcation.

Multiphysics pore scale flow is the other main application researched here. In order to provide the substrate geometry, a straightforward algorithm is developed to generate random blockages producing realistic porosities and passages. Combined with advection-diffusion equations for conjugate heat transfer and soot particle transport, critical diesel particulate filtration phenomena are simulated. To introduce additional fidelity, a model is added which accounts for deposition caused by a variety of molecular and atomic forces.

Detailed conclusions are presented to lay the groundwork for future extensions and improvements. Predominantly, higher lattice velocity large eddy simulation, improved parallelization, and filter regeneration.

Keywords: incompressible flow; turbulent-transition; lattice Boltzmann method; porous media filtration; conjugate heat transfer; multiphase flow

Chapter 1

Introduction

Mathematical models of fluid motion can be categorized based on the length and time scales considered, namely molecular, mesoscopic, and macroscopic models. Historically, the most popular choice for simulation is the macroscopic scale, approximating fluid as a continuum through the Navier-Stokes (N-S) equations. In flows of interest the Knudsen number (Kn) is often low, yielding an accurate approximation to continuum [5]. However, flows which appear continuous are actually the result of molecular action. Microscopic models thus present a more fundamental picture, but also present unknowns on the order of 10^{23}, the scale of Avogadro's number relating the number of molecules to macroscopic levels. Between these extremes is the mesoscale described by kinetic theory. By approximating the flow as the collective statistical action of many molecules, scales smaller than the N-S equations can simulate are attainable

without the cost of individual molecule motion computation. Even for larger scale continuum flows the mesoscopic approach provides several unique benefits which will be expounded in chapter 3, which covers base methodology.

Kinetic theory is described by the Boltzmann equation, a first-order partial differential equation (PDE) [6]. While the N-S equations describe a branch of continuum mechanics which transports familiar macorscopic variables, the Boltzmann equation describes a branch of statistical mechanics and transports a probability distribution function (PDF). The Boltzmann equation can be discretized into the numerically solvable lattice Boltzmann equation (LBE), shown in chapter 3. The lattice Boltzmann method (LBM) is the mesoscopic method researched and applied in this work.

Turbulent transition simulation and diesel particulate filtration (DPF) modeling within the incompressible limit are the ultimate goals of this dissertation, for which the LBE will be modified, refined, and applied through novel research. Both fields are highly active due to the relative youth of the LBM, world-wide interest in carbonous particulate matter (PM) capture [7], and ubiquitous interest in turbulence [8].

1.1 Transition

Modeling approaches to turbulent transition must make large assumptions, resulting in limited capability [9]. Consequently, methodology which better facilitates a direct numerical simulation (DNS) or in high node counts a large eddy simulation (LES) of the process is worthy of study. Historically, the N-S equations have provided DNS and LES of incompressible flows based on Kolmogorov's theory of length scales and their relative importance. The expense of resolving all, or even the just the largest scales with a fine mesh is exacerbated by non-linearities and non-local computation. The LBM can reduce the computational cost by its linear nature and local computation. However, the standard LBE simulates compressible continuum flow. With modifications and clarifications to the LBE, the LBM is shown to be capable of incompressible continuum DNS and LES in contrast to previous literature.

With LES, in laminar flows, there must be a vanishing viscosity modifying sub-grid scale (SGS) model contribution, with the contribution increasing in transition and through to turbulence. Additionally, since flow near walls is in a low-Re regime, it is important the SGS contribution be limited near these boundaries automatically. Since LES in its most basic form, using the Smagorinsky-Lilly SGS model, requires a non-vanishing global model constant it is not suitable for transition. More recent SGS developments make LES a good candidate for transitional flows, and these will

be utilized.

1.2 Filtration

Accurate aftertreatment numerical simulations are essential to the rapid development of the most efficient and effective filtration. With increasing pressure placed on governments, industry, and research institutions to reduce dangerous emissions [7], it is difficult to overstate the importance of achieving efficient capture of carbonous PM, while also reducing engine fuel consumption. Literature on this type of numerical analysis has been increasing in response, but still leaves desirable improvements in the accuracy of transport phenomenon simulation. To advance the state of PM filter modeling, this work will produce a comprehensive code which can leverage parallel computing to integrate improvements to the LBE with existing models.

A PM filter, such as a cordierite DPF, has three fundamental scales. The largest scale is the honeycomb cordierite block placed inside of a flow control system. Next is the channel, which produces the honeycomb appearance. Flow may enter alternating channels, and exit the adjacent channel. Linking these channels is the smallest scale, the porous walls, where disordered passage distributions allow flow, but trap particles. A simplified schematic is presented in figure 1.1.

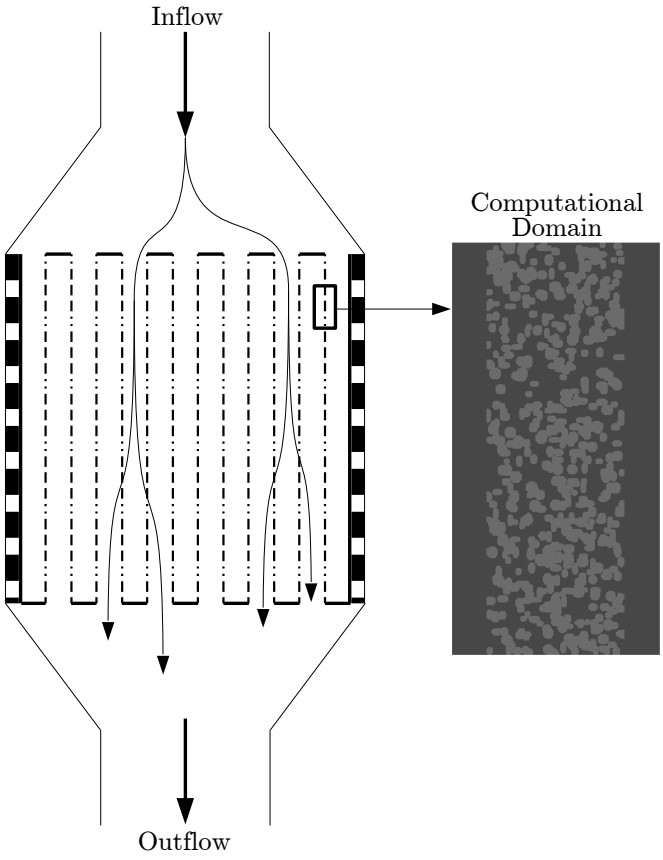

Figure 1.1: Schematic of DPF flow.

In a real device, there are hundreds of these alternating channels. The porous walls contain passages on the scale of tens of microns to tens of nanometers. Some pressure loss inevitably occurs, but the goal is to minimize this while maximizing PM sequestration. The computational domain of interest in this work is the wall detail. This representative sample can feed into solutions at the larger scale, all the way to the total device level.

0D and 1D aftertreatment models have long been the standard approach to DPF study. Bisset and Shadman, and researchers at MTU pioneered such models and

their development in the 1980's [10, 11]. This approach has been frequently refined over the past several decades to arrive at a relatively ubiquitous and standardized approach [12]. However, models that reduce the spatial and/or temporal dimensions involved in a problem have many limitations as well as benefits.

At the time of the original DPF model development, mathematical solutions to problems in fluid mechanics were limited to four basic approaches: 1) analytical solutions to the N-S equations, available for fewer than 40 simple cases [13]; solutions based on similarity principles capable of approximating a larger set of cases, but still limited to basic flows [13]; the nascent field of Computational Fluid Dynamics (CFD) [14], not yet capable of efficient broad application to arbitrary cases; and 0D/1D models based on assumptions of what occurs in the microscopic pore structure, and populated with parameters discoverable and tunable by experiment. By approaching the problem as a reduced dimension model, efficient solutions can be achieved without destructive testing, which would ultimately interfere with the validity of the filtration mechanisms. Parameters required for the model allow for very specific results. Alternate simulation or modeling possibilities were either untenable or inferior. The fundamental assumption, the unit cell/collector model, has a strong basis and long history of evaluation, being introduced in the 1940's and 50's [15–17].

However, future development of PM capture modeling remains due to severe limitations, especially in light of recent mathematical constructs [18]. Principally, the

requirement to introduce a large number of empirically tunable parameters leaves the reduced dimension modeling approach largely an echo of the test data on a particular filter and run condition. Broad application of these calibrated parameters is not dependable as they are not based on fundamental physical laws, in contrast to most aspects of modern CFD [14]. Several of these parameters pertain to the geometric description of the substrate within the unit collector paradigm. Perhaps the most sophisticated is the heterogeneous multiscale filtration model which employs a PDF of the size distribution [19]. While LBM cannot handle a more accurate and detailed simulation over an entire filter device for computational cost reasons, a representative sample with greater fidelity and fundamental physics has the potential to capture more extensive characteristics.

Reporting only averaged macroscopic boundary condition results is perhaps the greatest disadvantage of the reduced dimension model. Even with well tuned and calibrated empirical parameters, it reports results such as net PM capture, pressure drop and assumed average porosity change. None of this helps evaluate the complex situation in the substrate detail itself. The required tests themselves do not create an investigatable image either. If evaluation of different filter material bases is of interest, a whole new calibration process needs to come from test. As such, the use of reduced dimension models as a research tool is severely limited, and lacks extensibility. Macroscopic variables are certainly of interest, but if deep physical understanding is sought for: 1) new discoveries across substrate types; 2) the best possible decisions on

substrate choice; 3) statements on the relative importance and order of magnitude of any effect; and 4) modifications with high confidence, a true detailed physical basis is required. This is largely analogous to the use of empirical correlations and simple analytic expressions versus CFD in the exploration of complex machinery.

1.3 Research Objectives and Structure

1.3.1 Objectives

For an LBM model to successfully simulate incompressible turbulence and turbulent transition, as well as an investigatable picture of mass transfer processes in a representative slice of the substrate, the following objectives are established:

1. An unambiguous LBM scheme that definitively captures the incompressible behavior of low Ma flows in the hydrodynamic limit. This includes derivation of a corresponding optimal multiple relaxation time (MRT) collision operator form.

2. A canonical flow code to simulate transition and turbulent regimes with the results of research objective 1.

3. A PM transport model which accounts for interception and Brownian diffusion,

less reliant on tuned or lumped parameters.

4. A conjugate heat transfer model for the temperature field in the fluid and solid domains.

5. An algorithm that can flag lattice cells as solid or fluid and produce an appropriate substrate representation, verified by empirical formulas.

6. Parallelize all work for general purpose graphics processing units (GPGPU) and computer processing units (CPU); compare and contrast.

7. A multiphysics code for filter modeling combining objectives 1, 3, 4, 5, and 6.

1.3.2 Document Structure

Chapter 2 reviews the current state of research literature relevant to the stated objectives, and continues to build motivation for the objectives. Chapter 3 describes the base methodology that this work builds upon, providing background on the LBM, turbulence simulation, and computational methods.

Subsequent chapters focus on one or more of the research objectives, expanding the state of literature and methodology as necessary. Primarily, these chapters present the derivation and numerical results which are the objectives of this work.

A concluding chapter summarizes the completed objectives and results as well as

suggesting future work. Appendices providing further detail on derivations follow.

Chapter 2

Literature Review

The published work on principles that comprise a mesoscale approach will be the focus of the review. Collectively referred to as transport phenomena; the fluid, solid particulate, and heat transportation relevant to the research objectives of this work comprise the fundamentals for review.

2.1 Incompressible Lattice Boltzmann Method

While the LBE is frequently applied to incompressible flows, the standard form actually recovers the compressible N-S equations in the low Mach number limit [20]. He *et al.* suggest that the standard LBE can be viewed as an artificial compressibility

method, with the resultant numerical error [20]. To eliminate this error, several attempts at an incompressible single-relaxation time (SRT) lattice Boltzmann equation exist in literature [21–25]. By limiting the density variation contribution, schemes [21–24] do not fully recover the desired incompressible conservation equations:

$$\nabla \cdot \boldsymbol{u} = 0, \tag{2.1}$$

$$\frac{\partial \boldsymbol{u}}{\partial t} + \nabla \cdot (\boldsymbol{u}\boldsymbol{u}) = -\frac{1}{\rho_0}\nabla P + \nu \nabla^2 \boldsymbol{u}. \tag{2.2}$$

Additionally, with the exception of [24, 25], the proposed schemes cannot suitably handle transient flows.

Guo *et al.* provide the exception, and produced an incompressible scheme without artificial compressibility error which is also valid for transience [25]. Due to a general definition of the equilibrium distribution function (EDF), the scheme requires the introduction of three free parameters, governed by two equations, said to satisfy incompressible flow physics. Thus, there exists an infinite number of choices for the EDFs, a fact Banda *et al.* also noticed [26]. While the paper does choose 5/12, 1/3 and 1/12 as the coefficients in the numerical results section, there is no indication as to why, or if these are the best choice. This fact is also noted by Banda *et al.* [26]

leading to a question we ask here: what of the other possible parameter choices?

Shi *et al.* display a single set of parameters for the Guo model [27]. However, there is no clear reason for the choice, exploration of alternative choices, nor clear derivation. Additionally, a speed of sound is still present in their model, a physical impossibility for a truly incompressible flow.

Questions still remain about the uniqueness of an incompressible form, derivation techniques, and the merits of alternative coefficients and parameters in the Bhatnagar-Gross-Krook (BGK) form of the LBE. Additionally, the MRT form is presented by Du *et al.* [28], but because of the issues in the Guo derivation, it is not definitive. A 3D form also requires definitive definition.

2.2 Turbulence Simulation

Numerous studies explore LBE-DNS, from the earliest years of LBM to present, [29–32], among others. Of those studies, [29, 31] simulate the canonical decaying homogeneous isotropic turbulences (DHIT) in 2D and 3D, but of particular interest is the study by Lammers et al., which directly simulates moderate-Re flow in a 3D, but periodic, flat plate channel [30]. Unlike many other studies, the lattice resolution is the Kolmogorov scale, resulting in fully resolved DNS without the need for entropic

stabilization. Turbulence statistics are in good agreement with pseudo-spectral methods, however, the authors point out some pressure coefficient discrepancies. They go further in stating that this is a result of the slight compressibility error of the standard LBE. Martinez et al. make a similar observation in their work [29].

Specific to transition, LBE-LES has been used to overcome the inherent difficulty with a Reynolds Averaged Navier-Stokes (RANS) approach [33]. While certainly superior to RANS, and tractable in 3D and complex flows, certain scales remain uncaptured, and their influence only assumed through a Smagorinsky model. Additionally, the onset and evolution of transition does not occur, simply a study at an Re exhibiting the properties. These same descriptions apply to [34], another representative source on transitional flow regime studies through LBM. Most recently, LBE-DNS is applied to aneurysms where transition is suspected, and found [35]. At great cost, transition Re is approximately determined by a simple search. Due to the complex nature of the geometry the bounceback scheme is used with several levels of resolution to find grid independence. A standard SRT-LBE is used for the flow, with all of the associated errors previously expounded in this work. A particular consequence of a non-incompressible SRT model, aside from errors, is the lower stability and longer convergence rate when compared to even the SRT incompressible model [28].

2.3 Particulate Matter Transport

Four major approaches exist when considering solid particle transport simulation in the lattice framework. The most physically accurate considers the particle as a finite size and arbitrary shape [36]. This approach is costly and complex when simulating flows with a large number of particles and particles substantially smaller than the characteristic dimension. In such flows a point particle approach is more tractable and accurate. A grid that realistically covers the domain would not provide sufficient links to describe the shape well. The method is not free of errors, as the particle is merely a shell filled with a fictitious fluid. A method-of-moments LBE approach is presented by Gschaider et al. [37] to consider size distribution. This aspect can be important for flows with particles of substantially disparate scales, but is unnecessarily complex, costly, and prone to uncertainty in determining model constants when not essential. The authors report the seven additional scalars (moments) of this model increase memory consumption and significantly increase computational time. Thus, the point particle and particle concentration approaches, Lagrange/LGA and LBM, respectively, will be the focus here. In all cases, the phases are decoupled, the particles are spherical in shape, and particle-particle interaction away from the walls is assumed to be insignificant [38].

2.3.1 LBE-Lagrange

Lagrangian or particle Monte Carlo motion descriptions are a direct way to consider particle transport while the LBE dictates the flow. The same basic Langevin equation and components of motion used for arbitrary shape particle transport are solved [38]. Rotation is neglected. Lantermann, Hanel, and Filippova include a large number of forces and capture mechanisms in their work including: electrical charge, buoyancy, van der Waals, and Brownian motion [38, 39]. As particles are deposited, evolution of the solid domain is also accounted for.

Particles will effectively never rest on a lattice node since motion is not tied to discrete positions, adding complexity. The computational cost to simulate a very large number of particles individually is prohibitive because each has its own continuous pathline, and these studies inspect relatively small regions, compared to the obstacle scales. Over time periods of interest it is important to evaluate the aggregate statistical behavior, not arbitrary positions of single, or small numbers of particles.

2.3.2 LBE-LGA

The LGA method, original introduced for fluid flows [40], is a statistical approach to motion which has been applied to particle motion [41, 42]. The applications of

these studies, snow formations and under-pipe scour, respectively, have several gross transport mechanisms in common with filtration. Dupuis and Chopard find that many particle details are effectively irrelevant in flows of interest [42], verifying the capability of LBE-LGA. The continuous nature of the Lagrangian description is no longer a problem; particles always reside on a lattice node after each time step and large numbers of particles are considered. The lattice for the fluid flow dictated by the LBE is the same lattice for the LGA simulated particles.

Brownian motion is implicitly considered. Some random motion does occur from mapping particles to discrete nodes. Similar to PM deposition on a filter, the snow model allows alterations to the surface geometry. The surface builds up as the particle distribution comes to occupy a lattice node linked to a solid node. More than one of these interceptions must occur, so repeated motion to this node eventually provides enough material to relegate the node to a solid flag and provide a new flow obstacle. Qualitatively, these studies are successful.

Computation requires numerous steps achieving partial calculation of the new position and random number generation, an expensive prospect for the CPU. The particle time step must be chosen carefully to keep the particle motion to less than one lattice unit at a given flow time step. This makes it difficult to find a satisfactory value for flows with disparate velocities throughout.

2.3.3 LBE-Euler for Particle Concentration

Yamamoto *et al.* applied an additional LBE for particle transport, similar to the double-distribution function (DDF) approach for heat transfer [43, 44]. The small PM in large quantities is treated as a concentration of a separate species and a velocity field shared with the flow. For sufficiently fine particles this Eulerian approach has been utilized substantially in the past in flows that bear resemblance to the PM transport study here [45–47]. With certain probability, the concentration at a node along the wall will "stick", allowing a gradual buildup. When the concentration reaches 1, the node becomes part of the wall. This is similar to the LGA approach.

The lattice for the species (particle) concentration is the same as the flow, the species/-particle presence is assumed to not affect the flow away from the wall, and in place of ρ in the LBE, Y represents the concentration. It is recovered from the zeroth-order moment Y, and the flux can be recovered from the first-order moment of the variable. The collision relaxation time is the same as the flow LBE, but no explanation or reasoning is supplied. As in the flow and thermal LBE, the value of the collision operator should be tied directly the diffusivity of the conserved property. Thus, Brownian diffusion, or Fick's law, is not explicitly included in their work.

2.4 Dominant Mechanisms

Multiple PM capture mechanisms exist, but not all are relevant to DPFs specifically. Additionally, inclusion of irrelevant or minor aspects can degrade solution accuracy, rather than enhance it. For completeness, the potential mechanisms from the literature include: inertial impaction, interception, thermophoresis, electrical potential, Brownian motion (diffusion), straining, gravitational and buoyancy forces, and van der Waals force [10, 11, 38, 48].

Some of these mechanisms are not relevant to passive filtration or DPF specifically. Of those that are, Konstandopoulos and Johnson found that Brownian diffusion and interception dominate [11]. This work will follow their finding and focus on these mechanisms specifically.

2.5 Heat Transfer

Within the LBM framework, conductive heat transfer is solved with a simplified LBE, and convective heat transfer is usually considered with either a multi-speed LBE (MS-LBE) or a double distribution function LBE (DDF-LBE). Chapter 5 of [49] provides an overview of the MS-LBE approach, which is summarized here for completeness and

as an introduction to the more relevant DDF-LBE. Consideration is also required for conduction heat transfer, and joining the models for these heat transfer mechanisms into an appropriate conjugate heat transfer (CHT) capability.

Briefly, Guo and Shu [49] point out the following difficulties with the MS-LBE: initially fixed Pr, potential for incorrect ν in the energy equation, poor numerical stability, limited temperature simulation range, and large computational cost. There are benefits to using such a model, however, they are not universally valuable. MS-LBE can handle coupled flow and the full energy equation, allowing consideration of additional work and dissipation terms, but for Boussinesq flows this is not a useful advantage.

2.5.1 DDF-LBE

Bartoloni *et al.* utilized the fact that the flow and temperature fields can often be decoupled, so each can be solved through a separate LBE [50]. Considering the temperature as a separate transport species, Shan gave the temperature field an equivalent full additional D2Q9 EDF [51]. The model has the advantage of using the temperature driven density difference to directly influence flow velocity. However, the use of a full EDF for temperature is more costly than using an EDF tailored to the simpler temperature transport equation.

To address the compressibility error with Boussinesq flow, as well as reduce the simulation cost by using only the required EDF, Guo et al. adopted their SRT incompressible model [52]. The temperature EDF does drop two of the four terms and becomes linear without loss of correctness, reducing the computational cost. Additionally, it is shown only 2D (where D is the number of dimensions) lattice velocities are required for the temperature transport distribution, further substantially reducing computational cost. Per section 2.1, the incompressible model is not fully correct. While the formulation does not allow direct influence of temperature on flow velocity, a forcing term can account for the motion change due to the bulk modulus (β).

Jami *et al.* recently extended this basic approach to utilize MRT in both the flow and temperature models [53]. A five velocity approach to the thermal field was selected instead of the four velocity approach found to be sufficient by Guo [52]. Importantly, the MRT approach allows for transitional flows, and results report the ability of MRT-LBM to satisfactorily handle convective flows.

2.5.2 Conjugate Heat Transfer

Wang et al. implemented a LBM CHT model for microchannel flow with good results [54]. This particular work is interesting not only for the relevance of the application

to pore scale filters, but also because they successfully utilized a halfway bounce-back type scheme at the fluid-solid interface with both the flow and thermal lattices. Tarokh et al. specifically used the same approach to the energy equation in the fluid and solid domains [55]. As a result, continuity of flux terms is automatically handled, unlike the special treatment required for N-S CFD. The study includes more complex geometries, further generalizing the CHT LBM approach.

These studies utilize the standard SRT-LBE, not necessarily the most appropriate for many applications. MRT in particular becomes important for small passage flows [56]. Additionally, they utilize the Shan approach which introduces an unnecessary number of lattice velocities and EDF terms.

2.6 Porous and Disordered Media

Many disordered media applications have three different fundamental scales, especially true in filters. The largest scale, the device as a whole, can be treated as a black box in a system, but little understanding is gained. Because this work seeks to provide investigative images and a physical basis, the other two scales, representative elementary volume (REV) and pore, are the focus of review. Both approaches often take advantage of the halfway bounceback BC of LBM to handle the complex boundaries inherent in disordered media. Important to the ability of this boundary

to properly predict the location and size of solids in the domain is the use of MRT [56]. In that work, SRT is shown to produce a viscosity dependent error in channel width. MRT also has the additional benefit of superior numerical stability [31].

2.6.1 REV Scale

Representing only the general behavior of the filter medium, the REV scale at minimum includes the effects of average porosity [57]. In this work by Chen, the Brinkman-Darcy, Forchheimer-Darcy, and Klinkenberg effects and equations are considered. That last effect being critical for large Kn where apparent permeability does not sufficiently describe flow rate. Despite REV scale simulations generally being used to avoid geometric details, the authors present a simulation which specifies heterogeneous randomly scattered porosity in 2D to a high resolution; substantially more detailed than assuming homogeneous features. In the nanoscale permeable areas of the domain the Klinkenberg effect becomes an important effective body force, allowing some flow to pass instead of assuming flow only occurs in the unoccupied space.

Chen's study is based on fundamentals from Guo and Zhao [52]. The form of the body force they derive for porous media flows completely eliminates residual errors. They considered the Ergun correlation to describe the physics. Their study did not map any detailed flow features like that of Chen, but was verified with canonical flows.

Examples of other attempts to produce REV scale filter models are based on the LBE Spaid and Phelan introduced [58], however, the forcing terms of this approach leave undesirable errors in recovering the general N-S equations [59].

2.6.2 Pore Scale

Simulation at the pore scale strictly resolves the LBE only, as opposed to the LBE with porosity and permeability laws in a body force term to model what cannot be directly resolved. This level will either require a large node count, modest pore sizes, and/or some under-resolution. Manz et al. [60] provides such a study, where the resolved pore sizes need not be as small as PM cake, for example. Resolution for the packed spheres in this single phase study is sufficient at $\sim$86 μm.

Succi et al. presented the first work on 3D LBM for pore scale disordered geometries [61] almost immediately after LBM inception. The bounceback nature of the randomized BCs was recognized as valuable in this application of LBM. The study is particularly significant because it confirms LBM's adherence to Darcy's law.

A recent study looks at packed beds of spheres in a pore scale approach [62]. The authors focus on proper BCs and collision forms related to the work of Pan et al. [56]. They confirm SRT-LBE is inappropriate. All blockages are spherical, and they use a pre-made program, waLBerla. An interesting result of having such a regular

blockage shape, and pores which can be completely resolved, is that a curved BC treatment on the solids can be implemented. This is generally not appropriate in truly disordered and particle capture media due to superior resolution requirements, evolution of the surface shape, and irregularity/randomness. However, the study shows excellent results from pore scale LBM.

2.7 Aftertreatment Synthesis

The field of LBM aftertreatment filtration is relatively new, and is the synthesis of many of the aforementioned topics in this review. One of the first papers outlining the benefits of LBM for this purpose comes, in part, from communications between PNNL and MTU [63]. This work describes some of the simulation and modeling approaches, and addresses common production filters. The study uses a standard SRT-LBE. To model the geometry of a filter in use, assumptions are made about already deposited PM and PM distribution. No temperature treatment exists, and resolution is limited to 100 μm.

Since then, the majority of the work has been conducted by Yamamoto with researchers at Nagoya University and Nissan Motor Co. Their standard approaches are captured in [43]. Since this early work on cordierite filters, they have published several updates exploring additional filter types with LBM, such as carbide fiber [44].

While interesting results, there is no new fundamental methodology, and few details are revisited or revised.

To form a computational domain they use a CT scan. In the case of [44], this results in 1.44E8 nodes to represent a domain 4.1 mm $\times$ 8.6 mm $\times$ 9.4 mm (331.4 mm^2), a sufficient count to accurately capture REV scale. The resultant resolution is 13.3 μm, the same resolution of the scan.

Incompressibility is claimed, however, the EDF does not obey incompressible mass conservation (equation 2.1). There is a small difference from their earlier work on cordierite filters, [43], where a SRT-LBE with body force is used to account for deposited soot permeability. Similar to Chen's REV scale models, it is somewhat of a hybrid. The main substrate pores are directly simulated through detailed grid resolution, but nanoscale pores are accounted for with Darcy's law alone. The quoted permeability, κ = 2.0E-14 m^2, is on a scale subject to the here neglected Klinkenberg effect in addition to Darcy's law [57]. Neglecting the Forchheimer effect is likely appropriate due to the velocities involved.

Temperature and species concentration are also governed by the LBE, with the EDF modified to replace ρ with the respective macroscopic values T and Y_α. Each macroscopic value is recovered from the zeroth order velocity moment of the distribution functions. The approach is that of Shan [51] as opposed to Guo [52].

Even though not an aftertreatment specific application, Kang *et al.* performed a series of filtration-like studies based on a survey of LBM methods [64]. Unlike the works of Yamamoto, a fully incompressible LBE is utilized, that proposed by Guo *et al.* [25]. As reviewed in preceding sections and chapter 4, ambiguity remains. The authors do not mention which set of parameters they utilize. LGA is avoided for the transport of particles in favor of a LBE species transport equation. No rules are placed on deposition growth, which can result in growth which is unphysical when sufficient flow momentum would otherwise break the structures. This can be seen in figure 7 of their study. Not all runs exhibit this behavior because mineral reactions can make up for the lack of rules when the Damköhler number is sufficiently low. Unlike aftertreatment filtration, the application is essentially study of a fracture, dominated by a small number of flow paths and low porosity; a relatively easier geometry.

Results in all aftertreatment studies demonstrate the superiority of LBM for porous media with PM capture, compared to other continuum or reduced dimension approaches.

2.8 Summary

A new, comprehensive, LBM code has great potential in providing accurate and realizable aftertreatment models and turbulence insight based on the literature reviewed.

When the work of previous authors is combined with fundamentally new methodology and new study approaches, incremental improvements will be produced.

Chapter 3

Methodology

In this chapter, focus is on the benefits and background of the methodologies later researched and employed for the dissertation objectives. Modifications are explored in subsequent relevant chapters. The basis presented here will be referenced and built upon.

3.1 The Lattice Boltzmann Method

Macroscopic N-S based CFD functions well for many flows, and has long been the standard. However, certain flows are either unsuitable for the continuum assumption, or can utilize unique benefits of a mesoscopic approach and the results of the LBE.

Flows both suitable and unsuitable to continuum analysis benefit from the more fundamental physical basis of the LBM, namely, the motion of a large number of molecules on a smaller scale than macroscopic variables.

Benefits to the LBM both related to this dissertation and additional flows are summarized in the following list:

- Simple boundary condition implementation yielding second-order accuracy. Namely, the heuristic half-way bounce-back scheme and related revisions.
- Generally superior computational performance due to local computation and linearity in the Boltzmann equation with BGK and MRT collision operators.
- Conjugate heat transfer without special interfacial treatment.
- Straightforward addition of multiphase and multispecies systems.
- Microscale flows are possible due to the mesoscopic basis.
- Generally minimal pre-processing and meshing time.

3.1.1 Origins

Through the work of many thermodynamics pioneers the models of kinetic theory have been defined and applied. Bernoulli developed the concept of a kinetic theory in

1738. Helmholtz recognized the transformation and conservation of all types of energy in 1847. Clausius showed that molecules move with velocities different than the bulk fluid and that they travel a mean free path. In 1860 Maxwell introduced probability to kinetic theory. Shortly after, Maxwell developed the idea of intermolecular collision forces. Boltzmann introduced what would become the central theme of the LBM in 1872. Proof that statistical mechanics leads to macroscopic properties of interest was displayed in 1917 by Enskog and Chapman. [65]

The Boltzmann equation can be expressed as

$$\frac{\partial f}{\partial t} + \boldsymbol{\xi} \cdot \nabla f = \Omega(f), \tag{3.1}$$

where f is the velocity distribution function of particles and is a function of position $\boldsymbol{x}$, particle velocity $\boldsymbol{\xi}$, and time t [6]. The collision operator was approximated as a simple linear equation of intermolecular collisions to conserve the necessary macroscopic quantities:

$$\Omega(f) = -\frac{1}{\tau}\left[f - f^{eq}\right]. \tag{3.2}$$

This Bhatnagar, Gross, and Krook (BGK) model [66] is appropriate for a wide variety of applications. The term f^{eq} is the Maxwell-Boltzmann equilibrium distribution function, and τ is the rate at which equilibrium is reached in collisions. The PDF of particle velocities, with Helium-4 at different temperatures as the example fluid, is visualized in figure 3.1. The relatively large velocities are those of individual molecules, not of the bulk fluid, which is generally significantly smaller.

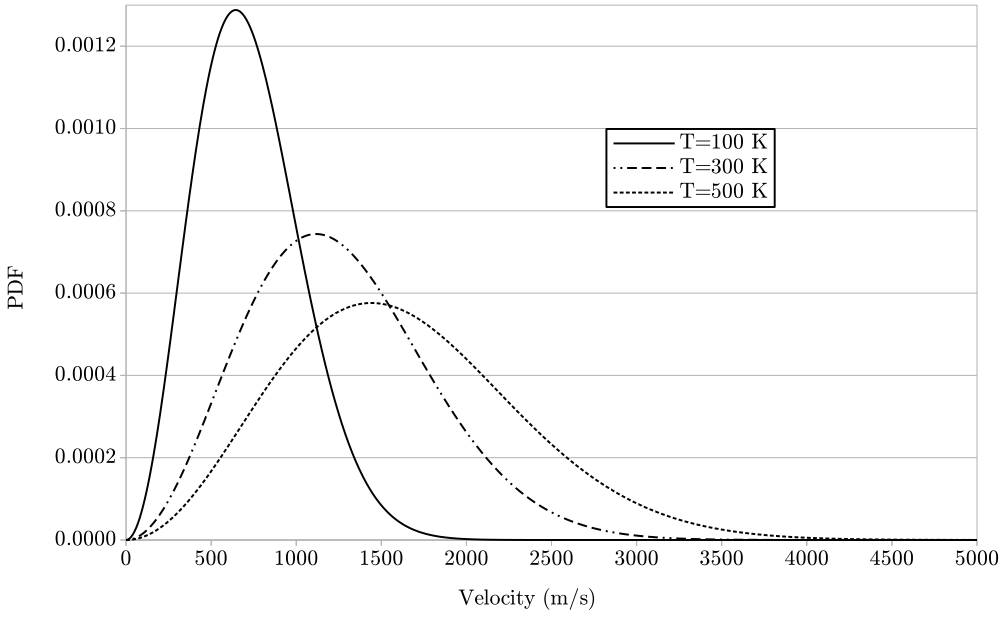

Figure 3.1: PDF of He-4 particle velocities at different temperatures.

3.1.2 The Lattice Boltzmann Equation

To discretize equation 3.1, f^{eq} is expanded into a Taylor series in terms of fluid velocity $\boldsymbol{u}$, and truncated for low Ma flows as

$$f^{eq} = \frac{\rho}{(2\pi RT)^{D/2}} e^{\left(-\frac{\boldsymbol{\xi}^2}{2RT}\right)} \left[1 + \frac{\boldsymbol{\xi}\cdot\boldsymbol{u}}{RT} + \frac{(\boldsymbol{\xi}\cdot\boldsymbol{u})^2}{2RT} - \frac{\boldsymbol{u}\cdot\boldsymbol{u}}{2RT}\right], \tag{3.3}$$

where D is the number of spatial dimensions. With the restriction that the N-S equations must be recovered in the hydrodynamic limit, the quadrature for discretization yields

$$f_i = w_i f(\boldsymbol{x}, \boldsymbol{c}_i, t) \quad \text{and} \quad f_i^{eq} = w_i f^{eq}(\boldsymbol{x}, \boldsymbol{c}_i, t), \tag{3.4}$$

where w_i are the weights related to each discrete velocity vector $\boldsymbol{c}_i$ of the continuous velocity $\boldsymbol{\xi}$. Important macroscopic variables arise, now from the summation instead of the integral of f. The conservation of mass and momentum are expressed as

$$\rho = \sum_i f_i \quad \text{and} \quad \boldsymbol{u} = \frac{1}{\rho}\sum_i \boldsymbol{c}_i f_i. \tag{3.5}$$

Returning discretizations 3.4 to equation 3.1 with associated variables, and integrating over the interval t to $t+\delta_t$, the LBE arises. Combining with the BGK collision operator yields

$$f_i(\boldsymbol{x} + \boldsymbol{c}_i\delta_t, t + \delta_t) - f_i(\boldsymbol{x}, t) = -\frac{1}{\tau}\left[f_i(\boldsymbol{x}, t) - f_i^{eq}(\boldsymbol{x}, t)\right]. \tag{3.6}$$

The EDF of equation 3.3 now has the discrete form

$$f_i^{eq} = w_i \rho \left[1 + \frac{\boldsymbol{c}_i \cdot \boldsymbol{u}}{c_s^2} + \frac{(\boldsymbol{c}_i \cdot \boldsymbol{u})^2}{2c_s^4} - \frac{\boldsymbol{u} \cdot \boldsymbol{u}}{2c_s^2} \right] \tag{3.7}$$

where c_s is the speed of sound. Three additional macroscopic variables of interest are available; pressure, momentum flux tensor, and viscosity,

$$P = \rho c_s^2, \quad P\boldsymbol{I} + \rho \boldsymbol{u}\boldsymbol{u} = \sum_i \boldsymbol{c}_i \boldsymbol{c}_i f_i, \quad \text{and} \quad \nu = c_s^2 \left(\tau - \frac{1}{2} \right) \delta_t. \tag{3.8}$$

Viscosity is directly tied to the collision relaxation time τ. This is a physically sensible model Chapman presented in his work on the theory of diffusion parameters in 1917 [67]. In fact, in that same work the macroscopic mathematical models, the N-S equations, are recovered in the hydrodynamic limit by the Chapman-Enskog expansion

$$\frac{\partial \rho}{\partial t} + \nabla \cdot (\rho \boldsymbol{u}) = 0, \tag{3.9}$$

$$\frac{\partial (\rho \boldsymbol{u})}{\partial t} + \nabla \cdot (\rho \boldsymbol{u}\boldsymbol{u}) = -\nabla P + \nabla \cdot \left[\rho \nu \left(\nabla \boldsymbol{u} + \nabla \boldsymbol{u}^T \right) \right]. \tag{3.10}$$

The expansion is not presented here, however for the iLBE derived as a research objective of this work, the same procedure is presented in appendix A.

3.1.3 Lattices

The index i is determined by the velocity value q in the standard model label DdQq, where d is the number of spatial dimensions. This network of i indices connects a node to all of its local neighbors by the discrete velocity vectors. The resultant lattice transports probability mass functions (PMF) 3.4 in accordance with the LBE. The number of velocities q in a lattice must meet symmetry and invariance requirements. Several of the most popular sufficient lattices are displayed in figure 3.2. The lattices in the left column are actually suitable only for advection-diffusion of scalars (which utilizes the same LBE derived above), and those in the right column are suitable for fluid flow.

Weights for each lattice, as well as velocity vector components and speed of sound, are required for equation 3.7. For the lattices of figure 3.2, table 3.1 provides the details.

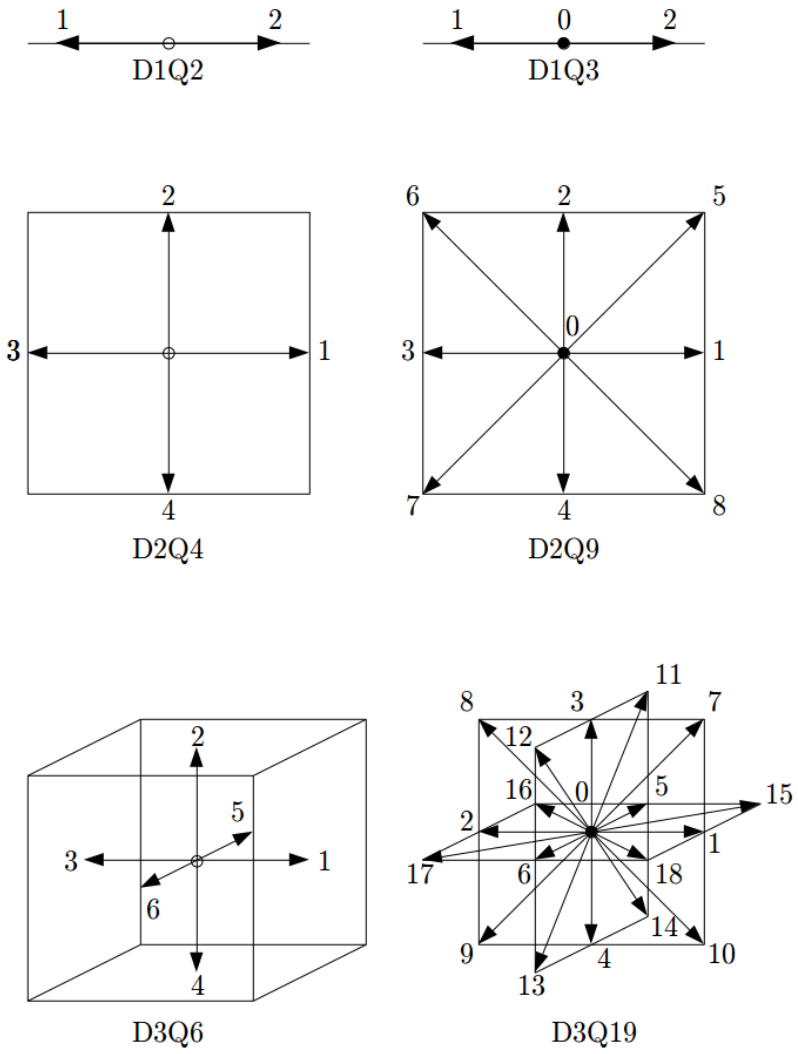

Figure 3.2: Some valid lattices of the LBM.

3.1.4 Boundary Conditions

Simple boundary conditions (BC) implementation is a unique benefit of the LBM. Three categories exist; heuristic, hydrodynamic, and extrapolation schemes. The hydrodynamic schemes are the most precise, but also; the most complex to implement,

Table 3.1
Lattice parameters.

Lattice	$\boldsymbol{c}_i$	w_i	c_s
D1Q2	$\pm$ 1	1/2	1
D1Q3	0	2/3,	$1/\sqrt{3}$
	$\pm$ 1	1/6	
D2Q4	($\pm$ 1, 0), (0, $\pm$ 1)	1/4	$1/\sqrt{2}$
D2Q9	(0, 0)	4/9,	$1/\sqrt{3}$
	($\pm$ 1, 0), (0, $\pm$ 1)	1/9,	
	($\pm$ 1, $\pm$ 1)	1/36	
D3Q6	($\pm$ 1, 0, 0), (0, $\pm$ 1, 0), (0, 0, $\pm$ 1)	1/6	$1/\sqrt{3}$
D3Q19	(0, 0)	1/3	$1/\sqrt{3}$
	($\pm$ 1, 0, 0), (0, $\pm$ 1, 0), (0, 0, $\pm$ 1)	1/18	
	($\pm$ 1, $\pm$ 1, 0), ($\pm$ 1, 0, $\pm$ 1), (0, $\pm$ 1, $\pm$ 1)	1/36	

inappropriate for disordered geometry, of no greater convergence accuracy than the heuristic and extrapolations schemes [68], in corners can present more unknowns than available equations, and when using a truly incompressible LBE, as later chapters will, pressure boundary conditions present a problem. As a result, the heuristic and extrapolation methodology will be the focus.

The heuristic schemes are based on the reflection of momentum when a particle impacts a solid surface. Implementation is simple, even for complex boundaries, free-slip/symmetry surfaces, and inlets. Second-order accuracy exists for the half-way bounce-back implementation [24]. However, when a discrete stair step approximates

curved BCs the order or accuracy drops to first-order. However, when utilizing high resolution grids, as in a porous media simulation, the convergence order of accuracy is of lesser importance since other factors dictate the need for a high spatial discretization (node counts). In actuality, the half-way and standard bounce-back schemes both follow the same algorithm,

$$f_{\bar{i}}(\boldsymbol{x}_f, t + \delta_t) = f'_i(\boldsymbol{x}_f, t), \tag{3.11}$$

where $\bar{i}$ is the reversed velocity vector of i for a no-slip wall, f' is the post-collision value, and $\boldsymbol{x}_f$ is the position of the last fluid node before a wall in the half-way bounce-back scheme (and is the wall node in the standard bounce-back scheme) (see figure 3.3). Effectively, the only real difference then between the schemes is where one imagines the wall, on the last node of the domain, or half of a lattice velocity beyond the last node of the domain. It is the nature of the time it takes the particle distribution to travel to the wall and back that places the wall half-way between with more accuracy. The node at the edge of the domain then has an integer value (standard bounceback) or a half-integer value (half-way bounceback). In the specular reflection form, the value $\bar{i}$ would be the velocity vector 90° from the incoming velocity vector.

A further heuristic scheme employed here is Ladd's revised half-way bounce-back

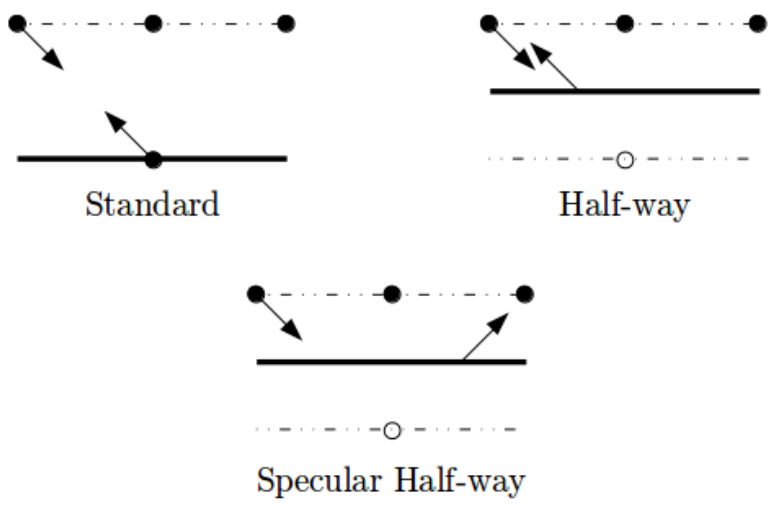

Figure 3.3: Bounce-back schematics over a single time step.

scheme [36]. By amending the momentum of both income and outgoing vectors, moving walls and velocity inlets (Dirichlet) can be applied as

$$f_{\bar{i}}(\boldsymbol{x}_f, t+\delta_t) = f_i'(\boldsymbol{x}_f, t) - 2w_i\rho(\boldsymbol{x}_f)\frac{\boldsymbol{c}_i \cdot \boldsymbol{u}_{in}}{c_s^2}. \tag{3.12}$$

Finite difference methods (FDM) often use a "ghost node" extrapolation approach where a node is placed outside the domain for computation purposes, but is not a part of the physical solution of the domain. Since the LBE is a type of finite differencing for the Boltzmann equation, Chen *et al.* applied the FDM to the LBM for gradient based BCs (Neumann), such as pressure [69]. In a general form the scheme is

$$f_i(\boldsymbol{x}_g, t) = \chi f_i(\boldsymbol{x}_0, t) - (\chi - 1) f_i(\boldsymbol{x}_1, t), \tag{3.13}$$

where g is the ghost node and 0 is the node on the boundary. The version Chen *et al.* published actually utilizes 2 instead of χ. However, this is not the only value which can be used for second-order accuracy, evident by simple rearrangement of various differencing forms. The scheme introduces non-local computation, however, it is stable and easy to implement.

3.1.5 Multiple Relaxation Time Collision Operator

Simplification of the inter-molecular collisions by the BGK model neglects the difference in relaxation times of the physical modes. d'Humières introduced the MRT model early in the development of the LBM [70] to offer a more accurate alternative. The MRT collision model increases computation time by an estimated 17% [71], but offers greater stability with increasing Re, and elimination of viscosity dependent geometry errors, especially in small passages [31, 56]. Both advantages are important to the work here; turbulent transition occurs at relatively high Re, and filtration includes a variety of passages, some only minimally spatially resolved. In place of the single relaxation time (SRT)-LBE of equation 3.6, the evolution equation with the MRT operator is

$$f_i(\boldsymbol{x} + \boldsymbol{c}_i\delta_t, t + \delta_t) - f_i(\boldsymbol{x}, t) = -\sum_j \Lambda_{ij} \left[f_j(\boldsymbol{x}, t) - f_j^{eq}(\boldsymbol{x}, t) \right] \tag{3.14}$$

where Λ_{ij} is a collision matrix of multiple relaxation times. A derivation of the incompressible MRT, with some reference to the standard MRT-LBE, based on the work of [72] is available in appendix A.

3.1.6 Heat Transfer

With relatively small adjustment, the LBE of section 3.1 solves the energy equation when temperature can be treated as a transported scalar:

$$\frac{\partial T}{\partial t} + \boldsymbol{u} \cdot \nabla T = \alpha \nabla^2 T + \dot{Q}. \tag{3.15}$$

A double distribution function is most appropriate for the flows considered here (see section 2.5). The flow velocity is resolved with equation 3.6 and distribution 3.7, and the temperature field with

$$g_i(\boldsymbol{x} + \boldsymbol{c}_i\delta_t, t + \delta_t) - g_i(\boldsymbol{x}, t) = -\frac{1}{\tau_T} \left[g_i(\boldsymbol{x}, t) - g_i^{eq}(\boldsymbol{x}, t) \right], \tag{3.16}$$

and

$$g_i^{eq} = w_i T \left[1 + \frac{\boldsymbol{c}_i \cdot \boldsymbol{u}}{c_s^2} + \frac{(\boldsymbol{c}_i \cdot \boldsymbol{u})^2}{2c_s^4} - \frac{\boldsymbol{u} \cdot \boldsymbol{u}}{2c_s^2} \right] \quad \text{or} \quad g_i^{eq} = w_i T \left[1 + \frac{\boldsymbol{c}_i \cdot \boldsymbol{u}}{c_s^2} \right], \qquad (3.17)$$

where g_i is now the temperature distribution function, τ_T is the thermal collision relaxation time based on $\tau_T = 3\alpha + \frac{1}{2}$ or $\tau_T = 2\alpha + \frac{1}{2}$, and g_i^{eq} is the temperature equilibrium distribution for the collision operator [51, 52]. $\boldsymbol{u}$ is supplied by the flow LBE and utilized in the thermal LBE at each time step. Conduction simulation is simply a special case where $\boldsymbol{u} = 0$.

The existence of two equations for g_i^{eq} comes from a refinement of the methodology in literature, dependent on the desired physics. Evaluation of both forms is conducted in this work to select the most appropriate method considering accuracy, and computational cost, with the second g_i^{eq} being more efficient due to fewer terms (2, 4, or 6 speed lattice for 1D, 2D, and 3D simulations, respectively). In the case of the longer g_i^{eq} form, the lattices on the right in figure 3.2 are required, as in the flow solution [51], but for the more compact g_i^{eq} the lattices on the left in the figure are appropriate [52]. For this more compact D2Q4 form, appendix B shows that equation 3.16 is recovered, thus obeying the macroscopic principle.

In either case, the macroscopic variables of interest are readily available:

$$T = \sum_i g_i, \quad Q = \sum_i \boldsymbol{c}_i g_i, \tag{3.18}$$

and, as with viscosity in the flow LBE, diffusivity $\alpha = c_s^2 \left(\tau_T - \frac{1}{2}\right) \delta_t$.

BCs for the thermal model are nearly identical to those for the flow LBE. Bounce-back can create a fixed temperature, and extrapolation allows for prescribed gradients, such as zero-gradient (adiabatic).

Conjugate heat transfer is a complex BC in traditional N-S CFD, however, in the LBM it is a relatively simple. By appropriately assigning the thermal diffusivity on nodes residing in the solid area, but solving on a continuous regular lattice common to both flow and solid domains, continuity is enforced at the boundary [54]. Actually, like the half-way bounceback scheme, the thermal boundary lies half-way between nodes.

An MRT collision operator can also be applied to equation 3.16 for improved stability. A form for the D2Q4 is derived in appendix B.

3.1.7 Particle Concentration Transport

As in the simplified energy equation (3.15), particle and species concentration can be treated as an advection-diffusion equation when certain effects such as reactions are absent, and simplifications such as one-way interaction and the particle diameter much less than characteristic length, are acceptable. The simplified form, Fick's second law [73], is stated here as

$$\frac{\partial Y}{\partial t} + \boldsymbol{u} \cdot \nabla Y = D\nabla^2 Y, \tag{3.19}$$

where $\boldsymbol{u}$ is the velocity field of the flow, Y is the volume concentration of the species, and D is the mass diffusivity. D is analagous to thermal diffusivity α and viscosity ν. Together, the three diffusion measures (all with units length^2/time) describe the diffusion of the three conserved properites, mass, momentum, and energy(thermal).

Just as the temperature transport equation can be modeled by the LBE, so can the species transport equation,

$$h_i(\boldsymbol{x} + \boldsymbol{c}_i\delta_t, t + \delta_t) - h_i(\boldsymbol{x}, t) = -\frac{1}{\tau_Y}\left[h_i(\boldsymbol{x}, t) - h_i^{eq}(\boldsymbol{x}, t)\right], \tag{3.20}$$

with equilibrium distribution function

$$h_i^{eq} = w_i Y \left[1 + \frac{\boldsymbol{c}_i \cdot \boldsymbol{u}}{c_s^2} + \frac{(\boldsymbol{c}_i \cdot \boldsymbol{u})^2}{2c_s^4} - \frac{\boldsymbol{u} \cdot \boldsymbol{u}}{2c_s^2} \right]. \tag{3.21}$$

The collision relaxation time is tied to the mass diffusivity/Brownian motion by $\tau_Y = 3D + \frac{1}{2}$. Individual particle motion is not tracked in this way, but for large numbers of small particles this is intractable and unnecessary. This collision relaxation time provides the statistically correct diffusive motion of large numbers of particles. Individually each particle would have a chaotic path based on temperature and Boltzmann's constant, but the ensemble average of motion will be zero, as well as the fluctuating term based on D.

Boundary condition treatment revolves around the half-way bounce-back scheme and modifications for inlet concentration (in place of velocity) as well as extrapolation outlet as a gradient. Sticking of the particle species to solid surfaces requires additional rules, and will be part of the novelty of this work in chapter 7. Modeling erosion is also possible with revised rules, but is not considered in this work.

3.2 Turbulence and Transition Simulation

3.2.1 Modeling and Simulation of Turbulence

Like the traditional N-S approach to CFD, turbulence can be modeled with approaches like the RANS equations. While efficient, only time averaged quantities are available, even in transience. More importantly, the computation of the values required for closure (Reynold's stresses) depend on several tuned parameters, five just for the $k-\epsilon$ model [74]. These parameters are based on experimental correlation and are more valid for certain flows and not others. Some work has been done to combine the best from multiple models, such as SST [74], but without resolution of turbulent structures, no model is broadly satisfactory. Turbulent transition models present the same pros and cons, focusing on time averaged intermittency in the onset of turbulence in the flow, and are overall broadly unsatisfactory [75].

Scale resolving simulation (SRS) addresses many of these issues, only resorting to modeling techniques for the lowest energy small turbulent scales. Kolmogorov determined these scales to be, in general, relatively unimportant to the greater effects of turbulence on flow [76]. The lack of resolution at certain scales still leaves some

uncertainty, and when computationally possible, resolution of every scale is the ultimate in accuracy. With the case of transition, this detail is desired as CFD progresses [8, 75].

3.2.2 Direct Numerical Simulation and Large Eddy Simulation

DNS refers to flow simulations without modeling of any type, or reliance on implicit diffusion of the numerical scheme [77]. No tunable parameters, experimental approximations, or overarching assumptions are required. Time and space are explicitly resolved, and detailed results available for inspection. The computational cost is high because now the space and time steps must be smaller than the smallest turbulent structure, estimated by Kolmogorov to be

$$N_i \approx Re^{3/4} \tag{3.22}$$

where N_i is the number of nodes in each direction. In transition, the role of the smallest scales in the process no longer presents uncertainty. The great cost of such detail can be reduced by the LBM. Inherent parallelism allows faster computation for a given domain size compared to the traditional N-S equations [49], isotropy

is superior [49], and the dissipative and dispersive effects are lower for improved small scale turbulent capture [31]. Turbulent continuum flows are possible with the mesoscopic LBE because of the collision operator, which recovers the macroscopic principles. There is an established history of the LBE for this purpose, as discussed in chapter 2.

Some past literature has attempted to reduce computation cost by intentionally under-resolving the simulation, and relying on higher order schemes, entropic correction, or other stabilizing tools like MRT [78]. All of which introduce additional assumptions and thus uncertainty about the results.

Due to the large computational cost of DNS, only a 2D simulation will be pursued with this full resolution. While turbulence is an anisotropic 3D phenomenon, analagous physical transitions and processes are present in lower dimensions. 2D simulation of transition and turbulent features is mathematically valid, and there is a long history as a tool for proof-of-method [78–81]. Even with these reductions, the *Superior* super-computing cluster is nearly overwhelmed with output data at times, and can require weeks of runtime.

LES will take over for 3D simulations due to the potential increase in node counts. The lattice is still well resolved; much more well resolved than a RANS approach, but an SGS model is deemed acceptable for the smallest scales. The energy cascade of Kolmogorov's theory dictates this approach captures the major actions of turbulent

flows. Since the SGS model of the original LES approach, Smagorinsky-Lilly, has a constant which is always included in the viscosity correction, it is not valid for laminar portions of the flow, and by extension, not appropriate for turbulent transition study.

In place, the Vremen SGS will be utilized [82]. In this model, the eddy viscosity can drop as low as zero in laminar and near wall areas, and increase in response to high shear in fully turbulent flows. As a result, transitional flows are possible with this approach, without the immense node counts of a DNS approach. A finite difference method (FDM) approach allows for the computation of the components required to determine the magnitude of the eddy viscosity, the local velocity gradients.

3.2.3 Evaluation Methodology

In the DNS case, for the the study of transience and transition the Hopf bifurcation is of primary interest. To find the initial bifurcation an extrapolation scheme of oscillation amplitude A(Re) in the vicinity of the critical Re will be employed. Thereafter, the velocity space and Fourier spectrum results will be used to approximate further Hopf bifurcations. While further frequencies will become superimposed with increasing Re, the velocity space will continue to show repetition until turbulence arises, after which the chaotic nature will form non-repetitive untraced behavior. The spectrum analysis will also show a large number of non-repeating frequencies.

Results in the fully turbulent regime will be computed and evaluated for fields of the following statistical quantities:

- Mean velocity, $\langle u_i \rangle$
- Turbulent kinetic energy, $k = \frac{1}{2}\langle u_i' u_i' \rangle$
- Energy dissipation rate, $\epsilon = 2\nu\langle s_{ij} s_{ij} \rangle$, $s_{ij} = S_{ij} - \langle S_{ij} \rangle$
- Local Kolmogorov scale, $\eta = \left(\frac{\nu^3}{\epsilon}\right)^{(1/4)}$
- Pressure coefficient, $C_p = \left(\frac{P - P_0}{\frac{1}{2}\rho_0 u_w^2}\right)$

LES results are evaluated with the same methodology. However, some finer details do not emerge since their large scale effects are only accounted for by the subgrid scale model.

3.3 Substrate Approximation

Realistic 2D substrate geometries are generated through modifications to the random number function in C. Certain nodes in the domain lattice are marked as "solid", and others as "fluid" in a boolean matrix. The benefit to this approach is that no CT scan or physical sample is required, and conversion from 3D to 2D without continuous pores is not an issue. The generation process is sensible when considering natural material

filters, like cordierite; a substrate is effectively a random arrangement of blockages within a certain size limit, which often overlap.

Within the confines of the domain filter area random seeds are placed, around which ellipses are built with random major and minor axes. Many of these structures will overlap to some degree as porosity decreases, creating a complex substrate. The number of seeds is the main determinant of porosity.

Lattice structure allows for simplistic substrate measurements. These measurements are first-order accurate, however, the high grid count required for a complex substrate limits the importance of higher-order schemes. Porosity is measured by dividing the number of fluid nodes in the filter by the number of nodes in the filter area (not counting inlet and outlet areas). Wetted perimeter is measured by counting the number of nodes on the boundaries of the substrate (the number of solid nodes bordering fluid nodes).

It is not enough to create a substrate with the above method which *looks* correct and consistent. Multiple techniques are utilized to judge appropriateness of the method, based on physical principles or numerical and experimental fits.

- Darcy's law
- Ergun equation

- Koponen model
- Gebart-Brinkmann model
- Gebart-Kubawara model
- Direct experimental data

3.4 Computational Language and Parallelization

C is the language for simulation in this work. There are many reasons to choose C/C++ including standardization, portability, control, libraries, etc..., however, one of the greatest reasons C is choosen is speed. Aruoba and Fernandez-Villaverde found C/C++ and Fortran to be to be at least an order of magnitude faster than many other possible languages, including Matlab, Python, Java, and Mathematica [86]. Commonality as a physics simulation language is a final critical consideration.

C also has the benefit of being parallelizable with the majority of the major paradigms, including OpenMP, MPI, OpenACC, CUDA, OpenHMPP, and OpenCL. To accomplish research objective 6, a GPGPU and CPU comparison must be considered. Portability, readability, comparability, available hardware, and effectiveness lead to the choice of OpenACC and OpenMP for comparison and final implementation.

The following observations are not entirely surprising when considering criticisms

of the much touted GPGPU approach [87], where the multiple order-of-magnitude increases over CPU's are largely an illusion generated by comparison to single-core CPU runs. Commercial codes such as STAR-CCM+ describe extensive testing in which GPU's offer no performance improvement for general CFD [88]. The load and access times present a substantial overhead.

A brief study was performed utilizing a quad-core AMD APU (A10-6800K) and 192 CUDA core GPU (GeForce GTS 450) for OpenMP and OpenACC respectively, the speed of each parallelism paradigm was compared. The 2D lid driven cavity and backward facing step were simulated with nodes varying from 2,500 to 262,000. Similar commands between the two paradigms allowed for direct comparison without variance related to coding style or available keywords and calls. The smaller simulations resulted in superior OpenACC performance, but by at most 15%. As node count increased, OpenMP gradually became the faster standard. It is theorized this is because of the need to pass data to traditional RAM (versus GPU memory) in larger amounts and over a greater number of iterations (time steps), and to display results to the screen.

The final decision between a CPU (OpenMP) and GPGPU (OpenACC) approach was largely determined by the best hardware available, the supercomputing cluster at MTU, *Superior*. It is difficult to determine if the APU and GPU comparison in the previous paragraph was an optimal way to compare speed, but *Superior* is currently

a CPU oriented cluster. GPGPU access is limited and the total CPU computing power is approximately 2.5x greater than the GPGPU computing power (32 versus 13 TFLOPS).

Using OpenMP on *Superior*, and studying the scaling of speed with increased core count shows the LBM algorithm and code benefit significantly from parallelism. In figure 3.4, the results of running the 2D lid driven cavity with 251,001 total nodes for 100,000 time steps are presented. 1, 2, 4, 8, 12, and 16 core solutions were run, five times each, and an average was computed. Speed is presented as million lattice site updates per second (Msu/s). The trend line shows linear scaling up to 8 cores, and a slow decline thereafter. 16 core runs still show value in run speed and efficiency.

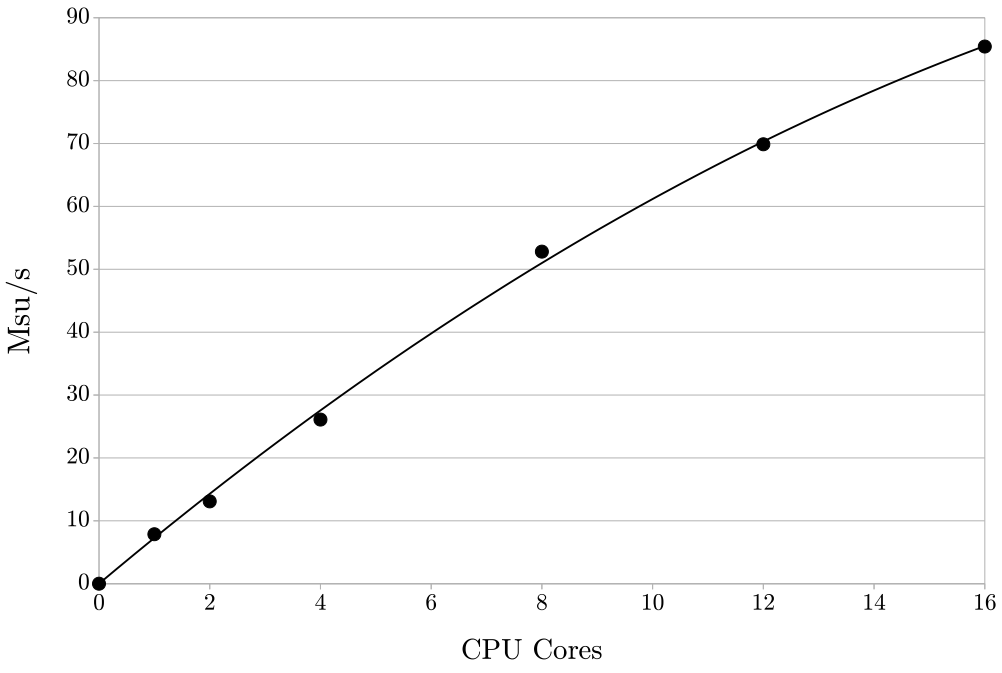

Figure 3.4: Speedup of LDC OpenMP code on *Superior*.

Chapter 4

The Incompressible LBE[1]

Abstract

A lattice Boltzmann equation for fully incompressible flows is derived through the utilization of appropriate ansatzes. The result is a singular equilibrium distribution function which clarifies the algorithm for general implementation, and ensures correct steady and unsteady behavior. Through the Chapman-Enskog expansion, the exact incompressible Navier-Stokes equations are recovered. With 2D and 3D canonical numerical simulations, the application, accuracy, and workable boundary conditions are shown. Several unique benefits over the standard equation and alternative forms

[1]The material contained in this chapter was previously published in the *International Journal of Computational Engineering Research* [1].

presented in literature are found, including faster convergence rate and greater stability.

4.1 Introduction

While the lattice Boltzmann equation (LBE) is frequently applied to incompressible flows, the standard form actually recovers the compressible Navier-Stokes (N-S) equations in the low Mach number limit. He et al. [20] suggest that the standard LBE can be viewed as an artificial compressibility method, with the resultant numerical error. To eliminate this error several steps toward a truly incompressible LBE exist in the literature [21–25]. Although limiting density variation most schemes [21–24] do not recover the exactly incompressible conservation equations:

$$\nabla \cdot \boldsymbol{u} = 0, \tag{4.1}$$

$$\frac{\partial \boldsymbol{u}}{\partial t} + \nabla \cdot (\boldsymbol{u}\boldsymbol{u}) = -\frac{1}{\rho_0}\nabla P + \nu \nabla^2 \boldsymbol{u}. \tag{4.2}$$

Additionally, with the exception of He and Luo [24] and Guo et al. [25], the proposed schemes are not designed for transient flows. The He and Luo [24] scheme recovers the

artificial compressibility N-S equations, which further requires that the characteristic time be large relative to the characteristic length. Guo et al. [25] design a fully capable unsteady incompressible scheme with three free parameters present in the definition of the D2Q9 equilibrium distribution function (EDF),

$$f_a^{eq} = \begin{cases} -4\sigma P/c^2 + S_a(\boldsymbol{u}), & a = 0 \\ \lambda P/c^2 + S_a(\boldsymbol{u}), & a = 1,2,3,4 \\ \gamma P/c^2 + S_a(\boldsymbol{u}), & a = 5,6,7,8 \end{cases} \tag{4.3}$$

where

$$S_a(\boldsymbol{u}) = w_a \left[3\frac{(\boldsymbol{e}_a \cdot \boldsymbol{u})}{c} + 4.5\frac{(\boldsymbol{e}_a \cdot \boldsymbol{u})^2}{c^2} - 1.5\frac{(\boldsymbol{u} \cdot \boldsymbol{u})}{c^2} \right], \tag{4.4}$$

These three parameters are governed by two equations,

$$\lambda + \gamma = \sigma, \qquad 2\lambda + 4\gamma = 1, \tag{4.5}$$

which create an infinite number of choices. Banda et al. [26] noted that while $\sigma = 5/12$, $\lambda = 1/3$, and $\gamma = 1/12$ are the parameters for the numerical tests in Guo et al.s

paper, questions exist about the properties of alternate possibilities. Shi et al. [27] utilize the same set of parameters to produce good results, however the choice is not explained or derived, nor is there an exploration of the alternative parameter choices from Guo et al.s paper.

Questions from past literature, our research group, and those who implement code still exist about the uniqueness of the incompressible form, derivation techniques, and the merits of the alternate values for the parameters σ, λ, and γ. In this work we seek to build off of the work by Guo et al. to:

- Describe a general derivation process;
- Clarify the literature and parameters for those impelementing the algorithm;
- Ensure consistent correct solutions;
- Evaluate the benefits to accuracy and stability with such a form.

This paper is organized as follows: Section 2 introduces the standard LBE and the derivation of a fully incompressible form through an appropriate ansatz. Section 3 presents numerical results which validate the form derived in section 2, compares results with other schemes, and explores the properties of alternate parameter values to equation 3. After the summary of section 4, appendix A.1 shows the recovery of the incompressible N-S equations through the Chapman-Enskog expansion.

4.2 Derivation of the D2Q9 Incompressible LBE

4.2.1 Standard LBE Form

From the standard LBE,

$$f_a\left(\boldsymbol{x}+\delta\boldsymbol{x}, t+\delta t\right) = f_a\left(\boldsymbol{x}, t\right) - \frac{1}{\tau}\left(f_a\left(\boldsymbol{x}, t\right) - f_a^{eq}\left(\boldsymbol{x}, t\right)\right) \tag{4.6}$$

the Chapman-Enskog multiscale expansion, as detailed by Qian et al. [89], results in the mass and momentum conservation equations:

$$\frac{\partial \rho}{\partial t} + \nabla \cdot \left(\rho \boldsymbol{u}\right) = 0, \tag{4.7}$$

$$\frac{\partial \left(\rho \boldsymbol{u}\right)}{\partial t} + \nabla \cdot \left(\rho \boldsymbol{u}\boldsymbol{u}\right) = -\nabla P + \nu\left(\nabla^2\left(\rho \boldsymbol{u}\right) + \nabla\left[\nabla \cdot \left(\rho \boldsymbol{u}\right)\right]\right). \tag{4.8}$$

In the D2Q9 LBE

$$\rho = \sum_a f_a, \quad \rho \boldsymbol{u} = \sum_a c \boldsymbol{e}_a f_a, \quad c_s = \frac{c}{\sqrt{3}}, \quad P = c_s^2 \rho, \quad \nu = c_s^2 \left(\tau - \frac{1}{2} \right) \delta t, \tag{4.9}$$

where $c = \delta_x / \delta_t$ is the lattice velocity, c_s is the speed of sound, $\boldsymbol{e}_a$ are the velocity vectors, and τ is the single collision relaxation time of the BGK model.

Many of the terms in equations 4.7 and 4.8 involve a variation of density with time or space, and thus suffer from compressibility error unlike the desired incompressible equations, 4.1 and 4.2. Relationships of equations set 4.9 depend on a speed of sound, and pressure and viscosity depend on that of sound.

4.2.2 An Incompressible LBE Derivation

An EDF must satisfy the necessary tensor symmetry and adhere to the incompressible conservation principles. For a valid EDF the form is first established, the governing principles are dictated, and an appropriate method is adopted to satisfy the form and principles. The result can be mathematically verified with the Chapman-Enskog expansion, shown in appendix A.1.

Based on the Maxwellian distribution and the nonlinearity of the momentum equation, an ansatz for the EDF form pertaining to the lattice discretization of figure 4.1

is established as:

$$f_a^{eq} = A_i + B_i \left(\boldsymbol{e}_a \cdot \boldsymbol{u}\right) + C_i \left(\boldsymbol{e}_a \cdot \boldsymbol{u}\right)^2 + D_i \left(\boldsymbol{u} \cdot \boldsymbol{u}\right), \tag{4.10}$$

$$i = \begin{cases} 0 & \text{for } a = 0 \\ 1 & \text{for } a = 1, 2, 3, 4 \\ 2 & \text{for } a = 5, 6, 7, 8 \end{cases} \tag{4.11}$$

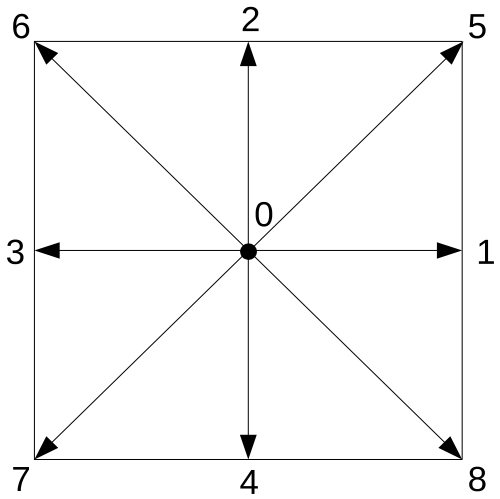

Figure 4.1: D2Q9 lattice velocities, a.

and as in [25] the mass and momentum governing principles are dictated as:

$$\sum_{a=0}^{8} f_a^{eq} = \sum_{a=0}^{8} f_a = Constant, \tag{4.12}$$

$$\sum_{a=0}^{8} c\boldsymbol{e}_a f_a^{eq} = \sum_{a=0}^{8} c\boldsymbol{e}_a f_a = \boldsymbol{u}, \tag{4.13}$$

and the zeroth-order incompressible momentum flux tensor is stated here as

$$\sum_{a=0}^{8} c\boldsymbol{e}_a c\boldsymbol{e}_a f_a^{eq} = \sum_{a=0}^{8} c\boldsymbol{e}_a c\boldsymbol{e}_a f_a = \frac{P}{\rho_0}\boldsymbol{I} + \boldsymbol{u}\boldsymbol{u}. \tag{4.14}$$

For generality and intuitive understanding we set $Constant = 1$ in the derivation. The additional assignment of $Constant = 0$, as in [25], is verified numerically to produce the identical result in section 3.

Remark 1 Equation 4.12 is critical in enforcing the zero-divergence law of equation 4.1. To validate that the statement made in equation 4.12 satisfies the requirement at each time step and point, both the summation of f_a and the finite difference method are independently evaluated in section 3.2. Both show the adherence to zero velocity divergence.

There are 12 unknowns in equation 4.10,

$$\begin{array}{ccc} A_0 & A_1 & A_2 \\ B_0 & B_1 & B_2 \\ C_0 & C_1 & C_2 \\ D_0 & D_1 & D_2 \end{array}$$

Several of these parameters can be determined through the conservation equations

and discrete lattice velocities. Due to the rest particle ($\boldsymbol{e}_0 = 0$),

$$B_0 = C_0 = 0, \tag{4.15}$$

and from the conservation principles 4.12 and 4.13,

$$\sum_{a=0}^{8} f_a^{eq} = A_0 + 4A_1 + 4A_2 + (2C_1 + 4C_2 + D_0 + 4D_1 + 4D_2)(\boldsymbol{u} \cdot \boldsymbol{u}) = 1, \tag{4.16}$$

$$\sum_{a=0}^{8} c\boldsymbol{e}_a f_a^{eq} = (2B_1 + 4B_2)c\boldsymbol{u} = \boldsymbol{u}. \tag{4.17}$$

Subsequently,

$$(A_0 + 4A_1 + 4A_2) = 1, \tag{4.18}$$

$$(2C_1 + 4C_2 + D_0 + 4D_1 + 4D_2) = 0, \tag{4.19}$$

$$(2B_1 + 4B_2) = \frac{1}{c}. \tag{4.20}$$

Through the 0^{th} order momentum flux tensor, and in the 2D case $\boldsymbol{u} = u\hat{i} + v\hat{j}$,

$$C_1 = \frac{1}{2c^2}, \quad C_2 = \frac{1}{8c^2}, \tag{4.21}$$

which further defines,

$$\begin{gathered} D_0 + 4D_1 + 4D_2 = -2C_1 - 4C_2 = -\frac{3}{2c^2}, \quad c^2(2A_1 + 4A_2) = \frac{p}{\rho_0}, \\ 2D_1 + 4D_2 = -4C_2 = -\frac{1}{2c^2}. \end{gathered} \tag{4.22}$$

There are now 8 remining unknowns, and only 5 linear equations. To provide an additional restriction an ansatz is introduced,

$$\frac{A_1}{A_2} = \frac{B_1}{B_2} = \frac{D_0}{D_1} = \frac{D_1}{D_2} = r. \tag{4.23}$$

Through a quadratic equation for r based on the relationships defined previously,

$$\begin{gathered} A_0 = 1 - \frac{2r+2}{c^2(r+2)}\frac{p}{\rho_0}, \; A_1 = \frac{r}{c^2(2r+4)}\frac{p}{\rho_0}, \; A_2 = \frac{1}{c^2(2r+4)}\frac{p}{\rho_0}, \\ B_1 = \frac{r}{c(2r+4)}, \; B_2 = \frac{1}{c(2r+4)}, \\ D_0 = -\frac{r}{c^2(r+2)}, \; D_1 = -\frac{1}{c^2(r+2)}, \; D_2 = -\frac{r-2}{c^2(8r+16)}. \end{gathered} \tag{4.24}$$

Consequently, $r = 4, -2$. 4 is the sensible result, and all of the unknowns can be resolved,

$$\begin{gathered} A_0 = 1 - \frac{5}{3c^2}\frac{p}{\rho_0},\ A_1 = \frac{1}{3c^2}\frac{p}{\rho_0},\ A_2 = \frac{1}{12c^2}\frac{p}{\rho_0}, \\ B_0 = 0,\ B_1 = \frac{1}{3c},\ B_2 = \frac{1}{12c}, \\ C_0 = 0,\ C_1 = \frac{1}{2c^2},\ C_2 = \frac{1}{8c^2}, \\ D_0 = -\frac{2}{3c^2},\ D_1 = -\frac{1}{6c^2},\ D_2 = -\frac{1}{24c^2} \end{gathered} \tag{4.25}$$

Building the EDF, the final incompressible form arises,

$$f_a^{eq} = \begin{cases} 1 - 5P/3c^2 + S_a(\boldsymbol{u}), & a = 0 \\ P/3c^2 + S_a(\boldsymbol{u}), & a = 1, 2, 3, 4 \\ P/12c^2 + S_a(\boldsymbol{u}), & a = 5, 6, 7, 8 \end{cases} \tag{4.26}$$

where

$$S_a(\boldsymbol{u}) = w_a \left[3\frac{(\boldsymbol{e}_a \cdot \boldsymbol{u})}{c} + \frac{9}{2}\frac{(\boldsymbol{e}_a \cdot \boldsymbol{u})^2}{c^2} - \frac{3}{2}\frac{(\boldsymbol{u} \cdot \boldsymbol{u})}{c^2} \right], \tag{4.27}$$

and the weights are those of the standard LBE,

$$w_a = \begin{cases} 4/9, & a = 0 \\ 1/9, & a = 1, 2, 3, 4 \\ 1/36, & a = 5, 6, 7, 8 \end{cases}$$

Based on the rest particle EDF of equation 4.26 the pressure is defined by

$$P = -\frac{c^2}{5}\left[\frac{2}{c^2}(\boldsymbol{u}\cdot\boldsymbol{u}) + 3f_0^{eq} - 3\right], \tag{4.28}$$

a function of velocity squared. The Chapman-Enskog expansion detailed in appendix A.1 yields a viscosity $\nu = \frac{c^2}{3}(\tau - \frac{1}{2})\delta t$ as well as the incompressible mass and momentum equations 4.1 and 4.2.

Remark 2 If we replace $Constant = 1$ with $Constant = 0$, the "1" is replaced by "0" in the $a = 0$ term in equation 4.26. Subsequently the "3" is replaced by "0" in equation 4.28. This pattern holds for other $Constant$ assignments. As predicted, the numerical result is the same, as verified in section 3.

4.2.3 Discussion and Comparison

The above derivation, combined with the Chapman-Enskog expansion of the appendix, has resolved several objectives of this study:

- An unambiguous EDF results;
- There is no speed of sound equation in the model, hence no need to have an equation of state for pressure and density;
- Clarity and rationale is established for the form of the EDF;
- The derivation is broadly applicable to other dimensions and lattice discretisations;
- Compressibility effects are eliminated and the model is valid for transient flows.

It is important to note that the form arrived at through this alternative approach satisfies equations 4.5 from [25]. However, other parameter values valid in equations 4.5 do not result from the ansatz approach taken here. In the next section, we show that these other parameter values are not favorable, and it is the form found in equation 4.26 that produces consistently valid results.

4.3 Numerical Results

Developing channel flow, the lid driven cavity (2D and 3D), Womersley flow, and the backward facing step serve as validation and verification tools for the form derived in the previous section. Wall boundary conditions are implemented with the halfway bounceback scheme, evaluated in He et al. [90]. Velocity inlets and moving walls are based on the revised halfway bounceback scheme of Ladd [36], where the momentum product is replaced by the form of momentum conservation of equation 4.2. Pressure boundaries are implemented with Chens extrapolation scheme [69]. Prescribed velocities are 0.1 in LB units to stay within the low Ma limit.

Additionally, alternative parameters satisfying equation set 4.5 are implemented and evaluated. The evaluated sets (σ,λ,γ) are:

$$G1 = \{3/8, 1/4, 1/8\};$$

$$G2 = \{9/20, 2/5, 1/20\};$$

$$G3 = \{7/12, 2/3, -1/12\}.$$

The work of Banda et al. [26] was also considered. In their D2Q8 stability analysis they suggest a different parametric condition from Guo et al. [25], $\lambda = 4\gamma$. While appropriate for the 8-velocity lattice, the condition lacks generality, and quickly becomes

unstable in our numerical tests. The D2Q9 EDF is no longer valid when the incompressible mass conservation principle is applied. However, the conditions presented were not designed to resolve the exact objectives we resolve in this work.

Results are found which are in line with those found by Guo et al. [25]. This is to be expected as the boundary condition impelementation is one of the few differences, and the form derived here holds the same values as Guo et al. [25] chose to employ in their numerical tests.

4.3.1 Developing Channel Flow

A uniform inlet velocity is applied on the left side of the domain, and exits three channel heights to the right. No slip walls are applied to the top and bottom infinite parallel plates. Since the length of the channel exceeds the estimated entrance length for the simulated $Re = 10$, the simulation has a simply analytic solution from White [13]: $u_x(x, H/2) = 1.5u_{in}$. The simplicity of the flow makes it a good test of the alternate sets, G1-3, as well as the order of accuracy of the method. A root mean square (RMS) residual of 5e-15 is achieved.

In table 4.1, the form derived in this work results in valid solutions while alternates result in fatal instabilities. The maximum x-velocity is in good agreement with the analytic solution, the maximum y-velocity at all grids is machine zero.

A brief look at the results in figure 4.2 shows second order accuracy, in keeping with the standard LBE evaluated by Meng and Zhang [91].

Figure 4.3 displays convergence history in the standard and incompressible LBE to demonstrate improved simulation speed in the form of the present work. For developing channel flow on a 27x9 grid the incompressible scheme achieves the convergence criterion with about 15% fewer steps. This behavior is somewhat analogous to the preconditioned LBE of Guo et al. [92], but not limited to steady flows. Additionally, for the given grid and boundary conditions the error of the standard LBE is 1.002% where the incompressible form has an error two orders of magnitude smaller.

Table 4.1
Maximum velocity and analytic error in developing channel flow.
* Indicates fatal instability.

Grid	**Present Work**		***G*1**		***G*2**		***G*3**	
	u_{max}	% Err	u_{max}	% Err	u_{max}	% Err	u_{max}	% Err
9 x 3	1.4841	1.057	1.4868	0.8784	1.4839	1.075	*	*
15 x 5	1.5070	0.4670	1.5179	1.192	1.5033	0.2214	*	*
21 x 7	1.5005	0.03580	1.5064	0.4247	1.4987	0.08547	*	*
27 x 9	1.4998	0.01653	1.5055	0.3684	1.4982	0.1221	*	*

4.3.2 Lid Driven Cavity

Incompressible flow in the lid driven cavity is well documented in literature. The geometry is simple, with only the top wall moving and all boundaries no slip flat walls. However, complex flow patterns form. Re = 100, 400, 1000 are compared

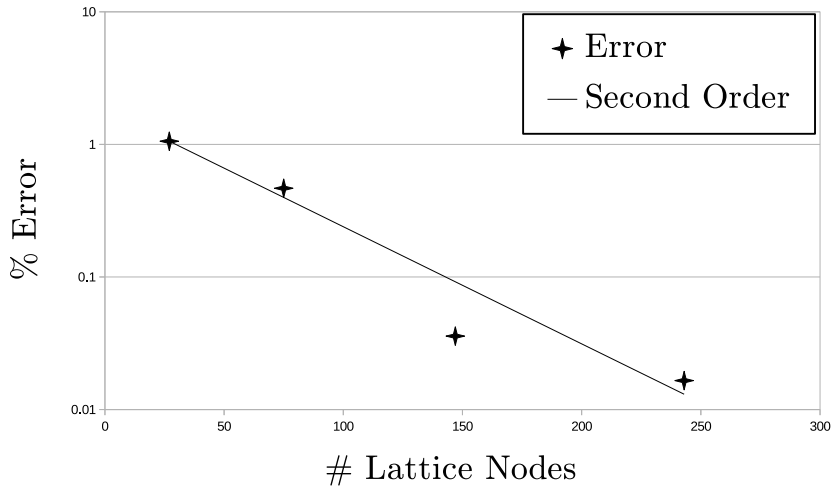

Figure 4.2: Developing channel flow convergence of u_{max} error with node count.

against the work of Marchi et al. [93]. The alternate parameter values $G1$-3 are again attempted. The grid is 257x257 and convergence is taken to RMS 1e-9.

Table 4.2 displays the reference values for comparison, table 4.3 and 4.4 display results for the present work and the first alternative set $G1$, respectively. $G2$-3 results are not presented because both proved fatally unstable at every Re. This indicates that as parameters approach those presented in this work, the solution comes closer to a proper incompressible form. The results of table 4.3 and figures 4.4 and 4.5 show excellent agreement with higher grid results from literature. For this grid, stable simulations exist to Re 5000 while the standard LBE quickly becomes fatally unstable at the same Re.

An additional important point is made in this numerical test: the LBE derived in this work satisfies the zero velocity divergence requirement ($\nabla \cdot \boldsymbol{u} = 0$). The finite

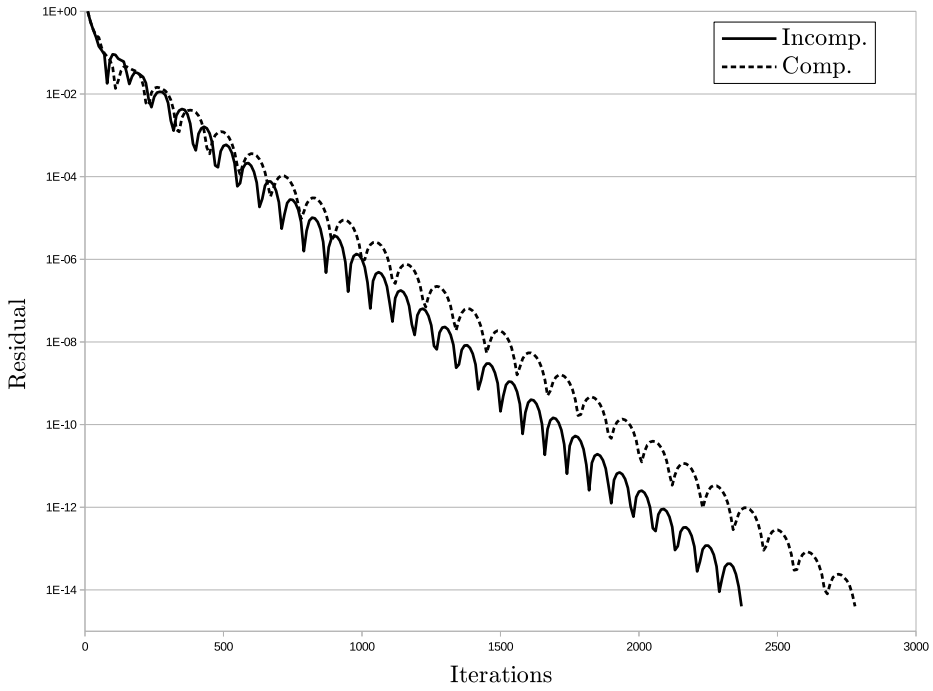

Figure 4.3: Developing channel flow residual history of standard and incompressible LBEs.

difference method is applied to each node at each time step. A second-order central differencing is performed on the interior nodes, and a second-order backward differencing scheme on the boundary nodes. To within numerical error, the zero-divergence requirement is well satisfied.

In this simulation both $Constant = 0$ and 1 have been utilized. The results are identical at every decimal place, as expected. It is only critical that a constant value is used, and the derivation is consistent throughout.

Table 4.2
Reference values from Marchi *et al.* lid driven cavity study.

Re	u_x	u_y	$\|\|\boldsymbol{u}\|\|$
100	$-2.0915\text{E}-1$	$5.7537\text{E}-2$	$2.1692\text{E}-1$
400	$-1.1505\text{E}-1$	$5.2058\text{E}-2$	$1.2628\text{E}-1$
1000	$-6.2056\text{E}-2$	$2.5799\text{E}-2$	$6.7205\text{E}-2$

Table 4.3
Center point values of lid driven cavity with velocity magnitude variance from Marchi *et al.*. Present work.

Re	**Present Work**			
	u_x	u_y	$\|\|\boldsymbol{u}\|\|$	% Diff
100	$-2.0907\text{E}-1$	$5.7547\text{E}-2$	$2.1685\text{E}-1$	$3.2270\text{E}-2$
400	$-1.1515\text{E}-1$	$5.2057\text{E}-2$	$1.2637\text{E}-1$	$7.1511\text{E}-2$
1000	$-6.2147\text{E}-2$	$2.5778\text{E}-2$	$6.7281\text{E}-2$	$1.1333\text{E}-1$

Table 4.4
Center point values of lid driven cavity with velocity magnitude variance from Marchi *et al.*. Set $G1$.

Re	**G1**			
	u_x	u_y	$\|\|\boldsymbol{u}\|\|$	% Err
100	$-2.0910\text{E}-1$	$5.7534\text{E}-2$	$2.1687\text{E}-1$	$2.3050\text{E}-2$
400	$-1.1514\text{E}-1$	$5.2061\text{E}-2$	$1.2636\text{E}-1$	$6.3351\text{E}-2$
1000	$*$	$*$	$*$	$*$

4.3.3 Womersley Flow

Pulsation of flow in a 2D channel is presented here to demonstrate the transient capability of the incompressible LBE derived here. Womersley [94] presented an analytical solution for validation. On a 41x41 grid, a time-dependent pressure difference dP is applied. The no slip walls and viscosity resist velocity field changes, but compressibility effects should not. The pressure fluctuation is governed by

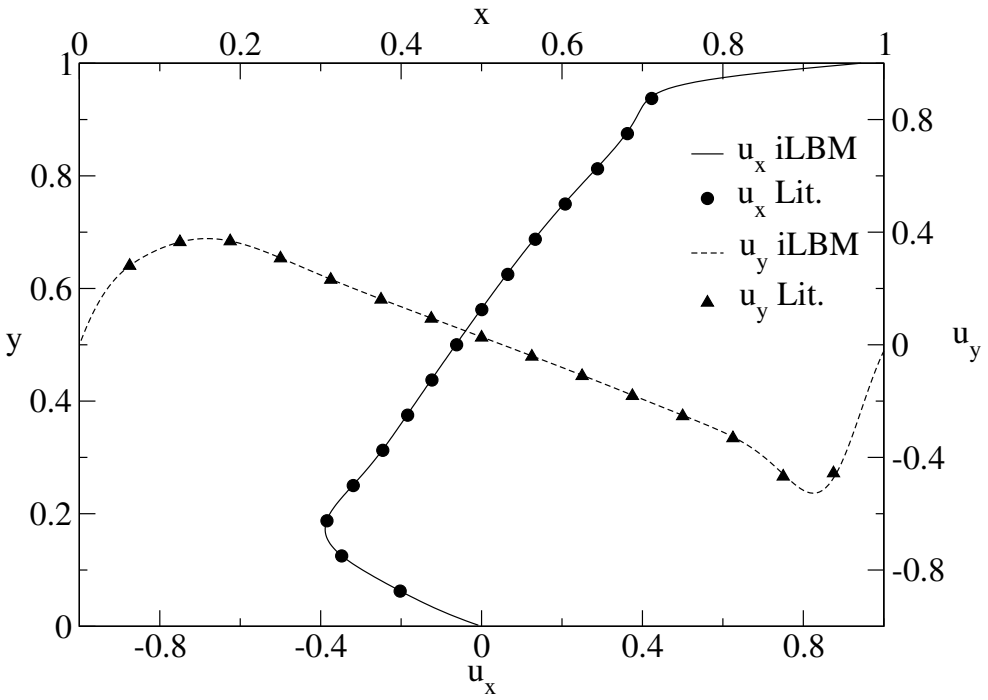

Figure 4.4: Comparison of x and y-velocities along the centerlines in the lid driven cavity flow for Re 1000 with Marchi *et al.*.

$$\frac{\partial P}{\partial x} = \mathrm{Re}\left(Ae^{i\omega t}\right) \tag{4.29}$$

where $A = dP/L_x$.

The Womersley number describes the relationship of transient inertial forces to viscous forces:

$$\alpha = L_y\sqrt{\frac{\omega}{\nu}}, \tag{4.30}$$

and is necessary in determining the analytical solution:

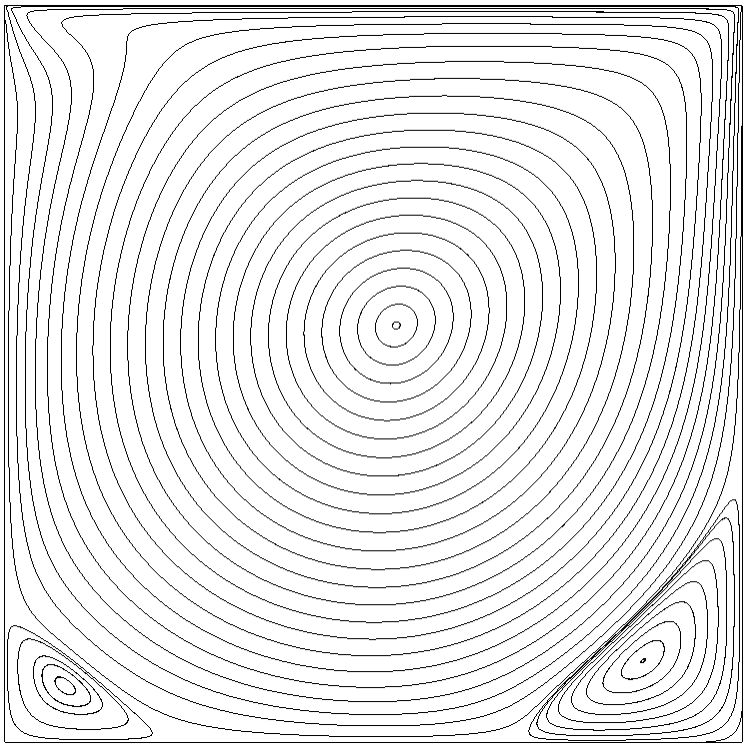

Figure 4.5: Lid driven cavity flow streamlines at Re 1000.

$$u_x(y,t) = \mathrm{Re}\left(\frac{iAe^{i\omega t}}{\omega}\left(1 - \frac{cos(\lambda(2y/L_y - 1))}{cos\lambda}\right)\right) \tag{4.31}$$

where $\lambda = \sqrt{-i\alpha^2}$. α is varied in this study by altering ω to show good time-dependent behavior, a major benefit of this approach. Additionally, to display incompressiblity, multiple values for dP are used.

Figure 4.6 displays the time dependency of velocity along the y-coordinate of the line at $x = L_x/2$ for dP =0.001 and $\alpha = 3.98$. u_{max} is determined from the Hagen-Poiseuille equation. The analytical results of equation 4.31 are shown as a solid line, and the numerical results as discrete shapes. Agreement is excellent at each 1/8

fraction of the period past 100000 time steps, and at each point along the centerline. To further validate the method and display its strengths, table 4.5 shows results as a function of dP, ω (as shown by change in α) compared with He and Luo [24]. Maximum Ma is also shown as a potential source of compressibility error amongst numerical errors. As in the transient test of Guo et al. [25], the present fully incompressible scheme results are generally one-half to a full order of magnitude better than [24]. The difference is likely due to the potential for some transient compressibility in [24], since the domain is discretised identically.

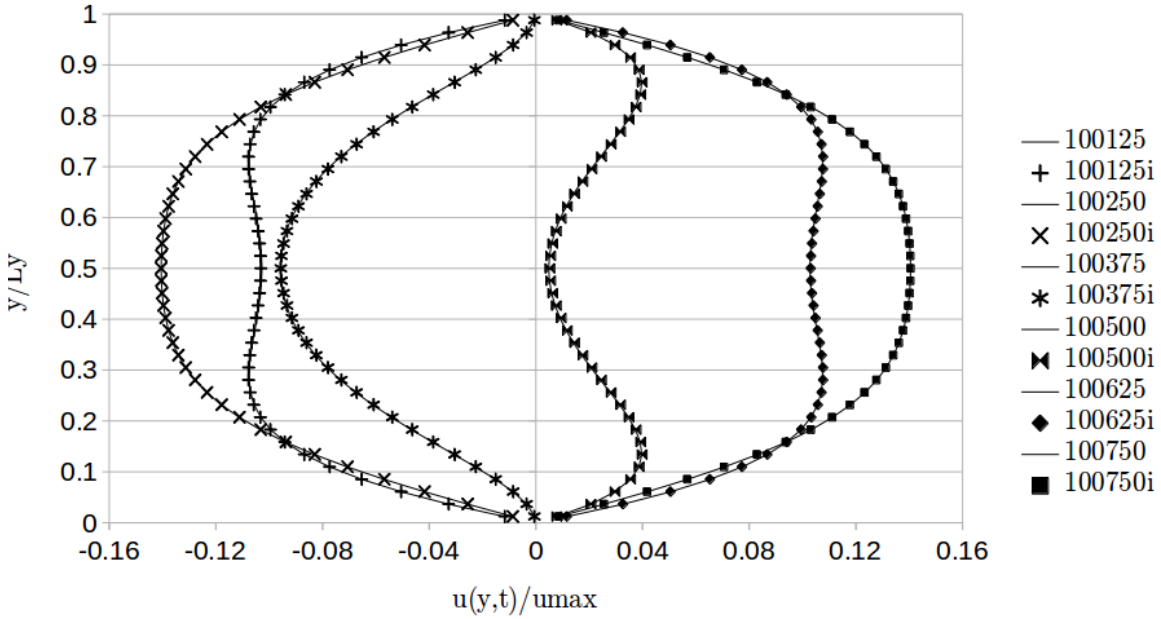

Figure 4.6: Womersley flow centerline velocity as a function of time and y.

Table 4.5
Womersley flow maximum velocity error at $x = L_x/2$ from each y point, from each $T/8$.

dP	α	Ma_{max}	% Err Present	% Err [24]
0.001	3.98	0.0449	0.00690	0.0182
0.01	3.98	0.449	0.116	0.753
0.001	6.29	0.0163	0.0258	0.247
0.01	6.29	0.163	0.134	1.02

4.3.4 Backward Facing Step

The backward facing step combines the inlet/outlet characteristics of the developing channel flow with the vortex generation and shedding nature of the lid driven cavity. Literature provides accurate values for the vortex reattachment point with a variety of Re. Here, $Re = 100$, 300, and 800 are simulated with grids 492x50, 892x90, 4002x200, respectively. Convergence is taken to RMS 1e-9. Agreement with the work of Erturk [95] for an expansion ratio of 2.0 is excellent, as seen in table 4.6.

Table 4.6
Reattachment point for the backward facing step.

Re	Present Work	Reference	% Err
100	2.920	2.922	0.06845
300	6.778	6.751	0.3999
800	11.87	11.83	0.3381

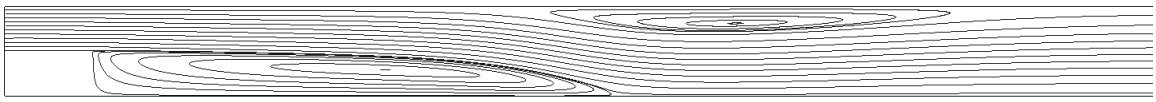

Figure 4.7: Backward facing step streamlines for Re 800.

4.3.5 3D Lid Driven Cavity

For 3D verification the procedure laid out in section 2 must be utilized on the D3Q19 lattice (figure 4.8) with weights

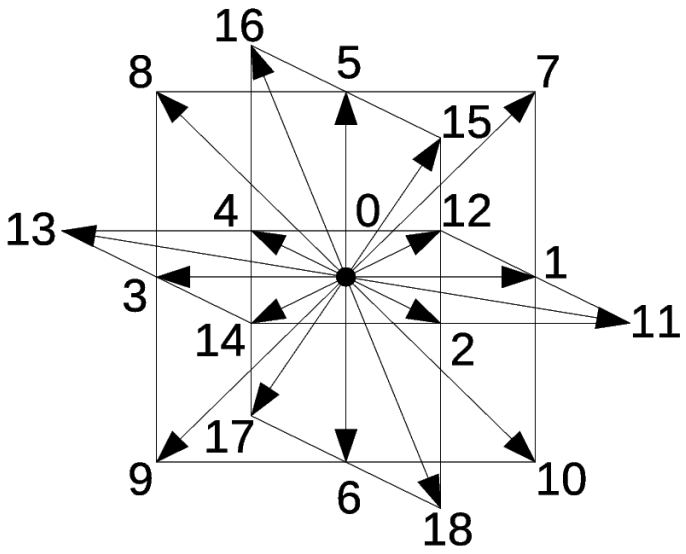

Figure 4.8: D3Q19 Lattice.

$$w_a = \begin{cases} \frac{1}{3} & \text{for} \quad a = 0 \\ \frac{1}{18} & \text{for} \quad a = 1 - 6 \\ \frac{1}{36} & \text{for} \quad a = 7 - 18 \end{cases}$$

The resultant EDF with $\sum f_a^{eq} = 0$ is

$$f_a^{eq} = \begin{cases} 1 - 2P/9c^2 + S_a(\boldsymbol{u}), & a = 0 \\ P/54c^2 + S_a(\boldsymbol{u}), & a = 1 - 6 \\ P/108c^2 + S_a(\boldsymbol{u}), & a = 7 - 18 \end{cases} \tag{4.32}$$

where $S_a(\boldsymbol{u})$ is defined in equation 4.27. Pressure is derived in the same way, and is now

$$P = -\frac{9c^2}{2}\left[\frac{1}{2c^2}(\boldsymbol{u}\cdot\boldsymbol{u}) + f_0^{eq} - 1\right]. \tag{4.33}$$

With these parameters definitively resolved, the 3D cubic lid driven is solvable. The cavity is defined with no slip stationary walls except for the top, translating in the $+x$ direction, and 101^3 nodes. For Re 100 and 400 the results compare excellently with the incompressible work of Wong and Baker [96]. u_x values along the z-direction on a line at $x = y = 0$ are plotted in figures 4.9 and 4.10, where the center of the cavity is the datum $(0, 0, 0)$. Convergence is taken to RMS 1e-6. Additionally, velocity vectors are plotted on the plane placed at y=0 in figures 4.11 and 4.12.

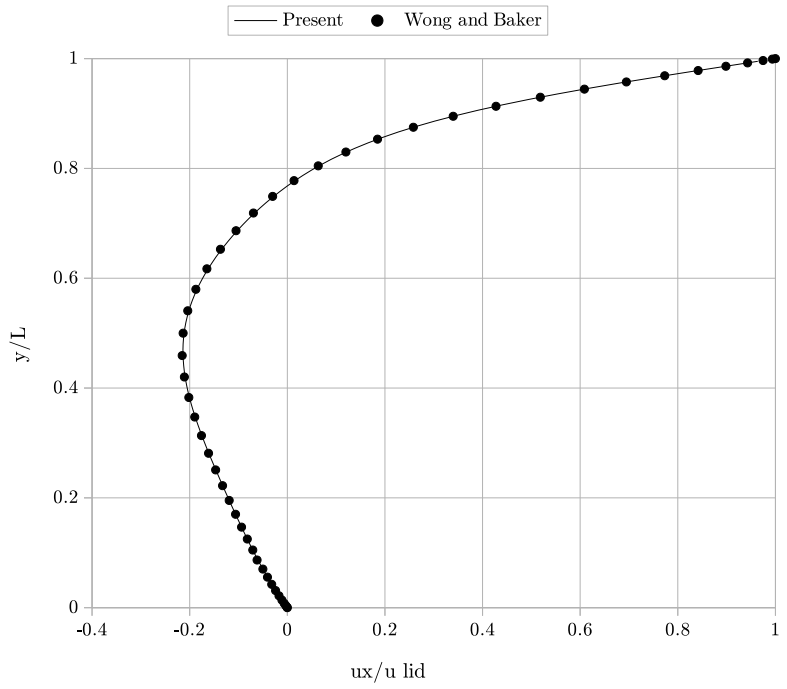

Figure 4.9: 3D lid driven cavity Re 100 x-velocity along the line y=x=0

4.4 Conclusions

This paper presents an alternative approach to deriving an incompressible lattice Boltzmann equation for steady and unsteady flow simulations by utilizing appropriate ansatzes. The result is a single form of the equilibrium distribution function which recovers the fully incompressible Navier-Stokes equations through the multi-scale Chapman-Enskog expansion. The explicit procedure was extended to additional dimensions and lattices. No speed of sound equation is needed in this model, hence no equation of state is needed. Canonical flow simulations yield results in good agreement with the incompressible analytical solutions and literature. The numerical

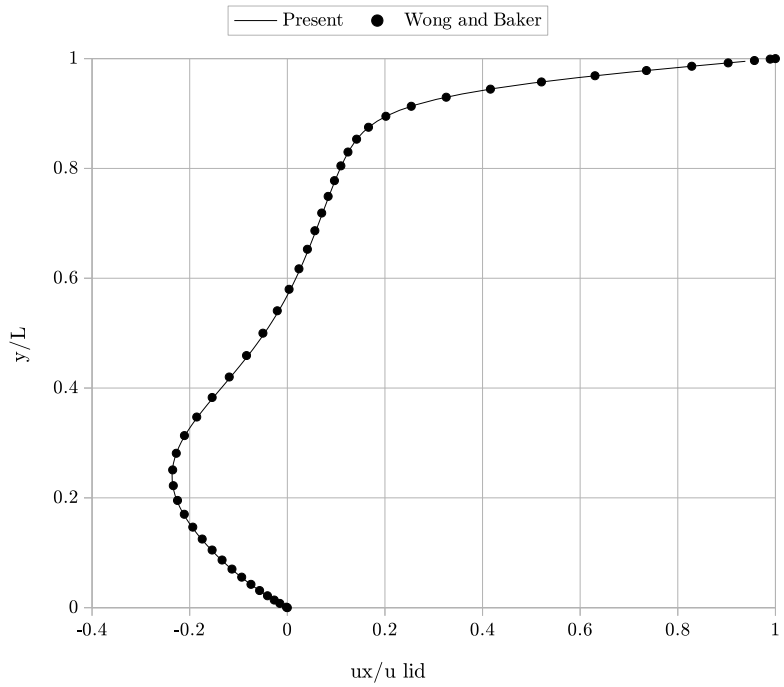

Figure 4.10: 3D lid driven cavity Re 400 x-velocity along the line y=x=0.

results also show that alternate parameters and forms in previous literature are not as favorable, and that there is an advantage over pseudo-incompressible and compressible forms. The form presented here is thus clarified as necessary for incompressible physics within the lattice Boltzmann method.

4.5 MRT-iLBE for the D2Q9 Form

For accurate representation of small passages in porous media (chapters 6 and 7) and stability of high-Re (chapter 5) aspects of this work, an MRT version of the iLBE derived above is required. Appendix A.2 combines the results of section 4.2.2

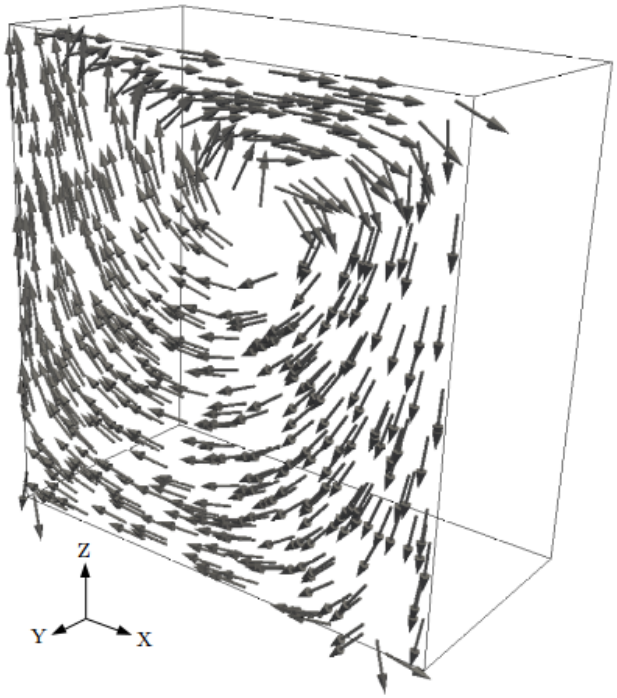

Figure 4.11: 3D lid driven cavity Re 100 velocity at y=0.

with the procedure of Bouzidi *et al.* [72] to produce an MRT-iLBE without density variation. Verification of the scheme is performed in the relevant chapters (5-6) by utilizing porous medium experimental fits, and numerical values from literature on Hopf bifurcation with increasing Re.

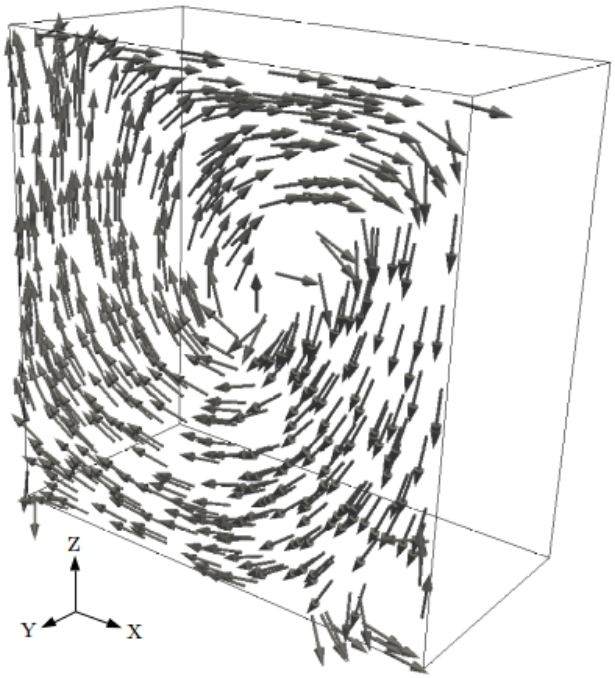

Figure 4.12: 3D lid driven cavity Re 400 velocity at y=0.

Chapter 5

2D DNS and 3D LES with the iLBE[1]

Chapter 4 presented an unambiguous iLBE which can resolve the compressibility error of previous turbulence studies within the LBM such as [29, 30]. To simulate macroscopic incompressible chaotic and transition flows the initial study utilizes an approach without modeling (DNS) by resolving the smallest length scales approximated by Kolmogorov [76]. The 2D lid driven cavity is utilized due to the plethora of literature on transition and turbulence [78–81], and for computational efficiency due to the high node count.

[1]Material contained in this chapter was previously published in *Advances in Applied Mathematics and Mechanics* [3].

It is acknowledged here that turbulence is a fundamentally 3D phenomenon. However, solutions across a variety of regimes in fewer than three dimensions are mathematically valid tests of method accuracy and stability. Analogous features of 3D turbulence exist in 2D, such as bifurcations leading to increasing levels of instability, transition, Re as a driving parameter for instability amplitude, and chaotic non-repeating time histories. These characteristics are well established in the citations of the previous paragraph.

In order to explore the 3D characteristics of transition the Vreman SGS LES approach [82] is utilized in a cubic lid driven cavity. While every scale of transition and turbulence is desired in a simulation (as in DNS), the smallest scales play little role in meaningful results [76] while driving computational costs to intractable levels. The SGS provides the increased viscous diffusion these small scales contribute when not resolved. A Smagorinsky-Lilly SGS is inappropriate when transition is involved [82], therefore the locally varying and potentially vanishing Vreman model is implemented with the iLBE here. As a result, this study adds to the knowledge which was previously dominated by the original compressible LBE and standard Smagorinsky SGS [97].

5.1 Transition Flow with an Incompressible Lattice Boltzmann Equation (2D DNS)[2]

Abstract

Direct numerical simulations of the transition process from steady laminar to chaotic flow are considered in this study with the relatively new incompressible lattice Boltzmann equation. Numerically, a multiple relaxation time fully incompressible lattice Boltzmann equation is implemented in a 2D driven cavity. Spatial discretization is 2nd-order accurate, and the Kolmogorov length scale estimation based on Reynolds number (Re) dictates grid resolution. Initial simulations show the method to be accurate for steady laminar flows, while higher Re simulations reveal periodic flow behavior consistent with an initial Hopf bifurcation at Re 7,988. Non-repeating flow behavior is observed in the phase space trajectories above Re 13,063, and is evidence of the transition to a chaotic flow regime. Finally, flows at Reynolds numbers above the chaotic transition point are simulated and found with statistical properties in good agreement with literature.

[2]The material contained in this section was previously published in *Advances in Applied Mathematics and Mechanics* [3].

5.1.1 Introduction

Characteristics of flow transition from steady state to transience and from transience to self-sustaining chaos and instability is an active area of research. While transition to chaos (turbulence in 3D) and separation remain unsolved problems in engineering flow analysis, direct numerical simulation (DNS) work continues to provide insight to the physics in an effort to develop improved turbulence transition and separation models. Past application of the lattice Boltzmann method to chaos and turbulence simulation, such as channel flow by Lammers *et al.*, suffered from the compressibility error [29, 30] inherent in the standard lattice Boltzmann equation [20, 27]. This work extends the study of transitional flow states using an incompressible lattice Boltzmann method (iLBM) and a Multiple Relaxation Time (MRT) collision operator. Although physical turbulence is a three dimensional phenomenon, solutions to the flow equations in two dimensions can exhibit similar randomness.

Bifurcations, chaos, and energy dissipation, among other characteristics, exist, while vortex stretching is absent. With this in mind, this work provides a numerical solution benchmark using MRT-iLBM for comparison with past 2D work.

The Lattice Boltzmann Method (LBM) is a relative newcomer in the field of Computational Fluid Dynamics (CFD), having been first described in 1988 [18]. This

class of analysis methodology can take many forms. For continuum flow analysis, parameters are chosen such that numerical solutions to the Navier-Stokes equations are recovered through solving the discrete Boltzmann equation. While the behavior of Navier-Stokes is replicated by LBM, the underlying solver algorithms for LBM are considerably simpler than an equivalent Navier-Stokes solver. Reduced computations-per step reduce overall roundoff error and make the MRT-iLBM a less numerically noisy solution method [31].

Lid-driven cavity flow (LDC) is a canonical flow case useful in evaluating methodology [98]. Literature reporting results for steady and transient laminar, transitional, and chaotic flows using a wide variety of methods is extensive. The complexity of the flow despite simple boundaries, along with the plethora of results, makes it an excellent verification tool. Steady state results were obtained by Ghia *et al.* [99] using a vorticity-stream function approach up to moderate Reynolds numbers. More recently, fine-grid results were reported by Marchi *et al.* [93] using finite volume Navier-Stokes. LBM has been applied to the LDC flow in the past by Hou *et al.* [100], who point out the compressibility error present in their results.

Past studies of 2D driven cavity flow have reported various values for the Reynolds number at the onset of transient behavior, dependent on the balance of noisiness and dissipation of the numerical method used. Cazemier *et al.* [80] analyzed this flow using both DNS and a reduced-order model deduced from Proper Orthogonal

Decomposition of a DNS simulation performed at Re 22,000. Peng *et al.* [78] reported the Reynolds numbers of the first Hopf bifurcation and the turbulence transition, but the sixth order numerical method applied in the domain center was contaminated by larger error terms from the second order spatial scheme applied at the boundaries. It is possible that numerical noise from the combination of low-order accurate numerics and typical grid resolution at the walls - where the highest gradients occur - served as a source of artificial excitation and contributed error to the determination of transitional Re. Marie *et al.* [101] show the dispersion and diffusion error of LBM to be excellent across all wavenumbers, suggesting it is well-suited for DNS analysis.

Several authors report steady solutions of the 2D lid driven cavity flow at Reynolds numbers upwards of 30,000 by omitting time dependency terms in the modeled equations. Failure of these simulations to allow solution unsteadiness belies the fact that the existence of steady flow depends upon Reynolds number-dependent stability criteria. Solution unsteadiness below Re 10,000 has been well established since at least the work of Cazemier *et al.* [80].

The objectives of this work are to establish the MRT-iLBM method as an accurate approach for DNS and compute critical low- to moderate-Reynolds number results using the method. These objectives will be accomplished by first verifying the MRT-iLBM method by showing agreement with literature results for steady, laminar 2D LDC flow. Subsequent objectives include identifying the Reynolds number of the first

Hopf bifurcation (the onset of transience) and the Reynolds number of the transition to self-sustaining chaos, respectively, and compare with literature results. Lastly, MRT-iLBM results of DNS at two chaotic Reynolds numbers are reported. Statistical results for these simulations are compared with literature; they are informative about the flow structure but also demonstrate the ability of MRT-iLBM to be effective for performing DNS.

5.1.2 Incompressible Multiple Relaxation Time Lattice Boltzmann Equation

The standard and incompressible lattice Boltzmann equation (LBE) have the same basic form:

$$f_i(\boldsymbol{x} + \delta\boldsymbol{x}, t + \delta t) = f_i(\boldsymbol{x}, t) - \frac{1}{\tau}\left(f_i - f_i^{eq}\right) \tag{5.1}$$

where f_i are the probability distributions of discrete velocity space, τ is the collision relaxation time, and f_i^{eq} is the equilibrium distribution [20].

Whether one arrives at a compressible flow in the incompressible limit, or a truly incompressible flow depends on the equilibrium distribution term [27]. In the standard

LBE this term takes the form:

$$f_i^{eq} = \omega_i \rho \left(1 + \frac{\boldsymbol{c}_i \cdot \boldsymbol{u}}{c_s^2} + \frac{(\boldsymbol{c}_i \cdot \boldsymbol{u})^2}{2c_s^4} - \frac{(\boldsymbol{u} \cdot \boldsymbol{u})}{2c_s^2} \right) \tag{5.2}$$

where $\boldsymbol{c}_i$ are the lattice velocities vector, $\boldsymbol{u}$ is the flow velocity vector, ρ is the density, ω_i are the distribution weights, and c_s is the speed of sound for a given lattice. For flows utilizing this formulation, the pressure is defined as $P = c_s^2 \rho$, and the relaxation time is related to the kinematic viscosity as $\nu = c_s^2 \left(\tau - \frac{1}{2} \right) \delta t$ [20].

The following mass and momentum conservation laws are then satisfied:

$$\sum_i f_i = \rho \ , \quad \sum_i \boldsymbol{c}_i f_i = \rho \boldsymbol{u}. \tag{5.3}$$

For this study, 2D physics is simulated with nine discrete velocities abbreviated as $D2Q9$. Figure 5.1 graphically demonstrates the $D2Q9$ lattice. The velocity vectors are then:

$$c_x = \{0, 1, 0, -1, 0, 1, -1, -1, 1\}, \quad c_y = \{0, 0, 1, 0, -1, 1, 1, -1, -1\}. \tag{5.4}$$

Weights ω_i correlate inversely with magnitude of each vector:

$$\omega_0 = \frac{4}{9}, \quad \omega_{1,2,3,4} = \frac{1}{9}, \quad \omega_{5,6,7,8} = \frac{1}{36}. \tag{5.5}$$

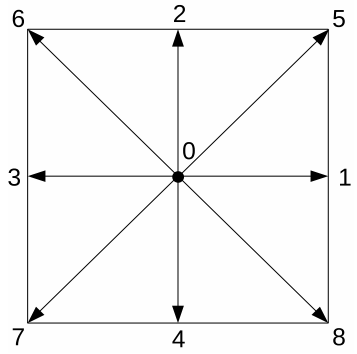

Figure 5.1: $D2Q9$ lattice structure

To resolve the issue of compressibility present in the standard LBE, the equilibrium distribution can be modified by replacing the conservation equations of formulation 5.3 with [1, 25, 27]:

$$\sum_i f_i = Constant, \quad \sum_i \boldsymbol{c}_i f_i = \boldsymbol{u}, \quad \boldsymbol{uu} + \frac{P}{\rho_0}\boldsymbol{I} = \sum_i \boldsymbol{c}_i \boldsymbol{c}_i f_i \tag{5.6}$$

and with *Constant* set to 1, the equilibrium distribution function becomes:

$$f_i^{eq} = \begin{cases} 1 - \frac{5}{3}\frac{1}{c^2}P + S_i, & \text{for} \quad i = 0 \\ \frac{1}{3}\frac{1}{c^2}P + S_i, & \text{for} \quad i = 1,2,3,4 \\ \frac{1}{12}\frac{1}{c^2}P + S_i, & \text{for} \quad i = 5,6,7,8 \end{cases} \tag{5.7}$$

$$S_i = \omega_i \left[3\frac{(\boldsymbol{c}_i \cdot \boldsymbol{u})}{c} + \frac{9}{2}\frac{(\boldsymbol{c}_i \cdot \boldsymbol{u})^2}{c^2} - \frac{3}{2}\frac{(\boldsymbol{u} \cdot \boldsymbol{u})}{c^2} \right], \tag{5.8}$$

which recovers the fully incompressible hydrodynamic equations for the $D2Q9$ case and yields for the lattice speed and kinematic viscosity $c = \frac{\delta x}{\delta t}$ and $\nu = \frac{c^2}{3}\left(\tau - \frac{1}{2}\right)\delta t$, respectively. Pressure is calculated from:

$$P = \frac{3c^2}{5}\left[1 - f_0^{eq} + S_0\right] \tag{5.9}$$

LBM fundamentals presented thus far have utilized the single relaxation time (SRT) Bhatnagar-Gross-Krook (BGK) collision model [66]. With increasing Re, stability and boundary location become problematic in the SRT-LBE [72]. While instability is reduced with the iLBE, a multiple relaxation time form further improves LBM for transitional and chaotic flows, as in this study. The MRT-iLBE is expressed as:

$$f_i\left(\boldsymbol{x} + \delta\boldsymbol{x}, t + \delta t\right) = f_i(\boldsymbol{x}, t) - \sum_j \Lambda_{ij}(f_j - f_j^{eq}), \tag{5.10}$$

with Λ_{ij} replacing the inverse SRT value, $\frac{1}{\tau}$. Several values of the new collision matrix are functions of τ. Computations actually occur in moment space, in which each moment has a physical correlation, and are then transformed back to velocity

space for macroscopic meaning. Appendix A.2 contains the derivation and complete components of the MRT-iLBE used for this study.

5.1.3 Simulation Parameters

The lid driven cavity configuration as simulated in this work is shown in Figure 5.2. The four walls of the cavity were treated with second order accurate halfway bounce back (HBB) boundary conditions [102]. Simulation similarity is governed by Reynolds number Re shown in Eq. 5.11. Characteristic time t_c is computed according to Eq. 5.12. These relations contain symbols for wall velocity ($\boldsymbol{u}_{wall}$) and kinematic viscosity (ν). The subscript lb signifies that the value used is in lattice Boltzmann units. Numbers presented throughout this work are nondimensional unless otherwise indicated.

$$Re = \frac{\boldsymbol{u}_{wall,lb} L_{lb}}{\nu_{lb}} \tag{5.11}$$

$$t_c = \frac{L_{lb}}{\boldsymbol{u}_{wall,lb}} \tag{5.12}$$

Since the numerics employed are second order both at the boundaries and domain

interior, flow feature resolution for this DNS simulation is dependent upon high lattice site counts. This contrasts with the use of larger grid spacing and a higher order spatial differencing based on the flow solution following a given polynominal order between the nodes. Kolmogorov's theory of turbulent length scales is the basis for discretizing each direction by $Re^{0.75}$ lattice sites as the standard grid sizing used in this work, including flow in the laminar regime.The accuracy of this approximation is reported upon with the results of the chaotic flows at Re 15,000 and Re 20,000. A grid dependence check at Re 1,000 is done to show that the MRT-iLBM method is comparable to literature results at lower spatial resolution.

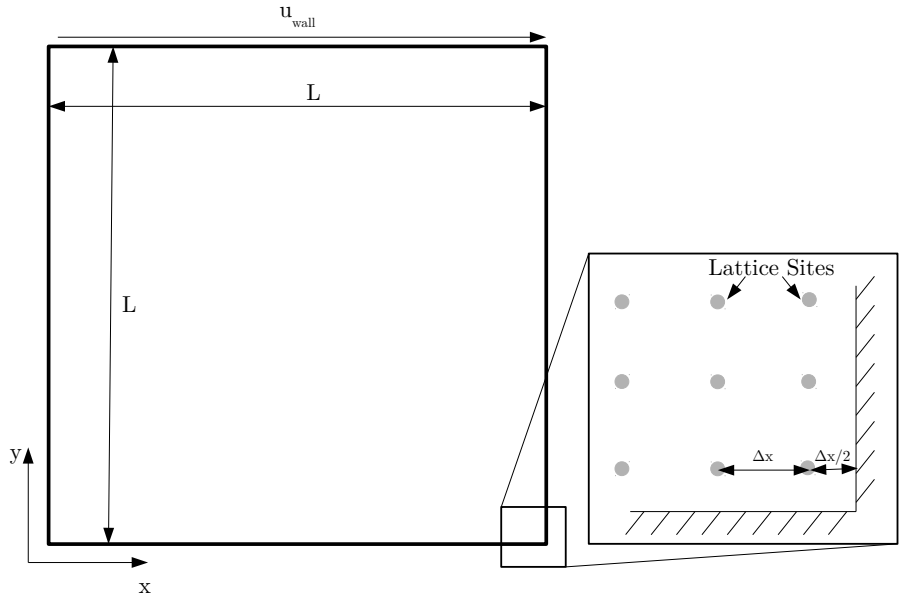

Figure 5.2: Lid driven cavity simulation setup and detail of HBB boundary condition

All simulations were started from at-rest initial conditions. As such, there was a burn-in period during which the mean flow values changed as the flow reached a steady

state or quasi-steady oscillatory condition. All data presented in this work was taken after the burn-in time was complete.

User specified Reynolds numbers and grid sizes were used to determine the requisite kinematic viscosity according to Eq. 5.11 . Wall velocity was held at the constant value of 0.1 throughout these simulations.

Low Reynolds numbers with steady results (Re 100, 400, 1,000) were simulated to validate the MRT-iLBM code. Comparison of these steady results with literature are given in the Results section. The first Hopf bifurcation was identified by interpolating from transient result data from Reynolds numbers just above the bifurcation Re. To determine the Reynolds number of the transition to chaos, one non-random transient Reynolds number and one chaotic (random and transient) Reynolds number were found, and then a binary search was performed successively until the desired accuracy was achieved. Fully chaotic results were then generated at two higher Reynolds numbers to provide DNS data for the statistical analysis.

5.1.3.1 Post Processing

Statistical properties of the chaotic flows are generated by a series of post-processing codes which made computations from sets of both macroscopic (u,v) and mesoscopic (f_i) data which were output periodically as the MRT-iLBM code ran. Data included

in the statistics met two conditions. First, the mean values of the code were required to be in a steady state which only existed beyond a minimum *burn-in time*. Second, the frequency of data output was required to be adequate to capture the highest frequency components of the system response and not produce aliasing.

Mean velocities are computed by averaging each of the i velocity components, whose instantaneous value is written U_i, at each time step k (N total) for all flow snapshots available. Eq. 5.13 describes the average for U_i and the pressure P, which has an analogous computation. The square of the fluctuating i^{th} velocity component of velocity u_i^2 is computed from the mean and the available snapshot data.

$$\langle U_i \rangle = \frac{1}{N} \sum_{k}^{N} U_i^k \qquad\qquad \langle P_i \rangle = \frac{1}{N} \sum_{k}^{N} P^k \tag{5.13}$$

$$\langle u_i^2 \rangle = \frac{1}{N} \sum_{k}^{N} \left(U_i^k - \langle U_i \rangle \right)^2 \tag{5.14}$$

$$AR = \sqrt{\frac{\langle u_1^2 \rangle}{\langle u_2^2 \rangle}} \tag{5.15}$$

To assess the anisotropy in the chaotic flows, the ratio of RMS components of fluctuating velocity was computed per Eq. 5.15. This quantity is referred to as the

anisotropy ratio, AR. According to the definition, AR is the multiplier between RMS fluctuating velocity in the x direction and RMS fluctuating velocity in the y direction; and shows how various regions of the flow field are dominated by one fluctuating velocity component or the other.

Local strain rate tensor components S_{ij} were computed based on the work of Li and Wang [103]. Namely, the mesoscopic properties of the flow were incorporated into the components of the 2D strain rate tensor as shown in Eq. 5.16. Data files periodically output by the code contained instantaneous snapshots of the strain rate tensor field at each lattice site in the domain. A code was run post-process to compute the mean and the mean fluctuating components of the strain rate tensor, $\langle S_{ij} \rangle$ and s_{ij}, respectively. What we will call the turbulence kinetic energy dissipation ϵ for 2D flows, was computed according to Equation 5.17.

$$S_{ij} \approx \frac{-3}{2\rho c^2 \tau \Delta t} \sum_{\alpha} c_{i,\alpha} c_{j,\alpha} \left(f_{post,\alpha} - f_{\alpha}^{eq} \right) \tag{5.16}$$

$$\epsilon = 2\nu \langle s_{ij} s_{ij} \rangle \tag{5.17}$$

Kolmogorov length scale was computed for each lattice site in the domain according to the relation given in Equation 5.18. η_k quantifies the spatial resolution of the

simulation; values less than one indicate that the smallest and shortest-lived flow features are not fully captured.

$$\eta_k = \left(\frac{\nu^3}{\epsilon}\right)^{\frac{1}{4}} \tag{5.18}$$

Phase space diagrams provide one tool for assessing the flow state. Namely, traces which converge to a single point are steady state, those which repeat the same values periodically are simply transient, and those which display non-repeating behavior are chaotic. Put another way, the random aspect of post-transition flows are identified when an arbitrarily large number of terms can be included in a predictive model without achieving arbitrarily accurate solutions for any later time.

5.1.4 Results

5.1.4.1 Verifying MRT-iLBM with steady LDC Flow

Steady-state results from the MRT-iLBM method at three Reynolds numbers are compared with literature results in order to check the correctness of the MRT-iLBM code. Table 5.1 shows the x and y velocity components of the MRT-iLBM computations and the same from recent literature. Additionally the resultant velocity

components are listed, and the percent difference between literature and MRT-iLBM resultant velocities are shown to be small, less than 0.15% for the three Reynolds numbers considered.

Figure 5.3 provides a more complete picture of the velocity profile comparison for *Re* 1,000. Both x and y velocity components are plotted for both MRT-iLBM and literature results. The good agreement between the two demonstrates both accuracy of the MRT-iLBM and adequacy of the lattice discretization to capture near-wall gradients.

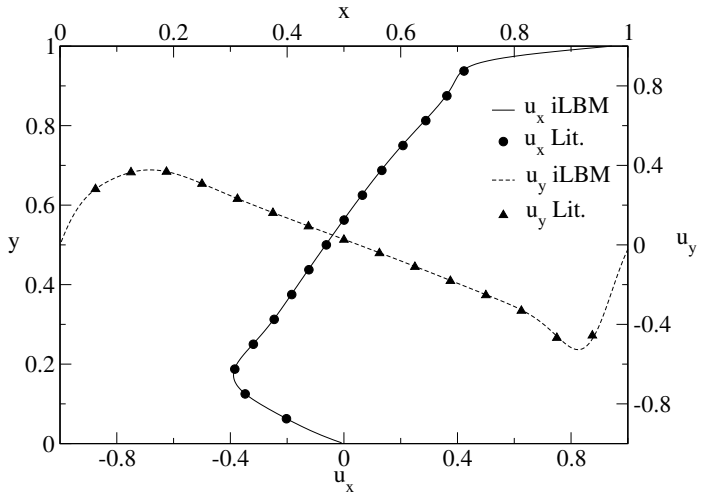

Figure 5.3: Re 1,000 velocity profiles: u velocity at $x = 0.5$, v velocity at $y = 0.5$, iLBM and Marchi et al.

Table 5.1
Steady-State Predictions of iLBM Match Literature to within 0.2%

Re	iLBM			[93]			$\|\|\boldsymbol{u}\|\|\%diff$
	u_x	u_y	$\|\|\boldsymbol{u}\|\|$	u_x	u_y	$\|\|\boldsymbol{u}\|\|$	
100	-2.091e-1	5.754e-2	2.169e-1	-2.091e-1	5.754e-2	2.169e-1	-0.003
400	-1.152e-1	5.206e-2	1.263e-1	-1.151e-1	5.206e-2	1.262e-1	0.081
1,000	-6.219e-2	2.578e-2	6.732e-2	-6.206e-2	2.580e-2	6.720e-2	0.176

The final point on steady laminar flow analysis is to compare the LBM-iMRT results to literature results on a comparable grid. Using the Marchi[93] result as the baseline for comparison, Table 5.2 shows that the current method produces comparable results (within 1.2%) on the coarser 100x100 grid. Thus, equivalence between this method and Navier-Stokes based codes for non-DNS simulations is demonstrated. Secondly, the minor difference in results between the coarser and finer grids using the present method show that the spacing criteria used produces grid independent results to within one percent.

Table 5.2
Comparison between literature and the current method on a coarse grid at Re 1,000

	u_x	u_y	$\|\|\boldsymbol{u}\|\|$	$\|\|\boldsymbol{u}\|\|\%diff$
Ghia[99] (129x129)	-6.080e-2	2.526e-2	6.584e-2	-2.02
Marchi[93] (1024x1024)	-6.205e-2	2.579e-2	6.720e-2	-
This work (coarse grid, 100x100)	-6.292e-2	2.565e-2	6.795e-2	1.12
This work (nominal grid, 178x178)	-6.219e-2	2.578e-2	6.732e-2	0.19

5.1.4.2 The First Hopf Bifurcation and Transition to Chaos

The first Hopf bifurcation point is the Reynolds number at which the flow changes from a steady solution to one which shows oscillatory behavior. Following the method of Cazemier *et al.* [80], the bifurcation point can be predicted by using the change in the square of signal oscillation amplitude A_{amp}^2 with Reynolds number to determine the point at which A_{amp}^2 goes to zero. In this case A_{amp} was taken to be equal to the difference between maximum and minimum values of u velocity at point (0.6,0.6).

Oscillation amplitudes were taken from MRT-iLBM simulations of flow at Re 8,100, 8,200, and 8,300 on grids of 854x854, 862x862, and 870x870 respectively. Figure 5.4a shows the progression of the phase space plots in question. Potential sensitivity of oscillation amplitude to changes in the spatial discretization was checked by performing two simulations at Re 9,000. The first simulation used the nominal grid sizing of this work ($Re^{0.75}$ lattice sites in each direction - a 925x925 grid), and the second reduced the grid count by 25%. Oscillation frequency and amplitudes were identical between the two, whereas the mean was reduced by 0.3% in the lower resolution case. Through this, the $Re^{0.75}$ estimate was deemed as acceptable for grid independence.

Figure 5.4b shows the linear interpolation based on the square of oscillation amplitude data from the three Reynolds numbers named above. As has been observed previously [80], the oscillation amplitude grows with the square of the Reynolds number beyond the first Hopf bifurcation, so the use of a linear interpolation based on the square is appropriate. The intersection of this curve fit equation with 0 oscillation amplitude was then taken as the first Hopf Bifurcation point for this case, and it is predicted to occur at Re 7,988 by the MRT-iLBM. This value is corroborated by the fact that the flow at Re 8,000 showed a nonzero but very small oscillating amplitude. Error was estimated by fitting a second order polynomial to data points at Re 8,100, 8,200, and 8,300 and computing the difference between the zero amplitude Reynolds number of that equation and the linear interpolation method. The Re_{Hopf} predicted by this second order polynomial is 8,007. This difference being indicative of the leading error

term for the linear interpolation, the uncertainty of ± 19 is associated with the linear interpolation estimate of 7,988.

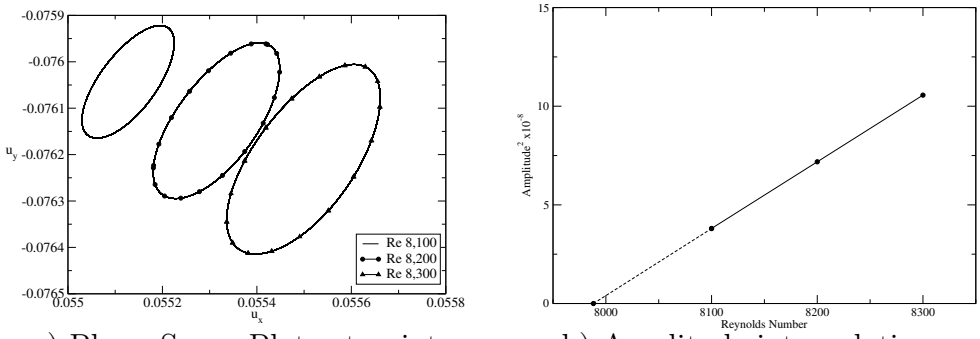

a) Phase Space Plots at point (0.6,0.6)

b) Amplitude-interpolation method predicts $Re_{Hopf} = 7,988$

Figure 5.4: Results for Re 8,100 - 8,300 and their use for predicting the onset of transience

Table 5.3
Summary of literature Hopf bifurcation predictions for 2D lid driven cavity

Reference	Methodology	Re_{Hopf}
[80]	Oscillation amplitude interpolation to zero, N-S DNS	7,972
[80]	POD model prediction by model constructed from Re 22k DNS results	7,819
[78]	Interpolation to zero amplitude, 200x200 grid, 6^{th} order inner, 2^{nd} order bc's	7,704
[79]	Direct dynamical system stability analysis	7,763
[81]	Lyapunov Stabilty Analysis	8,000 - 8,050
This Study	Interpolation to zero amplitude, MRT-iLBM DNS	7,988 ± 19

Table 5.3 summarizes literature which predicted the first Hopf bifurcation of the 2D lid driven cavity flow according to the method used and the reported Reynolds number of the bifurcation. The Re_{Hopf} result of this work agrees well with the prior DNS simulation of Cazemier *et al.* [80], and the Lyupanov stability analysis of Bruneau and Saad [81]. While within 4% of the previous results, the results of Peng *et al.* [78], Poliashenko and Aidun [79], and the POD-based prediction of Cazemier *et al.* [80]

are somewhat lower than the value reported here. The POD method of Cazemier *et al.* was a valuable and informative exercise in mathematics but not useful as a tool for general flow analysis.

Peng *et al.* [78] embellishes upon the bifurcation behavior of the LDC flow solution at Reynolds numbers between Re_{Hopf} and the Re 11,000. It is known that the flow undergoes bifurcations to become two-periodic and then one-periodic as the Reynolds number is increased beyond the first Hopf bifurcation. Eventually stability conditions in the flow change such that perturbations are not damped out over time, but cause further flow perturbations. Transition to chaos is assessed by checking how faithfully the phase space traces repeat the same circuit. Figure 5.5 shows the difference in phase space plots between two Reynolds numbers which lie on either side of transition. Both plots capture 1 million time steps and a few tens of characteristics times of the flow; the flow at Re 13,000 has perfect repeatability of the solution. Alternatively, Re 13,125 is identifiable as post-transitional because of the lack of any repetition in the phase space trace.

5.1.4.3 Post-Transition Statistics

This section reports results of DNS simulations at two high, post-transition, Reynolds numbers: Re 15,000 and Re 20,000. Per the Kolmogorov length estimate, the Re 15,000 case was run on a 1356 x 1356 grid and the Re 20,000 case on a 1,682 x

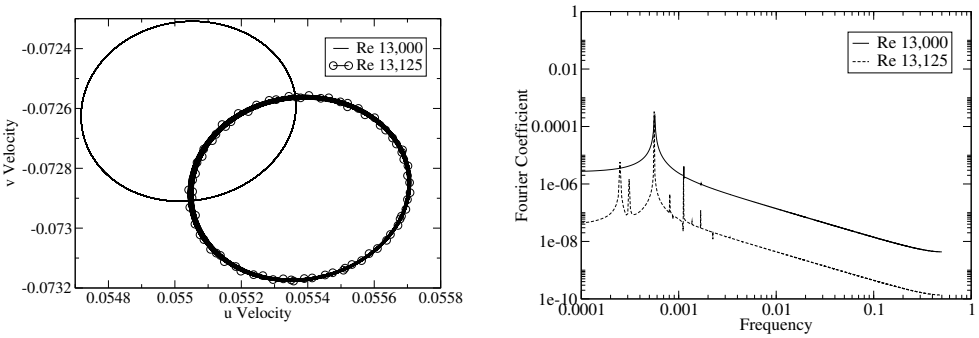

a) Phase Space Result b) Frequency Spectrum Result

Figure 5.5: Results from point (0.6,0.6) before transition (*Re* 13,000) and after (*Re* 13,125)

1,682 grids with uniform lattice spacing and the halfway bounce back (HBB) boundary condition as shown in Figure 5.2. Statistical results for mean flow, turbulence kinetic energy (2D version) (tke), turbulent energy dissipation ϵ (2D version), the Kolmogorov length scale η_k, and the anisotropy of the instabilities are presented.

Figure 5.6 shows the statistical results from *Re* 15,000. Mean streamlines show good agreement with published results, including capture of the very small self- contained mean flow circulation zones in the bottom corners of the domain. ϵ shows high values near the top right corner of the domain where flow from the driven wall impinges upon the neighboring non-moving wall. Following mean streamlines, the tke does not show appreciable variation until the bottom wall is reached. This fact suggests that the very high dissipation rates in the upper right corner were keeping the tke magnitude low, and it is not until the bottom wall that tke production overcomes dissipation to produce notable tke values.

Kolmogorov lengthscale is another result in Figure 5.6. The results tell that, relative to the grid length, the Kolmogorov length scale ranges from one-tenth of the grid spacing in busy areas to 271 times the grid spacing near the inactive domain center. A significant aspect of this result is the fact that, near the top and right side walls of the domain, the smallest scales of the flow are less than the scales which are being resolved by this analysis. Although somewhat displeasing, this result is in line with other DNS simulations which report grid spacing which is greater than the Kolmogorov length in very limited parts of the domain.

Figure 5.7 shows time averaged coefficient of pressure in the domain, and the anisotropy ratio AR described in Section 3.1. Pressure coefficient shows typical trends; higher pressure arises to turn the flow away from walls and corners, whereas low pressures exist in the center of flow features which involve circulation. This pressure field is noteworthy in that it comes from equation 5.9 which does not rely on a speed of sound.

Anisotropy Ratio, shown in Figure 5.7, shows some trends not seen in simple flat plate turbulence. Anisotropy ratios greater than 1 indicate that the fluctuation in the x component of velocity is greater than than the fluctuation of the y component. As expected, near-wall anisotropy ratios show that the dominant component of fluctuating velocity is from the component parallel to the wall, since the other component is dampened by the impermeability of the wall. Anisotropy ratio profiles on

all non-driven walls show a reversal of the prevailing fluctuating velocity component in between the near-wall flow and the more calm flow in the domain center.

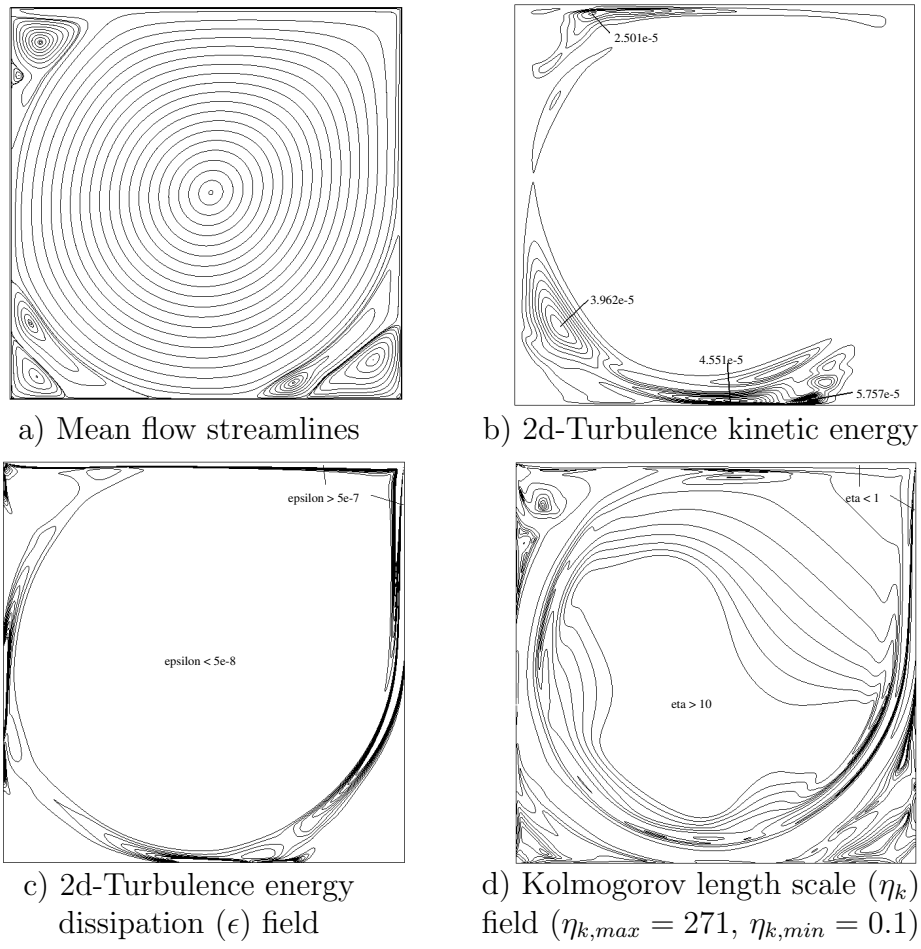

a) Mean flow streamlines

b) 2d-Turbulence kinetic energy

c) 2d-Turbulence energy dissipation (ϵ) field

d) Kolmogorov length scale (η_k) field ($\eta_{k,max} = 271$, $\eta_{k,min} = 0.1$)

Figure 5.6: Re 15,000 statistical property field contour plots

Statistical results for *Re* 20,000 are shown in Figure 5.8. Streamlines of the mean flow show various self-contained circulation zones in the domain corners consistent with other literature results. A configuration of mean flow circulation zones similar to that of *Re* 15,000 results develops. Conceptually, increased diffusion of flow quantities due to turbulence-like mixing is clear when considering the mean flow streamlines of

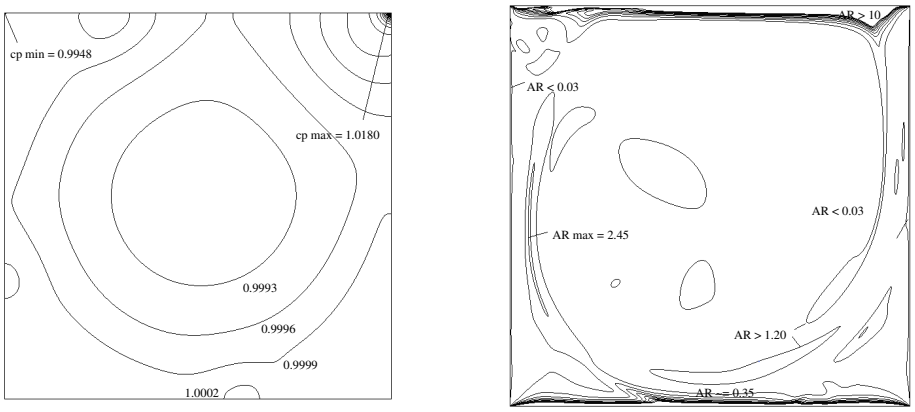

a) Pressure Coefficient b) Anisotropy Ratio

Figure 5.7: Statistical results for Re 15,000

these cases. For example, the mean flow streamlines show tangential, shearing flow at the boundaries between circulation zones. This description leaves out the fact that the real flow has transient eddy features which convect flow across the mean flow streamline boundaries and enhance mixing. Mean flow energy loss is another side effect of the turbulence-like chaos which is not indicated by Figures 5.6a and 5.8a. Because the chaos, like turbulence, has no net time-averaged effect it constitutes a lower or "less useful" form of energy in the flow.

Energy dissipation rate results of Figure 5.8c are similar to the Re 15,000 results, with high values on the driven wall and right hand wall. Also similar to the *Re* 15,000 results, the high dissipation tends to suppress overall tke until later in the flow, analogous to developing flow in a flat plate. The field of Kolmogorov length scale for *Re* 20,000 is qualitatively similar to that of *Re* 15,000. With the uniform grid spacing used, Kolmogorov length scales near the driven and right side wall are

one tenth of the resolved length scales. Near the center of the domain where the flow is less active, the smallest flow features are approximated as 235 times larger than the resolved scales. As noted previously, DNS simulations typically have a small part of the domain which is under- resolved. It is noteworthy that the largest Kolmogorov scale in this case is smaller than that of Re 15,000 - although Kolmogorov's theory says nothing of the largest scales. On the other hand, the fact that using $Re^{0.75}$ nodes in each direction leads the smallest computed η_k values in the two simulations to be the same agrees with Kolmogorov's theory that the smallest length scales are proportional to $Re^{-0.75}$.

Figure 5.9 presents results for the pressure coefficient and anisotropy ratio. Both of these fields have analogous behavior to their Re 15,000 counterparts, with variation in magnitudes. Flow-turning high pressure zones are present in near corners and wall centers, while low pressure zones exist at centers of mean flow circulation. With this Re we have the ability to make some direct qualitative comparison with literature [104]. In the work of Zhang *et al.*[104], the similarity of the pressure field features is very similar, including how the pressure changes away for the corners, the main contour band shapes radiating from the center of the domain, and even the appearance of contour bands on the bottom at approximately x=0.6, on the left at approximately y=0.3, and the top at approximately x=0.2. Variations do appear, but this is expected as the work of Zhang *et al.*[104] uses the weakly compressible LBE and a coarser grid. Interestingly, their work presents a "viscosity counteracting" modification to the MRT

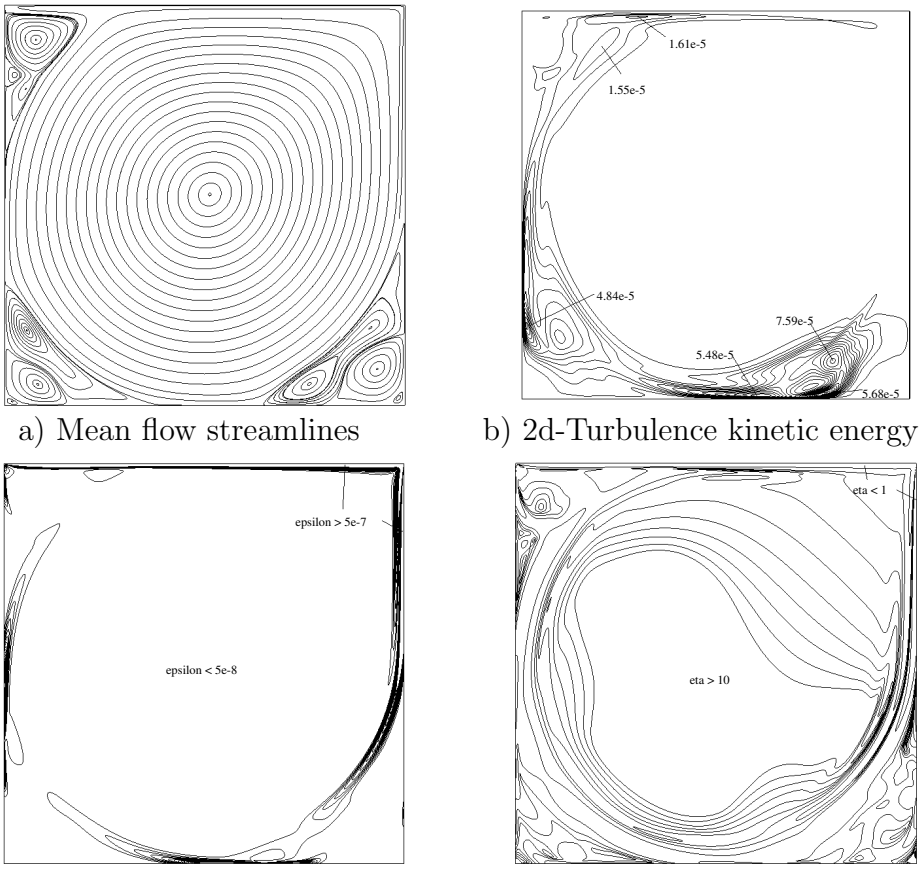

a) Mean flow streamlines

b) 2d-Turbulence kinetic energy

c) 2d-Turbulence energy dissipation (ϵ) field

d) Kolmogorov length scale (η_k) field ($\eta_{k,max} = 235$, $\eta_{k,min} = 0.1$)

Figure 5.8: Re 20,000 statistical property field contour plots

form which has unique value in such high-Re simulation, and is considered for future work.

An interesting feature of these flows is the anisotropy ratio on the non-driven walls for both cases. Whereas flat plate turbulent flow anisotropy maintains the order of highest- to-lowest as a function of distance from the wall, the LDC unstable results presented here do not. Consider the bottom wall of Re 20,000. AR at the wall is much greater than 1 because u_2 is damped due to the presence of the wall, and this

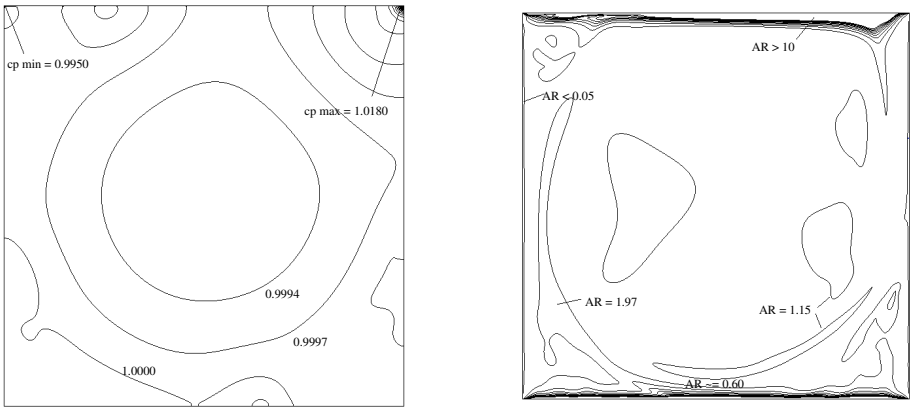

a) Pressure Coefficient b) Anisotropy Ratio

Figure 5.9: Statistical results for Re 20,000

is consistent with flat plate statistics. For the LDC, however, away from the wall AR reaches values as low as 0.6. In this location the RMS fluctuating velocity component perpendicular to the wall is larger than the corresponding wall-parallel component. This trend differs from flat plate flow results.

5.1.5 Conclusions

We have utilized the relatively new incompressible lattice Boltzmann equation with a multiple relaxation time collision operator as a direct numerical simulation tool. Steady laminar to chaotic flow transition has been documented with comparisons to literature and attention drawn to interesting phenomena such as the anisotropy ratio throughout the field. As a steady laminar solver, the method is well established, but it is also clear the simulation of macroscopic flows experiencing instabilities and

chaos is also well founded. The agreement of our method quantitatively at the first Hopf bifurcation with the majority of literature, and the qualitative agreement post-transition indicates that not only is the method valuable as a continuum flow solver, but also good resolution with a 2nd-order method may be more appropriate than a higher-order method with lower resolution. Future work interests include the viscosity counteracting modification to the MRT form for further high-Re benefits in the LBM.

5.2 3D LES of a Driven Cavity

Simulating a third dimension is a substantial challenge at higher Re due to the exponential cost of DNS. For example, performing the Re 20000 study of section 5.1 in 3D, with the same required resolution, would result in 4.75 billion nodes (66.5 billion degrees-of-freedom) with the lowest velocity 3D lattice. This is untenable with current computational power. To provide a workable solution, without resorting to a full modeling technique which would smear details, LES is implemented. To further provide generality, the Vreman sub-grid scale model is employed, which is designed to be valid through all regimes, steady laminar to fully turbulent [82].

Vreman's LES subgrid model is well studied for turbulent flows [82], so focus here is on validating this relatively new approach, in combination with the iLBE of this dissertation, in non-turbulent and intermittent transitional regimes. Per the landmark study by Vreman, the contribution of the SGS model should approach zero in non-turbulent regimes and yield the same results as incompressible solutions without models employed. The structure of Vreman's SGS should be valid for LBM, even the incompressible version, despite being originally applied to the N-S simulations.

To verify the iLBE with the Vreman SGS in transitory Re a series of simulations are performed and compared against the steady and unsteady data of literature utilizing

non-iLBE solvers. It is expected the SGS will play an appropriate role across the flow regimes, unlike the standard Smagorinsky-Lilly SGS, and predict a good match for Re_{Hopf}.

Due to the simplicity of geometry, yet complex flow physics, the lid driven cavity is again utilized. This also allows comparison to be made with the 2D DNS work of the previous section. The Re at which instability is generated will be predicted with the same methodology as section 5.1 and compared to the resources there.

5.2.1 Simulation Parameters

For direct comparison to the 2D configuration of the previous section (5.1), an open cube approximating a domain with width >> height is employed. As in the 2D cavity, the front, back, and bottom walls are all stationary no-slip, and the lid a no-slip wall translating in the positive x-direction. The third dimension introduced to this simulation is enforced with periodic bounds at $z = 0$ and Nz. The 2D study is then effectively the center plane of the current 3D cavity.

As in the 2D case the Reynolds number is defined as

$$Re = \frac{\boldsymbol{u}_{wall} L}{\nu} \tag{5.19}$$

where u_{wall} is the speed of the top wall, L is the width, height, and depth of the cavity, and ν is the viscosity. All properties and results are in LB and non-dimensionalized units; Re and non-dimensionalized units would be the same in a physical system. The second-order accurate half-way bounce-back scheme is utilized on all BCs, except the periodic bounds, which simply copy the missing lattice information from one z-coordinate extent to the other. A simulation characteristic time is defined as

$$t_c = \frac{L}{\boldsymbol{u}_{wall}}. \tag{5.20}$$

Since the motivation for an LES approach is to avoid extreme grid requirements, practical computational concerns and past literature guide the choice of node count. Further economy is achieved by utilizing the iLBE of chapter 4 with the D3Q15 approach, seen in figure 5.10. Similarly, the equilibrium distribution function, lattice weights, and pressure computation follow in equations 5.21 - 5.23, respectively.

$$f_a^{eq} = \begin{cases} 1 - \frac{7}{3}\frac{1}{c^2}P + S_a & \text{for} \quad a = 0 \\ \frac{1}{3}\frac{1}{c^2}P + S_a & \text{for} \quad a = 1 - 6 \\ \frac{1}{24}\frac{1}{c^2}P + S_a & \text{for} \quad a = 7 - 14 \end{cases} \tag{5.21}$$

where

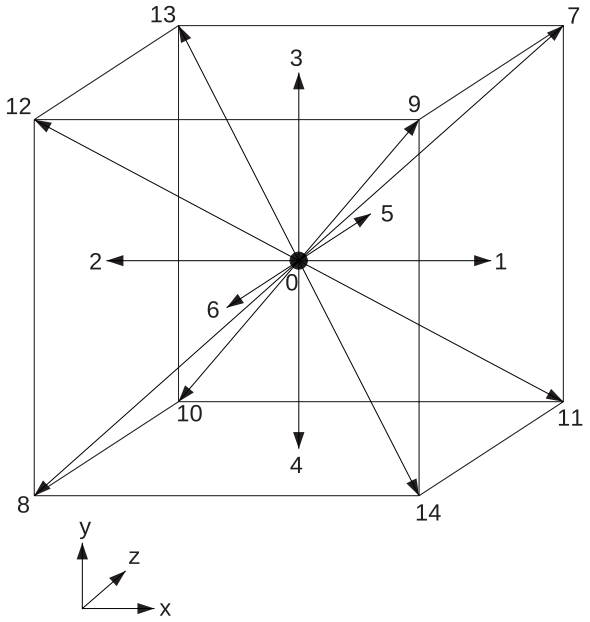

Figure 5.10: Lattice of D3Q15 LBE

$$S_a(\boldsymbol{u}) = w_a \left[3\frac{(\boldsymbol{e}_a \cdot \boldsymbol{u})}{c} + \frac{9}{2}\frac{(\boldsymbol{e}_a \cdot \boldsymbol{u})^2}{c^2} - \frac{3}{2}\frac{(\boldsymbol{u} \cdot \boldsymbol{u})}{c^2} \right], \tag{5.22}$$

$$w_a = \begin{cases} \frac{2}{9} & \text{for} \quad a = 0 \\ \frac{1}{9} & \text{for} \quad a = 1 - 6 \\ \frac{1}{72} & \text{for} \quad a = 7 - 14 \end{cases}$$

Based on the rest particle EDF of equation 5.21 the pressure is defined by

$$P = -\frac{c^2}{7}\left[\frac{1}{c^2}(\boldsymbol{u}\cdot\boldsymbol{u}) + 3f_0^{eq} - 3\right], \tag{5.23}$$

Additionally, because of the MRT approach, greater stability and reduced numerical dissipation are achieved than SRT [31, 71]. [105] does find that a D3Q18 version (D3Q19 without a rest particle) can provide some increased stability over the D3Q15 model, but with the expected cost increase of computing additional velocities per lattice node (and their contributions to macroscopic properties). Thus, for practical purposes, the 15 velocity model was selected of these two. However, motivation for higher velocity models (as high as D3Q27) exists based on comments found in [105, 106].

Simulations proceed from a zero-velocity initial condition and require a substantial burn-in time to reach the unchanging mean flow variables characteristic of turbulence. The burn-in time was surpassed before results were taken to ensure proper data collection, as measured by the achievement of time-independence of mean flow variables.

To ensure the low-Ma limit is obeyed, $\boldsymbol{u}_{wall}$ is held at a constant, which is always below 0.17. ν is altered to produce the correct Re. Due to the direct relationship between spatial resolution and Re in the LBM, ν can become very low without DNS level grid resolution. Even with the iMRT methodology, something additional must

enter the computation of ν locally to ensure stability. The next section describes the need for closure modeling, and the role of LES in physical modeling. In addition to a more accurate physical picture, a major benefit is stabilizing solutions which would otherwise diverge.

5.2.2 Vreman Sub-grid Scale Model

Noting the inability of the standard LES SGS model to handle laminar and transitional flows, and the complexity of existing models which resolve this issue (i.e. the dynamic Smagorinksy SGS model), Vreman derived a simpler approach [82]. The closure model is based on the Boussinesq assumption in which viscosity is modified by analysis of local conditions. The result is an effective viscosity ($\nu_e = \nu + \nu_{turb}$) employed in place of the molecular viscosity of the governing equations. In the context of the LBE, where the viscosity is represented by the collision relaxation time, this ν_e modifies the collision relaxation time operator.

In the Vreman model the effective viscosity is defined by

$$\nu_e = \nu + c\sqrt{\frac{B_\beta}{\alpha_{ij}\alpha_{ij}}}, \tag{5.24}$$

where c is related to the Smagorinsky SGS constant (C_s) by $c \approx 2.5C_s^2$. The remaining

variables are computed through

$$\alpha_{ij} = \partial_i \bar{u}_j \quad \text{and} \quad B_\beta = \beta_{11}\beta_{22} - \beta_{12}^2 + \beta_{11}\beta_{33} - \beta_{13}^2 + \beta_{22}\beta_{33} - \beta_{23}^2, \tag{5.25}$$

where $\beta_{ij} = \Delta_m^2 \alpha_{mi}\alpha_{mj}$ and Δ_m is the grid filter size in dimension m. Here, and in meshless LBM, this is going to be 1. The standard LBM relationship between the collision relaxation time (τ) and ν still holds, and provides the necessary modified momentum diffusion in the collision step.

Effective viscosity then requires only the determination of the first-order spatial derivative of velocity, similar to the standard SGS model. Importantly, turbulent viscosity is expected to approach zero in laminar and low-Re regions both in the far field and near walls, unlike the standard SGS model. Here the components of α are computed using second-order finite differencing: central differencing in the majority of the domain, and backward differencing at the boundary nodes.

As in the case of the standard SGS for LES, the value used for C_s is experimental and solver dependent. In the standard SGS this falls between 0.1-0.2, often 0.13-0.18. However, previous literature on the LES applied to the LBM indicates the value of C_s may be different than when applied to the N-S equations for similar simulations [32]. Here, 0.2 is used as this causes the largest reasonable eddy viscosity contribution to

effective viscosity. As a result, if the iLBE and Vreman SGS combination is not valid in non-turbulent regimes the solutions will highlight the issue.

5.2.3 Statistical Processing and Post Processing

Like RANS, where the statistical properties are computed as the run progresses and the numerics are modified, the SGS routine must be executed continuously. Unlike RANS, most scales are explicitly resolved and thus the full solution must be post-processed as in DNS. As such, special post-processing codes were required which took in mesoscopic and macroscopic data at the appropriate time steps. Instantaneous data must be produced at sufficient frequency to avoid aliasing to insure proper averaged properties after the burn in time.

Statistical values of velocity and pressure are computed as

$$\langle u_i \rangle = \frac{1}{N} \sum_{k}^{N} u_i^k \quad \text{and} \quad \langle P \rangle = \tfrac{1}{N} \textstyle\sum_k^N P^k. \tag{5.26}$$

u_i are the instantaneous velocity components, P is the pressure, N is the number of time steps, k is the time step, and the brackets $\langle\rangle$ indicate the average operator to compute the mean components.

5.2.4 Numerical Results

In all simulations the terms of the diagonal relaxation matrix found to be most stable, and thus utilized, are: $s_0 = s_3 = s_5 = s_7 = 1.0$, $s_1 = s_2 = 1.1$, $s_4 = s_6 = s_8 = 1.2$, $s_9 = s_{10} = s_{11} = s_{12} = s_{13} = \frac{1}{\tau_e}$, $s_{14} = 0.98$. Additional details of parameters necessary for, and utilized in this simulation can be found in appendix section A.2.2.

5.2.4.1 Verifying D3Q15 MRT-iLBE with Steady Flow

Laminar results of the MRT-iLBE with Vreman SGS applied to the LDC are compared with section 5.1 at *Re* 1000, which provides verification of the method to move to more complex simulation. Velocity along the center line on the z center plane is compared with the same values in the 2D DNS study (itself verified against considerable literature) for verification (see section 5.1). Comparison of velocity components and magnitude at the center point of the domain at *Re* 100, 400, and 1000 are also presented for verification. 3D plots are of interest to show that the flow structures extend in the "infinite" z-direction homogeneously, as well.

The analyses were run on a 101^3 grid, resulting in a node count of 1,030,301, and lattice degrees-of-freedom of 14,424,214. In addition, for each node a three-point second order finite difference equation in each coordinate direction is solved at every

time step. A total of 43,272,642 equations solved per time step.

For more direct comparison to the resolution of the 2D study: The grid on the plane for which data is collected is 101^2 (10,201), about six and a half times smaller than the 257^2 (66,049) grid of the 2D study. Yet when in direct comparison, table 5.4 and figure 5.11 show excellent agreement with the SGS model engaged. The resolution not only displays grid independence, when comparing against an 81^2 solution, but the Vreman SGS model behaves in accordance with its intent: Approaching zero in laminar flows. This is in contrast to the oversimplified Smagorinsky SGS model which would continue to modify the viscosity inappropriately at low-Re.

Table 5.4
MRT-iLBE for D3Q15 and D2Q9 Re 100, 400, and 1000 LDC.

Re	D3Q15 MRT-iLBE			D2Q9 MRT-iLBE		
	u_x	u_y	$\boldsymbol{u}$	u_x	u_y	$\boldsymbol{u}$
100	$-2.091\text{E}-1$	$5.744\text{E}-2$	$2.169\text{E}-1$	$-2.091\text{E}-2$	$5.754\text{E}-2$	$2.169\text{E}-2$
400	$-1.157\text{E}-1$	$5.206\text{E}-2$	$1.267\text{E}-1$	$-1.152\text{E}-2$	$5.206\text{E}-2$	$1.263\text{E}-2$
1000	$-6.255\text{E}-2$	$2.569\text{E}-2$	$6.762\text{E}-2$	$-6.215\text{E}-2$	$2.578\text{E}-2$	$6.728\text{E}-2$

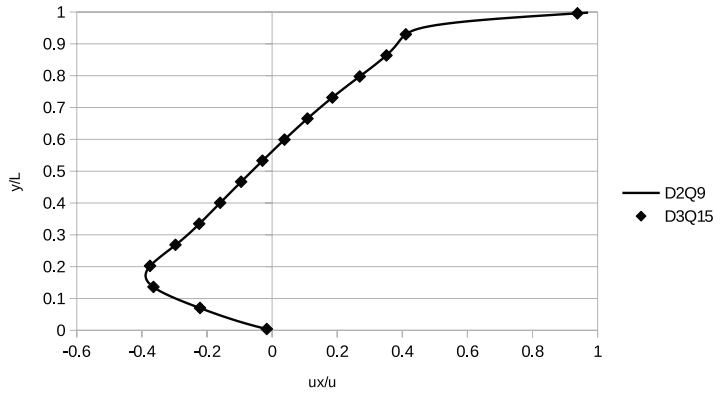

Figure 5.11: MRT-iLBE results between D2Q9 and D3Q15 at Re 1000.

Also important is the modification to the kinematic viscosity due to the SGS model in non-turbulent regimes. The traditional Smagorinsky SGS has been shown in literature to perform poorly in low-Re flows and in the near wall regions. In figure 5.12 it is clear that the viscosity contribution from the Vreman SGS here has almost no effect on the molecular viscosity of the simulated fluid, and what little effect there is, is minimized near walls, except for the high shear of the corners. The major vorticies are outlined in the τ_e map, however it is important to note again that the actual τ_{SGS} contribution is 0.16% at the extreme.

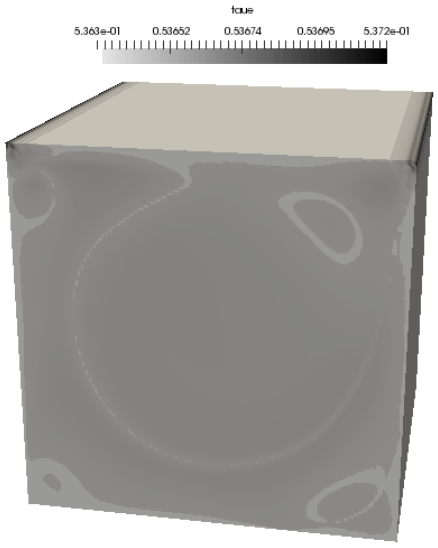

Figure 5.12: Variation of effective collision relaxation time τ_e ($\propto \nu_e$), from the Vreman SGS model at Re 1000.

5.2.4.2 The Hopf Bifurcation

To predict the onset of instability as a function of Re, the method of Cazemier *et al.* employed in section 5.1 is utilized again. This entails obtaining and plotting the square of the signal oscillation amplitude (A^2_{amp}) (the difference between velocity max and min values) as a function of Re. Regression analysis and extrapolation reveals the point at which $A^2_{amp} = 0$, indicating the regime change. For comparison to the 2D results, these values are gathered at the point (0.6, 0.6, 0.5).

The grid for each Re is 131^3, selected to benefit from the cost reduction of LES. Following the same calculations from the steady flow verification study, the total degrees-of-freedom per time step is 94,419,822. Combined with the time resolution requirement, this is an expensive approach. However, if the DNS approach of the 2D study were utilized, this number would jump to approximately 2.91E10. Over 300 times more expensive.

Figure 5.13 displays the oscillation present at the measurement point after the burn-in time. Sufficient sampling resolution was required to avoid aliasing the data and missing the peaks which determine amplitude. The differences are subtle as the input parameters are intentionally similar, but the upper and lower bounds of u_x change. This data was collected for Re 8200, 8300, and 8500. The decision to utilize these values was informed by the 2D study (for which the Hopf bifurcation occurred at Re

= 7988), and an initial run at Re 8000 which indicated the critical Re may be slightly higher here than in the DNS case. As in the DNS study, the Re values from which the final result is extracted must be both above and proximate to the instability onset.

In figure 5.14a the oscillations in both x- and y-velocities are represented in a phase space plot. The z-velocity for all simulations is machine zero, but would become of critical interest in a fully turbulent regime. As Re drops, both major and minor axes approach zero. It is also important to point out that each oval represents at least 10 characteristic times to display regularity in oscillation as opposed to an insufficient and unrepresentative sample size.

The square of the amplitude of x-velocity at each Re is then plotted to develop the line fit displayed in figure 5.14b. Basic extrapolation finds that instability sets in at Re 8081. Comparing to the 2D plane and DNS approach, this 3D LES approach runs **1.164 %** higher. This is a good match, and within the bounds of the existing literature, compared in table 5.5. The match is all the more impressive considering the substantially lower node count versus the "gold standard" of DNS.

To give a more complete picture of the LES results, figures 5.15a-d present information of interest on the center plane. Data is of the mean properties, computed after the burn-in time and over several hundred characteristic times. As a sample, Re 8300 is presented. The streamlines display the familiar LDC patterns: a centralized circulation region, secondary and tertiary eddies in the two bottom corners, and top

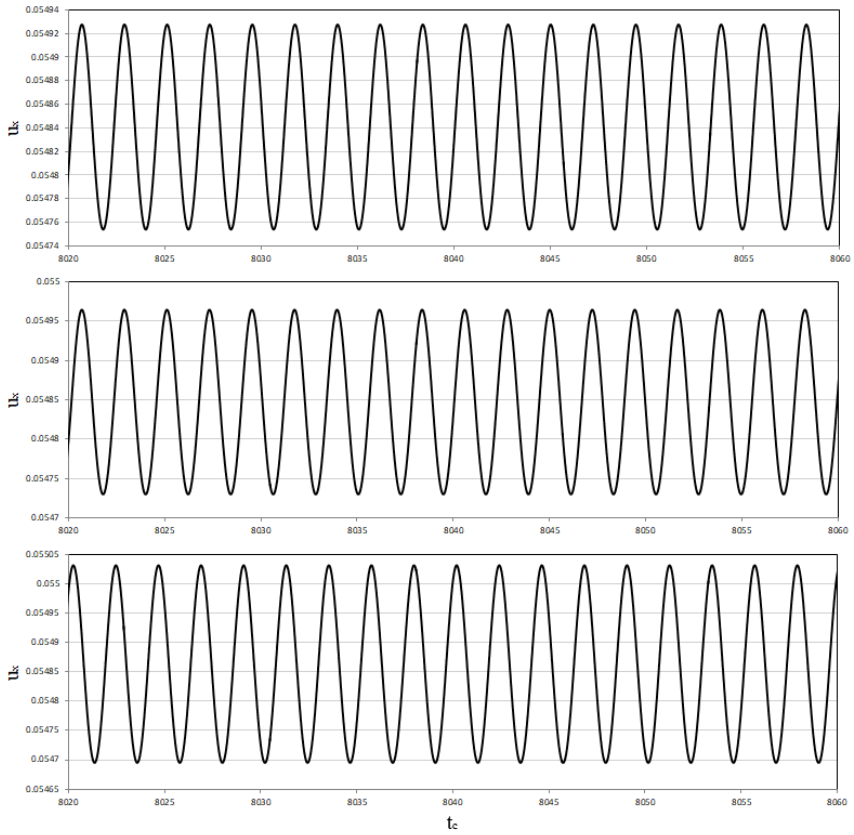

Figure 5.13: Oscillation of x-velocity at (0.6, 0.6, 0.5) after burn-in, at Re 8200, 8300, and 8500; top-to-bottom

left corner. Flow is generally well aligned on the top and right sides where there is a roughly singular, compelling, momentum direction. Pressure coefficients also follow the same pattern, with the center field close to the datum pressure due to the relatively low local velocity. Flow is accelerated in the top left corner, where the pressure is lowest. The top right and bottom left are where flow nearly comes to an abrupt halt.

Effective viscosity and shear strain rate fields are related, in that it is a close relative of shear (velocity gradient) which dictates the turbulent viscosity contribution. Thus it

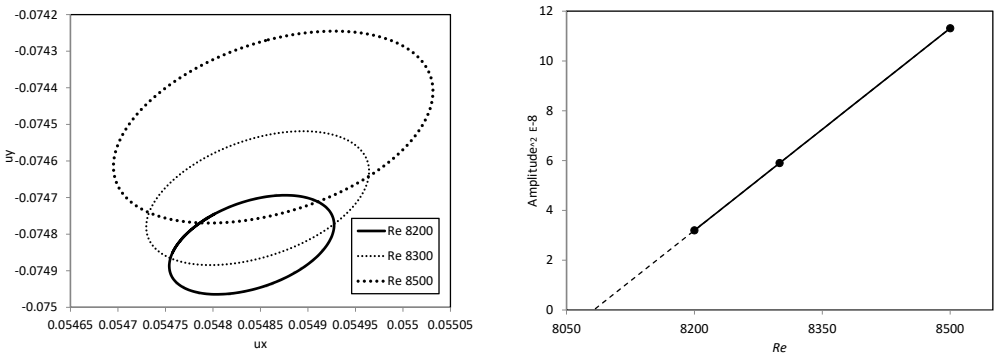

a) Phase space plots at (0.6, 0.6, 0.5)

b) Amplitude interpolation, predicting $Re_{Hopf} = 8081$

Figure 5.14: Hopf bifurcation determination

Table 5.5
Summary of literature Hopf bifurcation predictions for the lid driven cavity (2D except for current study)

Reference	Methodology	Re_{Hopf}
[80]	Oscillation amplitude interpolation to zero, N-S DNS	7972
[80]	POD model prediction by model constructed from Re 22k DNS results	7819
[78]	Interpolation to zero amplitude, 200x200 grid, 6^{th} order inner, 2^{nd} order bc's	7704
[79]	Direct dynamical system stability analysis	7763
[81]	Lyapunov Stabilty Analysis	8000 - 8,050
[3]	Interpolation to zero amplitude, MRT-iLBM DNS	7988 $\pm$ 19
This Study	Interpolation to zero amplitude, MRT-iLBM LES	8081 $\pm$ 19

isn't surprising that the peak shear of 40 occurring at the top right corner is where the peak viscosity occurs. Viscosity in the center represents the molecular viscosity fluid property; the baseline to which the modeled viscosity is added. In comparison, the top left corner with high shear is substantially higher. The Vreman model contributes a turbulent viscosity almost equal to the constant molecular viscosity. Combined with the high shear, this indicates that a potentially intermittent turbulence may be beginning.

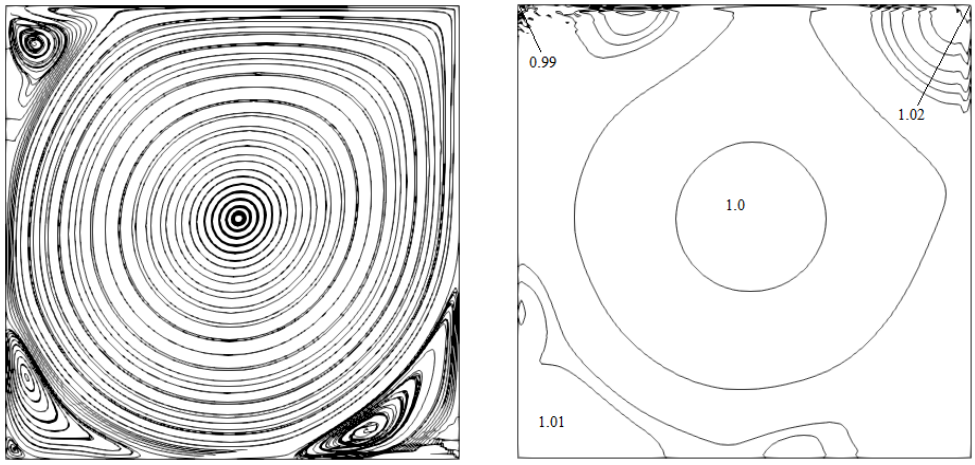

a) Mean flow streamlines b) Pressure coefficient

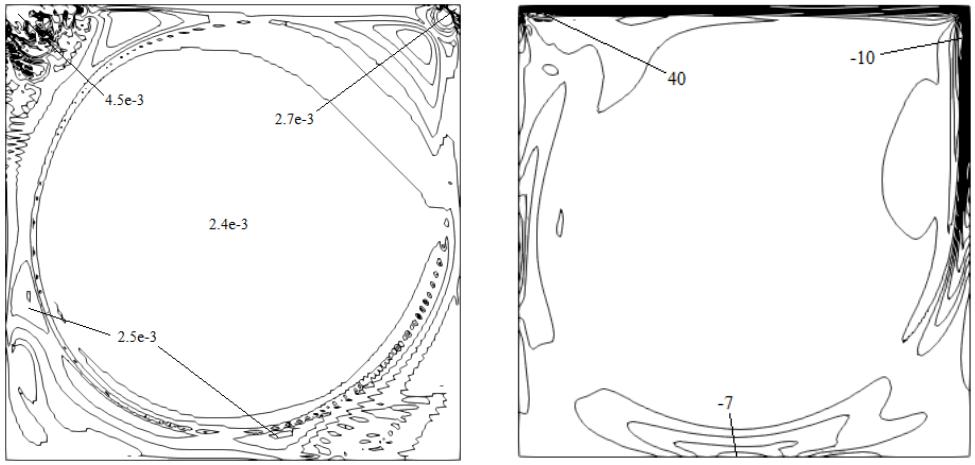

c) ν_{eff} field d) Shear strain rate field

Figure 5.15: Re 8300 field properties

5.2.5 Conclusions

Utilizing the incompressible LBE of this dissertation, the Vreman SGS model has proven to be a compatible and good pairing with the lattice Boltzmann method. In steady laminar flows of low Re, the contribution of turbulent viscosity approached zero, yielding solutions in good agreement with high resolution simulations free of

models. Comparing to the "gold standard" of the 2D DNS simulation previously conducted, the prediction of Re_{Hopf} was found to be in excellent agreement. For 3D flows, practically limited by computational power, the MRT-iLBE and Vreman SGS are thus recommended for flows of all Reynolds numbers. The combination realizes the low cost of the Vreman approach, relative to other transition-predictive SGS approaches, providing an attractive alternative to the Dynamic Smagorinsky and WALE SGS models for lattice Boltzmann, and CFD in general. Despite the low cost of a 15 velocity model, future work should focus on higher lattice velocity models.

Chapter 6

Substrate Generation and Verification[1]

Abstract

To provide porous media substrates that are quick to generate and characterize for lattice Boltzmann analysis, we propose a straightforward algorithm. The method leverages the benefits of the lattice Boltzmann method, and is extensible to multiphysics flows. Several parameters allow for simple customization. The generation algorithm and lattice Boltzmann method are reviewed, and suggested implementation

[1]The material contained in this chapter has been submitted to the *ASME Journal of Fluids Engineering* [4].

covered. Additionally, results are discussed and interpreted to evaluate the approach. Several verification tools are employed such as Darcys law, the Ergun equation, the Koponen correlation, a newly proposed correlation, and experimental data. Agreement and repeatability are found to be excellent, suggesting this relatively simple method is a good option for engineering studies.

6.1 Introduction

Disordered media flow analysis can provide significant design direction and research findings across a variety of fields such as oil and gas, chemical, automotive, and environmental engineering and sciences. However, the multiscale nature of porous flow presents challenges not present in many areas of computational fluid dynamics (CFD). Three length scales broadly describe most media: domain scale, representative elementary volume (REV), and pore scale. Domain scale provides the least detail and effectively acts as a black box. Behavior may be governed by simple pressure drop vs. flow rate assignments. The REV scale provides more details governed by semi-empirical correlations such as Darcy's law, the Kozeny-Carman relation, and the Klinkenberg, Forchheimer, and Brinkman considerations [107, 108].

It is at the pore scale where more fundamental governing equations can describe and display the flow for deeper understanding. Unlike the previous two descriptions, the

pore structures must be characterized, and put in a form for a discretized solution method. There are two main approaches: Acquisition of the solid matrix by an imaging device, such as X-ray computed tomography (CT scan), as used in [109] and construction of the solid matrix by an algorithm that follows certain properties [54, 110–113]. The focus here is on a simpler, but still effective algorithm construction to provide greater flexibility, speed, and variety than a scanning process can.

Not all mathematical techniques for resolving flow fields are ideal for pore scale flows. The choice of technique depends on important considerations like handling of complex boundary conditions and the ease with which the scheme can be parallelized [49]. The lattice Boltzmann method (LBM) utilizes the relatively simple bounce-back scheme on arbitrarily complex solid surfaces and momentum inlets [24, 36], is relatively easy to implement [49], and due to its linear nature, scales well when parallelized [114]. The lattice Boltzmann equation (LBE), however, introduces a compressibility error for incompressible flows [20], such as most filter flows [64]. In order to reduce this error, an incompressible method (marked with an i) is utilized here [1].

In this study, a simpler algorithm for filter substrate generation for lattice Boltzmann analysis is proposed. A filter substrate refers to the underlying material which provides the pore structure, commonly cordierite for diesel particulate filtration. The generated substrates are compared against semi-empirical models with an incompressible lattice Boltzmann equation to verify the algorithm. Flows and conditions

are representative of common filter conditions, such as $Re < 100$. Capability of the generated substrate to handle thermal and multiphase flows and sweeps of various porosities is discussed. Modifications for various types of porous media and three dimensional flows are also considered for future work.

6.2 Substrate Generation and Measurement Algorithm and Pseudocode

Defining the simulation domain is fundamentally a task of marking nodes of a lattice as solid or fluid on an Nx x Ny state matrix. This state matrix must provide the ability to control porosity, and ideally the ability to control a characteristic size. It must also be possible to make the necessary measurements such as porosity, wetted perimeter, and flow area to obtain characteristics like hydraulic radius and Reynolds number (Re).

To comply with the variety of languages for LBM code implementation, a pseudocode is presented in appendix D with broad applicability. The code provides functions not only for the substrate generation, but also for measurement, and to flag boundary nodes. By flagging boundary nodes during preprocessing, LBE streaming and bounce back occurs only on the necessary nodes, introducing an efficiency improvement.

Generation is based on the random placement of ellipses that can overlap to form more complex shapes. Each ellipse has a major and minor axis of random radii within a designated range of values. Nodes that fall within the ellipse are flagged as "solid" in the state matrix. Only certain portions of the lattice are allowed to contain solids to provide inlet and outlet areas, both of which can be dictated. To ensure these areas are obeyed, the portions of ellipses that were assigned to the inlet and outlet areas are reset to "fluid". The size of the domain, number of ellipses, and radii ranges are important choices, and will be discussed further in the verification and results section.

This compact method produces substrates with porosity within 1% of that assigned, once calibrated. Shape of the solid substrate is more complex than if circles or squares formed the fundamental substrate. Since an ellipse can easily be described by an equation with a third dimension, the generation method can be readily extended. An extension to 3D would provide a percolation threshold below 0.4, as opposed to this initial study on two-dimension, which limits the porosity to values greater than 0.4 to avoid the zero permeability limit.

Boundaries are marked with a search algorithm, and the link(s) of the lattice between fluid and solid nodes are recorded. As a result, operations in the LBM are performed only where necessary. Since the perimeter computation is done in the initialization stage, it is not repeated during simulation.

Finally, measurement is conducted based on inputs from the previous functions. The

discrete nature of the lattice makes characterization fundamentally a counting task. By providing porosity and wetted perimeter, the non-dimensional values that verify and characterize the filter can be computed. These equations and implementations are discussed in the sections on methodology and results.

Fig. 6.1 and Fig. 6.2 demonstrate samples of the generated substrates.

Figure 6.1: Sample generated substrate geometry: 50% porosity.

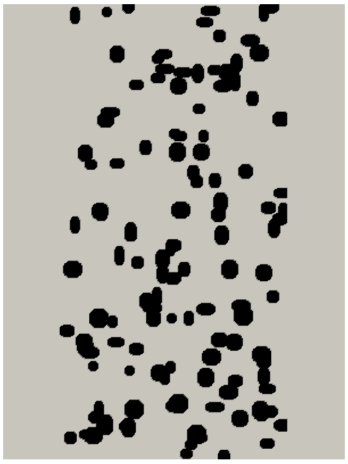

Figure 6.2: Sample generated substrate geometry: 80% porosity.

6.3 The Lattice Boltzmann Method

By solving the Boltzmann equation for streaming and colliding particles, fluid flow can be resolved in a more fundamental manner than the Navier-Stokes equations. Discretization results in the lattice Boltzmann equation, and allows for a computational approach to fluid dynamics.

6.3.1 The Incompressible Lattice Boltzmann Equation

The LBE is stated as [115]

$$f_i\left(\boldsymbol{x}+\boldsymbol{c}_i, t+\delta_t\right)=f_i\left(\boldsymbol{x}, t\right)-\frac{1}{\tau}\left[f_i\left(\boldsymbol{x}, t\right)-f_i^{eq}\left(\boldsymbol{x}, t\right)\right], \tag{6.1}$$

where δ_t is the time step, f is the velocity distribution function, $c = \delta_x/\delta_t$ is the lattice speed, δ_x is the spatial discretization, i is the index of the lattice velocity, τ is the collision relaxation time related to viscosity, and f^{eq} is the equilibrium distribution function based on the Maxwell-Boltzmann distribution.

The form of the equilibrium distribution function largely dictates the characteristics of the flow solution. The standard form is [115]

$$f_i^{eq} = w_i \rho \left[1 + \frac{\boldsymbol{c}_i \cdot \boldsymbol{u}}{c_s^2} + \frac{(\boldsymbol{c}_i \cdot \boldsymbol{u})^2}{2c_s^4} - \frac{\boldsymbol{u}^2}{2c_s^2} \right], \tag{6.2}$$

where w_i is the velocity weight, ρ is density, and c_s is the speed of sound. Macroscopic density and momentum are computed by

$$\rho = \sum_i f_i, \quad \rho \boldsymbol{u} = \sum_i \boldsymbol{c}_i f_i. \tag{6.3}$$

At small Mach numbers and density variations, the error in simulating incompressible flows is limited. For porous flows, this can pose a problem due to large pressure and density gradients [64].

Past filtration studies have utilized an LBE which limits the compressibility error [43] with a pseudo-compressibility approach. However, improvement in achieving an

incompressible behavior for steady and transient flows can still be made [1]. The incompressible singular equilibrium form is

$$f_i^{eq} = \begin{cases} 1 - 5P/3c^2 + S_i(\boldsymbol{u}), & i = 0 \\ P/3c^2 + S_i(\boldsymbol{u}), & i = 1, 2, 3, 4 \\ P/12c^2 + S_i(\boldsymbol{u}), & i = 5, 6, 7, 8 \end{cases} \tag{6.4}$$

with

$$S_i(\boldsymbol{u}) = w_i \left[3\frac{(\boldsymbol{c}_i \cdot \boldsymbol{u})}{c} + \frac{9}{2}\frac{(\boldsymbol{c}_i \cdot \boldsymbol{u})^2}{c^2} - \frac{3}{2}\frac{(\boldsymbol{u} \cdot \boldsymbol{u})}{c^2} \right], \tag{6.5}$$

where P is pressure. Density is no longer a variable, and a speed of sound is no longer present. The macroscopic variables are computed as

$$\boldsymbol{u} = \sum_i \boldsymbol{c}_i f_i, \quad P = \frac{3c^2}{5}\left[1 - f_0^{eq} + S_0(\boldsymbol{u})\right] \tag{6.6}$$

Through the Chapman-Enskog expansion the incompressible Navier-Stokes equations are recovered as

$$\nabla \cdot \boldsymbol{u} = 0, \tag{6.7}$$

$$\frac{\partial \boldsymbol{u}}{\partial t} + \nabla \cdot (\boldsymbol{u}\boldsymbol{u}) = -\frac{1}{\rho_0}\nabla P + \nu \nabla^2 \boldsymbol{u}. \tag{6.8}$$

where viscosity and the collision relaxation time are related by

$$\nu = \frac{\delta_x^2}{3\delta_t}\left(\tau - \frac{1}{2}\right) \tag{6.9}$$

When the LBM has been applied to pore scale simulations, convergence and accuracy were found to be compromised due to artifacts in the boundary conditions. Pan *et al*. recognized this issue and found that a multiple relaxation time (MRT) form of the LBE avoided the problem [56]. More specifically, viscosity in the single relaxation time (SRT) form has an effect on where the boundaries are located [24]. While the permeability should scale linearly with viscosity (all other quantities being equal), Pan *et al.* finds unwanted deviations using SRT, in particular at low viscosities. Implementing the SRT form in our own models results in the same trend.

The MRT-LBE replaces the single value τ with a collision matrix which allows each mode to relax at a different rate. Due to these benefits, the flow solver for this study

is the MRT-iLBE. d'Humieres introduces the MRT-LBE, and Murdock *et al*. provide derivations, forms, and results of using the MRT-iLBE, which is second-order accurate in time and space [3, 70, 106].

6.3.2 The Lattice

As previous sections have discussed, the substrate matrix is formed on, and the solution takes place on a lattice of nodes. For this study, that lattice is D2Q9, where D labels the number of spatial dimensions, and Q labels the number of discrete velocities. Fig. 6.3 shows the lattice structure used here.

Values discussed in the section on the LBE, such as w, c, and the subscript i all made reference to properties of this lattice. For D2Q9, w_i = 4/9, 1/9, 1/9, 1/9, 1/9, 1/36, 1/36, 1/36, 1/36 for i =0-8. Since this is a square lattice, c=1 and c_i =(0,0),(1,0),(0,1),(-1,0),(0,-1),(1,1),(-1,1),(-1,-1),(1,-1) for i=0-8. In the standard LBE case, $c_s^2 = 1/3$.

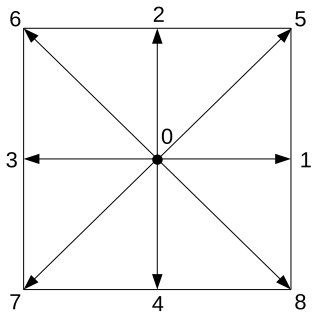

Figure 6.3: D2Q9 lattice structure.

6.3.3 Boundary Conditions

For porous media flows, the major benefit of the LBM is boundary condition implementation. The bounce-back method is commonly implemented in LBM for complex geometries. The algorithm is simple. As shown in Fig. 6.3, if a value for f_8 streams into a wall, it is simply returned along the lattice vector 6. Even without the perimeter and link search of the algorithm presented in the previous section, the boundary conditions is easy to implement and efficient just by knowing which lattice nodes are solid and which are fluid.

Boundaries conform to the Cartesian grid, and form a stair-step approximation to the pore structures. While this is an approximation to potentially more complex surfaces, it allows for implementation ease and computational efficiency, and is frequently applied to LBM filter simulations with success [43, 64]. Implementing this approach for common filter flow conditions, we find good agreement with verification techniques in the latter sections of this work. Accuracy of these complex boundaries is improved with increasing global grid refinement. This can be expensive; however, the need to refine the entire domain to capture the random distribution of small pore passages partially negates the benefits of a local refinement approach. This simple method is applied on all substrate surfaces in the domain.

The same boundary method can be modified for symmetry and inlet boundary conditions. To provide the free-slip behavior of symmetry bounds, the value of f_8 is specularly reflected along the lattice vector 5. For the top and bottom boundaries of the substrate domain, this method is implemented to simulate the length of an entire filter wall. At the inlet, the value of f_i bounced back into the domain is modified with a momentum source term to generate the desired velocity [36]. The boundary (wall, symmetry, or inlet) is actually placed at the point halfway between solid and fluid node, and this is accounted for in our algorithm. With this halfway interpolation, the boundaries are second-order accurate [24, 106].

Outlets are the only boundary which cannot utilize a bounce-back scheme. Instead an extrapolation scheme [69], similar to the finite difference method, is implemented, which is second-order accurate.

6.3.4 Multiphysics Capability

Since transport phenomena are described by equations fundamentally similar to the Navier-Stokes equations, the lattice Boltzmann equation described in the previous sections can be readily extended to additional physics [116]. Further, since the substrate is generated to be complaint with the LBM, these additional transport LBEs can be employed. Non-isothermal incompressible flow is straightforward to implement,

and since velocity can simply be turned to zero at solids, conjugate heat transfer on the substrate is not difficult to implement [117]. While viscosity is replaced by thermal diffusivity for energy transport, the same equation can be employed with mass diffusivity to transport the species to be filtered [118].

6.4 Verification Methodology

The following empirical and derived equations and correlations provide the basis for utilizing the algorithm presented in a previous section for filter studies.

6.4.1 Darcy's Law

Darcy's law is a widely employed model relating the porosity (ϕ) and the ease with which flow passes through disordered media, measured by permeability (κ). For a fluid of viscosity ν, density ρ, and velocity $\boldsymbol{u}$, the pressure drop should result in a permeability given by [108]. Pressure drop in eqn. 6.10 is calculated using the average value of pressure at the inlet and outlet, respectively.

$$\kappa = \frac{\boldsymbol{u}\nu\rho}{\nabla P} \tag{6.10}$$

Since the pore scale flow is being resolved, permeability is a direct result of the simulation algorithm, as opposed to an input or tuned result. Further, with the use of the MRT form, permeability behaved linearly with viscosity changes in our models. The relationship between porosity and permeability is linear on a semi-log plot. Simple calculation and expectations make this a good initial methodology for verification of pore scale simulations.

6.4.2 Ergun Equation

The Ergun equation relates pressure losses in the form of the friction factor (f) to the Reynolds number of a packed column and fluidized beds. The equation is a correlation without the foundation of the Navier-Stokes equations like Darcy's law. However, it is a useful tool in determining the validity of methods for analyzing fluid flows in porous media. The equation is stated here as [85]

$$f = \frac{150}{Re} + 1.75 \tag{6.11}$$

where Re is defined as

$$Re = \frac{\boldsymbol{u} D_p}{\nu\,(1-\phi)} \tag{6.12}$$

For three dimensions, the hydraulic diameter is defined as

$$D_p = 6R_h \frac{(1-\phi)}{\phi} \tag{6.13}$$

where the hydraulic radius R_h is the ratio of flow volume to wetted surface area.

Since two dimensions are of interest in this initial study, the definition of Dp must be modified. Since the radius is determined by the ratio of volume to surface area in three dimensions, it is possible to "remove" one dimension from each measure in two dimensions, yielding the ratio of flow area to wetted perimeter. This ratio reduces to $D_{sphere}/6$ in three dimensions and $D_{circle}/4$ in two dimensions. As a result, the two dimensional hydraulic diameter is defined as

$$D_p = 4R_h \frac{(1-\phi)}{\phi} \tag{6.14}$$

Friction factor from the simulation is computed as

$$f = \nabla P \frac{D_p \phi^3}{\boldsymbol{u}\,(1-\phi)} \tag{6.15}$$

and compared with equation 6.11. On a log-log plot the Ergun equation forms a more complex non-linear shape, providing a more challenging verification test.

6.4.3 Koponen Model

A simple exponential model is fitted to the porosity-permeability data as proposed by Koponen *et al*. for creeping flow through large three dimensional random fiber webs [119]. However, there is no theoretical basis for this model in literature as also stated in [119]. This model is valid for values of porosity between 0.42 and 0.85. The model has an essential shortcoming. The zero permeability limit is not reached at a finite porosity value, called the percolation threshold, ϕ_c. Despite these shortcomings, the model provides a good verification test for our random substrate generator, the model being valid over a wide range of porosities and also having shown good agreement with experimental data [120]. The relation for the model expressed in non-dimensional form is,

$$\frac{\kappa}{D_p^2} = \frac{\alpha}{exp\left(\beta\left(1-\phi\right)\right) - 1} \tag{6.16}$$

The following values are found for constants α and β in equation 6.16,

$$\alpha = 2.44, \quad \beta = 13.94 \tag{6.17}$$

6.4.4 A New Semi-Empirical Model

A number of correlations have been proposed since the late 1940s trying to relate porosity and permeability in porous media. Broadly, these correlations can be classified into three types:

1. Relations based on the flow through conduits model.
2. Relations based on the flow past a submerged body model.
3. Relations based on the Cell Model theory.

At low and intermediate porosities, the porous flow is modeled better by the flow through conduits approach while at higher values of porosity the flow past a submerged body model or the cell model theory gives better results [121]. The model usually used for flow through filters, called the Kubawara model [17], is based on the cell model theory. Hence, it slightly over-estimates the permeability values at low porosities, as it does not take into account the effect due to surrounding fibers in the

porous structure. A model based on the conduit-flow approach would give a better approximation at low and intermediate porosity values. Though at higher values of porosity, the Kubawara model gives very good results [122]. Apart from this, the Kubawara model does not take into account the percolation threshold (the minimum porosity of the medium above which it becomes permeable). The idea to improve the permeability model is based on using a weighted combination of two models, a conduit-based model for low porosity values and a submerged body model or a cell model for higher porosities.

6.4.4.1 The Conduit-Model: Gebart Model

Gebart's formulation is based on modeling the porous structure as a parallel array of cylinders perpendicular to the flow direction and modeling the flow through the voids as flow through conduits of very small cross-section or diameter [123]. If Gebart's derivation is followed for cylinders with elliptical cross-sections (the shape of the solid substrate used in the substrate generator being an ellipse) instead of circles in hexagonal arrangement, the following result is reached,

$$\kappa = \frac{4}{9\pi\sqrt{6}} \left[\frac{1-\phi_c}{1-\phi} - 1 \right]^{\frac{5}{2}} \left(\frac{a^{\frac{3}{2}} b^3}{(a+b)^{\frac{5}{2}}} \right) \tag{6.18}$$

where a and b are the semi-major and the semi-minor axis of the ellipses respectively. The second term on the right hand side in the above equation in brackets () is simply a length scale squared. This can be replaced by a characteristic length scale, D_p^2 (chosen to be the hydraulic diameter as defined in equation 6.14) and the above equation can be written in non-dimensional form as follows,

$$\kappa = \frac{4}{9\pi\sqrt{6}} \left[\frac{1-\phi_c}{1-\phi} - 1 \right]^{\frac{5}{2}} \tag{6.19}$$

6.4.4.2 Flow Past a Submerged Body Model and the Cell Model

The model chosen for modeling permeability at higher porosities is the Brinkmann model [124]. This model is based on flow past a swarm of spherical particles. The resulting equation for permeability based on this model in non-dimensional form is,

$$\frac{\kappa}{D_p^2} = \frac{1}{72} \left[3 + \frac{4}{1-\phi} - 3\sqrt{\frac{8}{1-\phi}} - 3 \right] \tag{6.20}$$

The Kubawara model, based on the cell model theory [122], can also be used in place of the Brinkmann model for intermediate and higher porosities and gives exactly the same results. The Kubawara model also improves the range of validity, as the Brinkmann model is not valid for porosities lower than 0.33 [121]. The relation for

the Kubawara model in non-dimensional form is given by,

$$\frac{\kappa}{D_p^2} = \frac{2}{9}\left(\frac{2 - \frac{9}{5}(1-\phi)^{\frac{1}{3}} - \phi - (1-\phi)^2}{1-\phi}\right) \tag{6.21}$$

6.4.4.3 Tortuosity Factor

The models mentioned above, like most permeability models suffer from the drawback of not including the effects of the twisted flow path through the porous structure, quantified by the tortuosity of the porous structure, T. In the present model, an empirical relation for tortuosity is used to incorporate its effect. The following correlation is used to model tortuosity as used by Carman [121],

$$T = \left(\frac{L_e}{L}\right)^2 \tag{6.22}$$

where L is the length of the porous structure in the macroscopic flow direction and the value of L_e depends on the type of porous media under consideration. The value of L for the present simulation is 200 units.

6.4.4.4 Blending functions/Basis-functions

The two models are finally blended together using the idea of blending functions or basis-functions. The particular choice of the basis set allows the Gebart form to be the major contributor to the relation at low porosities and the Brinkmann model or the Kubawara model to take over at high porosities > 0.75. The basis set chosen is as follows,

$$w_1(\phi) = a_1 + a_2 e^{a_3(1-\phi)} \tag{6.23}$$

$$w_2(\phi) = b_1 + b_2 e^{b_3\phi} \tag{6.24}$$

The blending function constants a_1, a_2, a_3, b_1, b_2, and b_3 are found using the values of the blending functions, $w_1(\phi)$ and $w_2(\phi)$ at the three nodal values that include the end nodes $\phi = \phi_c$ (the percolation threshold) and $\phi = 0.9$ (the last value of ϕ in our numerical simulation results) and a mid-node chosen to be $\phi = 0.75$. The values of the blending functions at the nodes are, $w_1(\phi_c) = 1$, $w_1(0.9) = 0$, $w_2(\phi_c) = 0$, $w_2(0.9) = 1$ and $w_1(0.75) = w_2(0.75) = 0.4$. The blending functions, $w_1(\phi)$ and $w_2(\phi)$ with $\phi_c = 0.135$ are plotted against porosity in Fig. 6.4.

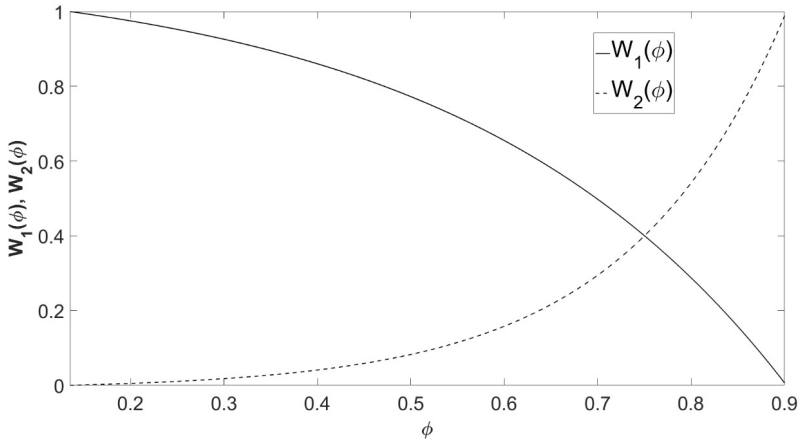

Figure 6.4: Blending functions w_1 and w_2 vs. porosity.

6.4.4.5 The Model Equations

The new model is based on the idea of modeling the permeability at low porosities using the conduit flow approach and the permeability at high porosities using the flow past a submerged body or the cell-model approach. The combined model is based on a more flexible form of the Gebart relation given by Nabovati *et al.* [84], and the Brikmann relation or the Kubawara relation. The following non-dimensional model equations are arrived at based on above discussions for the Brinkmann and Kubawara models respectively. Both equations are divided by the tortuosity factor, T. The relation for the combined Gebart-Brinkmann (GB) model is,

$$\begin{aligned}\frac{\kappa}{D_p^2} =& \frac{1}{(\alpha/L)^2} w_1(\phi) \frac{4}{9\pi\sqrt{6}} \left[\frac{1-\phi_c}{1-\phi} - 1\right]^{\gamma} \\ &+ \frac{1}{(\beta/L)^2} w_2(\phi) \frac{1}{72} \left[3 + \frac{4}{1-\phi} - 3\sqrt{\frac{8}{1-\phi} - 3}\right]\end{aligned} \tag{6.25}$$

and for the combined Gebart-Kubawara (GK) model is,

$$\begin{aligned}\frac{\kappa}{D_p^2} =& \frac{1}{(\alpha/L)^2} w_1(\phi) \frac{4}{9\pi\sqrt{6}} \left[\frac{1-\phi_c}{1-\phi} - 1\right]^{\gamma} \\ &+ \frac{1}{(\beta/L)^2} w_2(\phi) \frac{2}{9} \left(\frac{2 - \frac{9}{5}(1-\phi)^{\frac{1}{3}} - \phi - (1-\phi)^2}{1-\phi}\right)\end{aligned} \tag{6.26}$$

where $w_1(\phi)$ and $w_2(\phi)$ are given above. Gebart derives the value of the percolation threshold in the above equations for a hexagonal arrangement of circles [123]. A more exact value of $\phi_c = 0.135$ is chosen from a numerical simulation of random arrangement of ellipses as shown in [125]. The values of the blending function constants for the GK model with $\phi_c = 0.135$ and specific nodal conditions are $a_1 = 1.12$, $a_2 = -1.49$, $a_3 = -2.91$, $b_1 = -0.01$, $b_2 = 0.005$ and $b_3 = 5.93$ respectively. As for the Gebart-Brinkmann model, the value of $\phi_c = 0.33$ is used, this being the lower limit in the range of validity of the Brinkmann model. The values of the blending function constants for the GB model with $\phi_c = 0.33$ are found to be $a_1 = 1.38$, $a_2 = -1.72$, $a_3 = -2.25$, $b_1 = -0.04$, $b_2 = 0.0064$ and $b_3 = 5.65$ respectively. A curve of the form is then fit to the data generated from the iLBM simulation using the non-linear least-squares method. The following values are found for constants α, β, and γ.

$$\alpha = 140.90, \quad \beta = 106.18, \quad \gamma = 2.17 \tag{6.27}$$

$$\alpha = 133.71, \quad \beta = 171.51, \quad \gamma = 3.84 \tag{6.28}$$

The values found for γ are around the same range as found by Nabovati [84] and Gebart [123].

6.5 Results

For each study point, a new filter is generated to demonstrate repeatability. Unless otherwise marked, units are non-dimensional lattice Boltzmann units. Inlet velocities are varied between 0.001 and 0.1 depending on porosity, for low Mach numbers, and outlet pressures are 1.0. All values are initialized to 0 and the solution proceeds until convergence is achieved at an RMS velocity change of 10^{-9}. In all cases, $\tau = 1.0$, so Re is computed and reported.

A number of grid sensitivity tests indicate that porosities greater than about 0.8 can utilize a grid of only 300 x 401 nodes, while lower porosities require a grid of 300 x 601 to ensure effective flow passages. 50 nodes upstream and downstream of the filter section bring the boundary conditions sufficiently far from the high gradients of the complex filter flow, leaving a 200 node-wide effective filter wall. The domain can be visualized as shown in figure 6.5. While both the number and radii of ellipses can

be used to control porosity, the number of ellipses is modified and radii ranges are assigned as 5-10 nodes here. This forms substrates more in line with cordierite, but other disordered media may be better matched by adjusting the allowed radii.

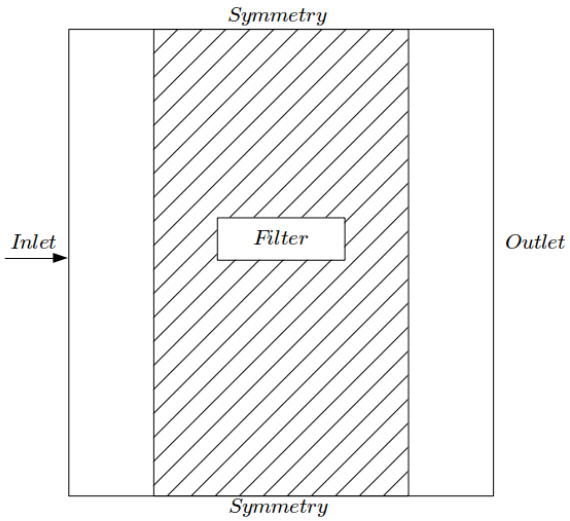

Figure 6.5: Computational fitler domain and boundaries.

Velocity fields of the sample filter substrates in figure 6.1 and figure 6.2 are visualized in figure 6.6 and figure 6.7, respectively. Velocities are normalized by the inlet value. The apparent rivulets are the flow paths through the substrate, with darker colors representing higher velocities, and the lighter colors signifying low velocity (the zero velocity of the substrate solids is the lightest). Visually, the flow paths are sensible, and the greatest mass flow occurs where resistance is lowest.

Figure 6.6: Velocity field at 50% porosity (*Re* 2.6).

6.5.1 Verification by Darcy's Law

In figure 6.8 permeability is plotted as a function of porosity for five filters at different porosities, at three different velocities. The goal is to evaluate if permeability of the generated filter is intrinsic, and if the relationship is linear on a semi-log plot.

In all cases, it is shown that permeability is independent of the specific filter and velocity. Permeability is only a function of porosity, within numerical error.

Figure 6.7: Velocity field at 80% porosity (Re 49).

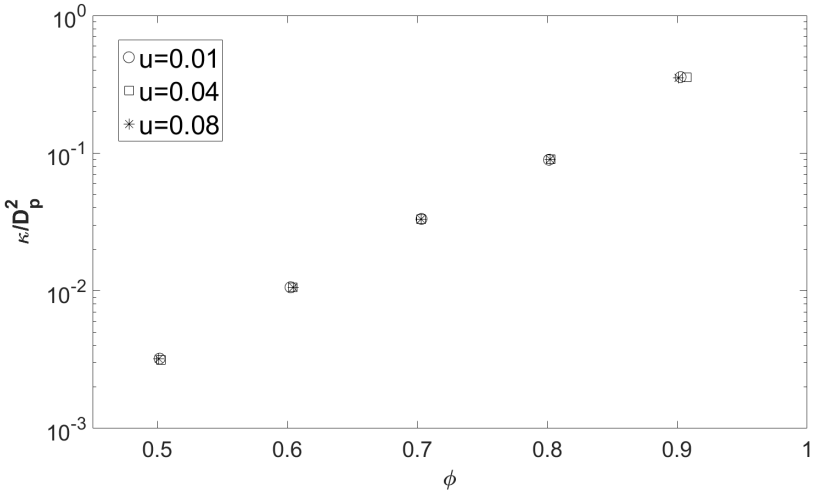

Figure 6.8: Porosity vs. permeability at multiple velocities.

6.5.2 Verification by Ergun Equation

For five filters of porosities 0.5, 0.6, 0.7, 0.8, and 0.9 a variety of inlet velocities were applied to vary Re. Friction factor at each Re was computed and plotted on a log-log

scale in figure 6.9. The Ergun equation is plotted with the data as a solid line.

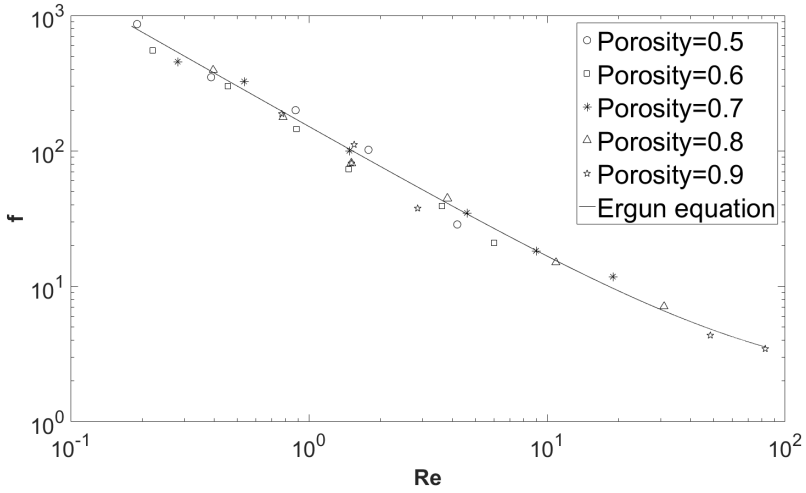

Figure 6.9: *Re* vs. friction factor at multiple velocities and porosities, compared to Ergun equation.

The results provide a good match to the correlation. Since visual comparison to the empirical correlation is important in this case, it is worth considering the results of other studies. When set beside figure 6.4-2 of Bird's *Transport Phenomena* [85], the filter substrate generated by the algorithm of this study, and analyzed by the MRT-iLBE, is at least as good a match as experimental results from previous works.

6.5.3 Verification by Porosity-Permeability Correlations

Permeability is evaluated at different values of porosity generated using the random substrate generator. The values of permeability are non-dimensionalized using the hydraulic diameter, D_p. The non-dimensional permeability, κ/D_p^2 is then plotted

against porosity, and compared against existing Koponen correlation [119] and the new porosity-permeability models developed in section 4.

6.5.3.1 Verification by Koponen Model

An equation of the form 6.26 is fitted to the iLBM simulation data and the values of non-dimensional permeability, κ/D_p^2 from the numerical simulation produce an excellent fit with the Koponen correlation within its valid range ($0.42 < \phi < 0.85$) [119], as seen in figure 6.10 and figure 6.11, cementing the effectiveness of the presented random substrate generator.

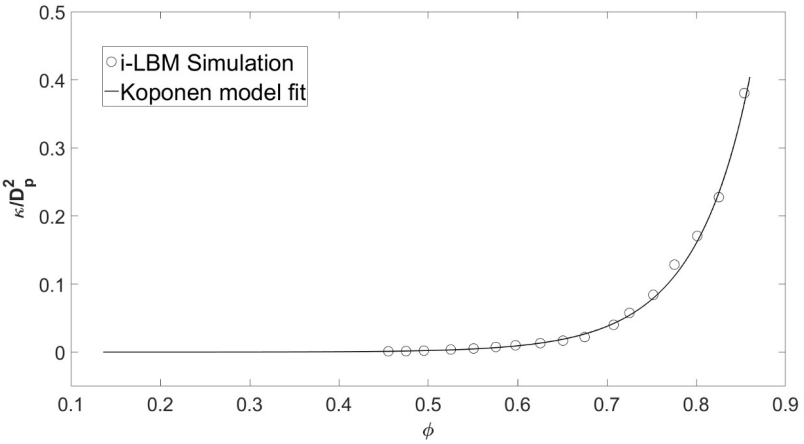

Figure 6.10: Non-dimensional permeability vs. porosity, fit to the Koponen model.

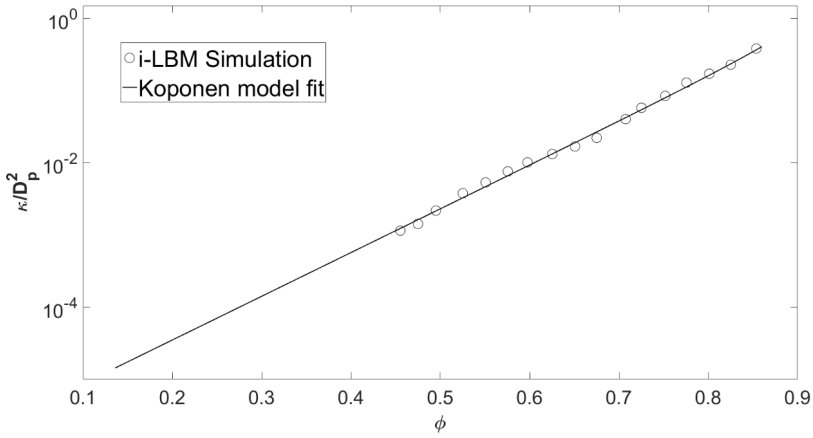

Figure 6.11: Semilog plot: Non-dimensional permeability vs. porosity, fit to the Koponen model.

6.5.3.2 Verification by Gebart-Brinkmann (GB) Model

As explained in the previous section, the GB model better approximates the underlying physics of flow through porous media capturing the essential concept of percolation threshold at low porosities and at the same time providing sound results at high porosities in agreement with previous models. The model strongly verifies our substrate generator showing that it is in compliance with the physics of porous flows at low as well as high porosities as can be seen in figures 6.12 and 6.13.

6.5.3.3 Verification by Gebart-Kubawara (GK) Model

The GK model fit to the data in figures 6.14 and 6.15 essentially shows the same trend as the results in the previous section for the GB model in figures 6.12 and 6.13.

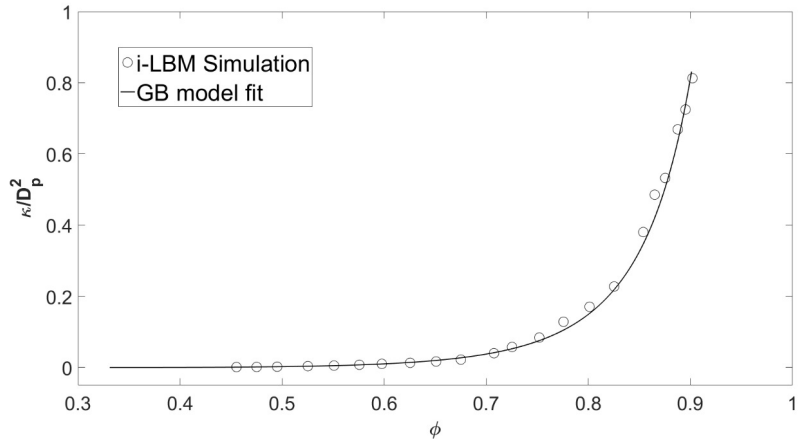

Figure 6.12: Non-dimensional permeability vs. porosity, fit to the GB model.

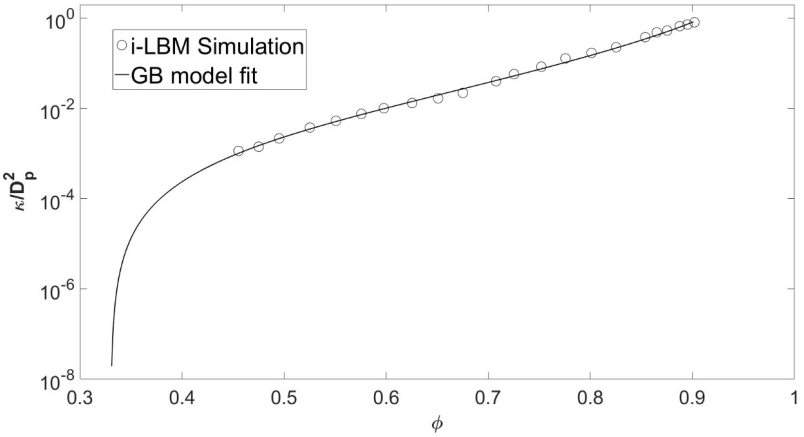

Figure 6.13: Semilog plot: Non-dimensional permeability vs. porosity, fit to the GB model.

This result is expected as explained in previous sections. The flow at high porosities in porous media can be modeled using the Cell Model theory as in the GK model or the flow past a submerged body theory as in the GB model. Both models are known to show similar results as stated in [122]. An additional benefit of the GK model is its wider range of validity at low porosities in comparison to the GB model.

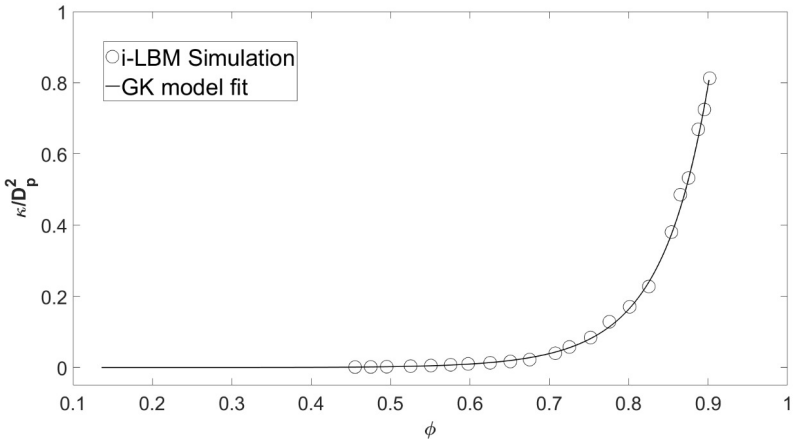

Figure 6.14: Non-dimensional permeability vs. porosity, fit to the GK model.

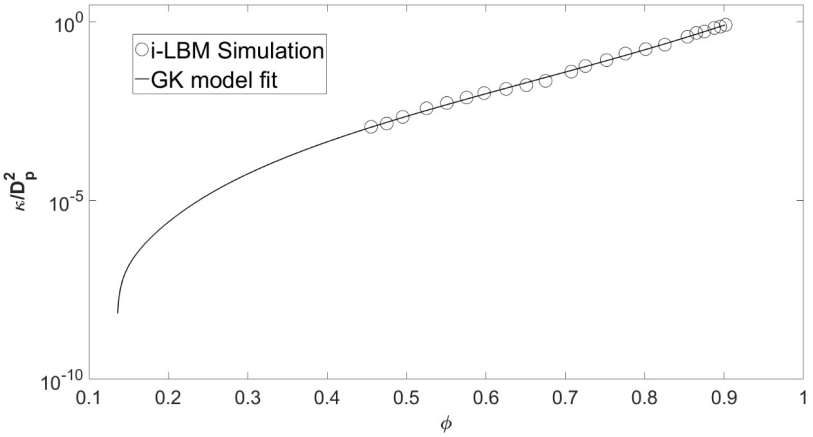

Figure 6.15: Semilog plot: Non-dimensional permeability vs. porosity, fit to the GK model.

6.5.4 Experimental Verification

Finally the data for non-dimensional permeability found using the iLBM simulation and the random substrate generator is compared against data from experiments in [119, 120]. The experiments in [119, 120] were performed with fiber mats and fibrous

filters and the permeability was non-dimensionalized using a characteristic diameter, $D_c = 5$. Therefore, the experimental results were scaled by a factor of $D_c^2/D_{p,avg}^2$ and then compared with our simulation results. The value of $D_{p,avg}$ is taken to be the average of all values of D_p in the plotted range of ϕ. For the present simulation, the value of $D_{p,avg}$ is 12.43. The experimental results show very good agreement with our simulation data as shown in figure 6.16. This confirms the idea that our substrate generator can simulate different types of porous media effectively.

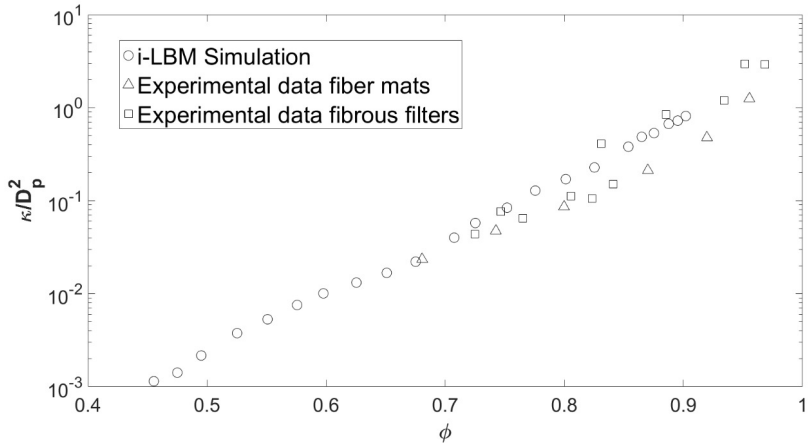

Figure 6.16: Semilog plot: Non-dimensional permeability vs. porosity.

6.6 Conclusions

Filtration and flows through disordered porous media play a substantial role in many physical and engineering processes. However, methods for obtaining or generating substrate geometry for the well-suited lattice Boltzmann method can be cumbersome or physically prohibitive. This work provides a pseudocode and description of a

method fundamentally built on randomly sized and placed ellipses which is flexible, quick, and easy to implement for engineering studies. The subsequent results section utilized well established semi-empirical tools to test the methods validity, such as the Ergun equation and the Koponen correlation. The data collected from such runs produced intricate well-visualized images for pore scale understanding, something not possible with model equations or representative volume analyses. More importantly, the results showed excellent agreement ranging from the fundamental Darcys law to the most complex correlations and multi-substrate experimental data. Due to the methods ability to produce very complex shapes and patterns from what is a fundamentally simple shape, the ellipse, the performance matches physical scan and more complex generation methods without over complicating a key step in many studies. Thus, it is recommended as a porous media study tool.

Not only is the method shown to repeatedly produce valid substrates, the study reveals important CFD methodology in pore-scale analysis. A singular form incompressible multiple relaxation time lattice Boltzmann equation was important in limiting compressibility effects and small geometry feature artifacts. The bounceback scheme, and its variants, handle the inherently random geometry in a tractable manner. Reasonable lattice Boltzmann unit boundary condition values for primitive variables such as velocity and pressure are also a result of the successful analyses. This study adds merit to the growing interest in the lattice Boltzmann method in complex geometry flows.

Of additional interest is that the study of this method resulted in a secondary development in the form of a blending-function based correlation describing permeability variations in different types of porous media over a wider porosity range. Each of the contributing model equations describes the phenomena in different porosity regimes, but together increases the breadth of validity. The blending-function correlations are valid at porosities as high as 0.9. The model also successfully incorporates the phenomenon of zero permeability at a low finite value of porosity, (percolation threshold). This essentially helps to differentiate between porosity and effective porosity which is of utmost significance in all real porous media.

Since porous media is commonly a filtration mechanism, multiphysics capabilities are an interest in future studies. Conjugate heat transfer in non-isothermal filter flows should be straightforward based on the recent lattice Boltzmann literature. A multitude of methods are available for multiphase transport, deposition, and erosion, including layered advection-diffusion lattice Boltzmann equations and lattice gas cellular automata, both compatible with the substrates generated by the studied algorithm. Also of future interest is the extension to three dimensions, which is possible due to the fundamental use of basic mathematical equations valid in two and three dimensions to turn simple shapes into complex patterns.

Chapter 7

Multiphysics and PM Filtration

Research objectives 1, 5, and 6 have been achieved and validated in the preceding chapters. Thus the initial focus in this chapter is objectives 3 and 4, the last constituents to objective 7. This particle transport and capture, and conjugate heat transfer methodology is incorporated to realize the ultimate goal of an after treatment model which offers advances beyond previous literature. Several approaches are employed to quantitatively validate and verify the approaches, but ultimately, parametric studies must be employed to qualitatively verify the model, as in previous literature. Fortunately, there are several correct trends and order-of-magnitude measures of filtration activity available in modeling and experimentally focused literature. Relationships between physical and lattice Boltzmann units which have been applied to obtain physically meaningful results are presented and derived in appendix C.

7.1 Heat Transfer

It is well established that the D2Q9 lattice with the standard EDF 3.4 is sufficient for recovery of the non-linear NS equations as well as the uncoupled linear advection-diffusion equation 3.15 [51]. However, if fewer lattice velocities can be utilized for the simplified energy equation, then greater computational efficiency can be achieved on large and complex grids. This section shows that the simpler D2Q4 lattice is sufficient and accurate for the thermal physics of interest to the dissertation.

7.1.1 Recovery of the Advection-Diffusion Equation

The first way in which the D2Q4 lattice is found to be sufficient is through the Chapman-Enskog expansion. In appendix B.2 the procedure is utilized with a four velocity lattice, and simplified EDF (second equation of set 3.17). The result is recovery of the desired equation, 3.15.

7.1.2 Numerical Results

To test the findings of appendix B, two complex flows are resolved and compared with both the D2Q9 and D2Q4 lattices, the lid driven cavity, and microchannel parallel

plate flow. The results of section 4.2.2 (SRT-iLBE) serve as the flow solver.

7.1.2.1 Thermal Lid Driven Cavity

In the LDC simulation, the top plate is both translating in the $+x$-direction and maintaining a constant $T_{lb} = 1.0$ which advects and diffuses into the flow. All walls are no-slip. The side walls are adiabatic, and the bottom is maintained at a constant $T_{lb} = 0.1$ to remove energy from the system. Thermal boundaries are implemented with a half-way bounce-back condition similar to the flow BC. Re 100, 400, and 1000 are evaluated, both forming a complex flow and thermal simulation to reliably check the D2Q4 capability. The Pr in both cases is 0.71. A 257x257 grid is utilized in all cases and convergence is achieved when both RMS velocity and temperature residuals are below $1.0\text{E} - 6$.

Table 7.1
Temperature at points along the vertical x centerline of the LDC with D2Q4 and D2Q9.

y/N_y	Re 100		Re 400		Re 1000	
	Q4	**Q9**	**Q4**	**Q9**	**Q4**	**Q9**
0.2	0.5094	0.5097	0.8656	0.8653	0.8902	0.8892
0.4	0.8037	0.8039	0.8969	0.8949	0.8691	0.8669
0.5	0.8634	0.8631	0.8881	0.8857	0.8699	0.8673
0.6	0.8797	0.8787	0.8877	0.8851	0.8698	0.8672
0.8	0.8509	0.8498	0.8713	0.8695	0.8715	0.8697

Across all Re, the D2Q4 version was 26% faster, on average, than the D2Q9. The agreement between the two methods, shown in table 7.1 is excellent, being as close as

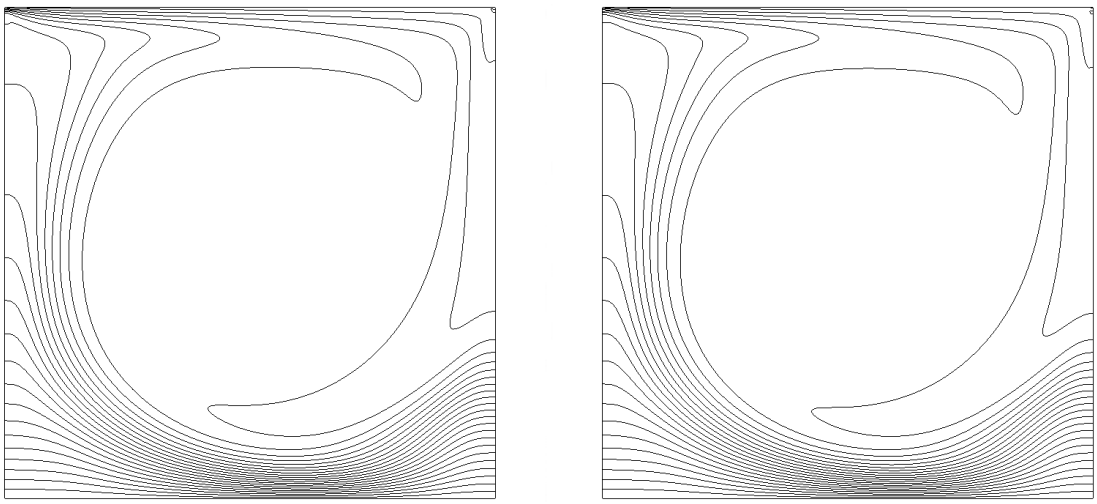

Figure 7.1: *Re* 1000 LDC temperature contours, D2Q4 left and D2Q9 right.

any two different numerical methods are likely to be. Temperature contours in figure 7.1 are virtually identical.

7.1.2.2 Conjugate Heat Transfer-Channel Flow

To inspect the D2Q4 and D2Q9 solutions with conjugate heat transfer a channel flow with wall thickness similar to the channel height is considered. Figure 7.2 displays the domain and table 7.2 summarizes the parameters. A four velocity and nine velocity lattice is applied to both the solid and fluid domains. The benefits of LBM for conjugate heat transfer (CHT) are realized here, and no special treatment besides a change in thermal diffusivity is required for the relevant domain. Half-way bounce-back is utilized at the interface for the no-slip boundary between fluid and solid domains. A constant body force drives the flow to represent a pressure gradient, and

periodic boundary conditions are enforced at inlet and outlet. A constant temperature inlet is applied, and the flow convects heat out of the system as it passes by the plates. The plates generate a constant heat and the non-interface walls are adiabatic. The Buick-Greated scheme [126] is used for the flow driving body force and to treat the heat generation as a body force in the thermal LBE. A 200x120 grid is utilized in all cases and convergence is achieved when both RMS velocity and temperature residuals are below $1.0\text{E} - 6$.

Contour lines are compared in figure 7.3 and the flow centerline temperatures are compared at several points along the channel axis in table 7.3. Again, agreement is excellent with centerline variation at the studied points of less than 0.4%, and the contour lines being nearly identical, showing that for the physics of interest here, a D2Q4 lattice is sufficient.

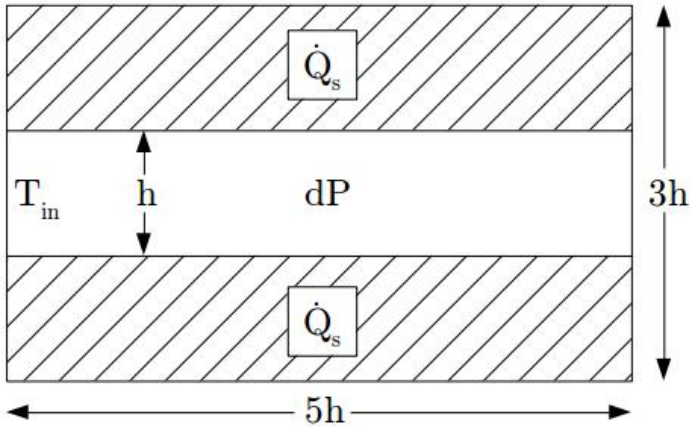

Figure 7.2: Conjugate heat transfer channel flow schematic.

Based on these results, it is strongly suggested that the D3Q6 lattice is proper for a

Table 7.2
Heated channel flow parameters (LB units).

Parameter	Value	Parameter	Value
$\dot{Q}_s$	$3.0\text{E}-8$	h	40
b_f	$3.0\text{E}-6$	T_{in}	1.0
$\alpha_f : \alpha_s$	4.0	ν	0.167

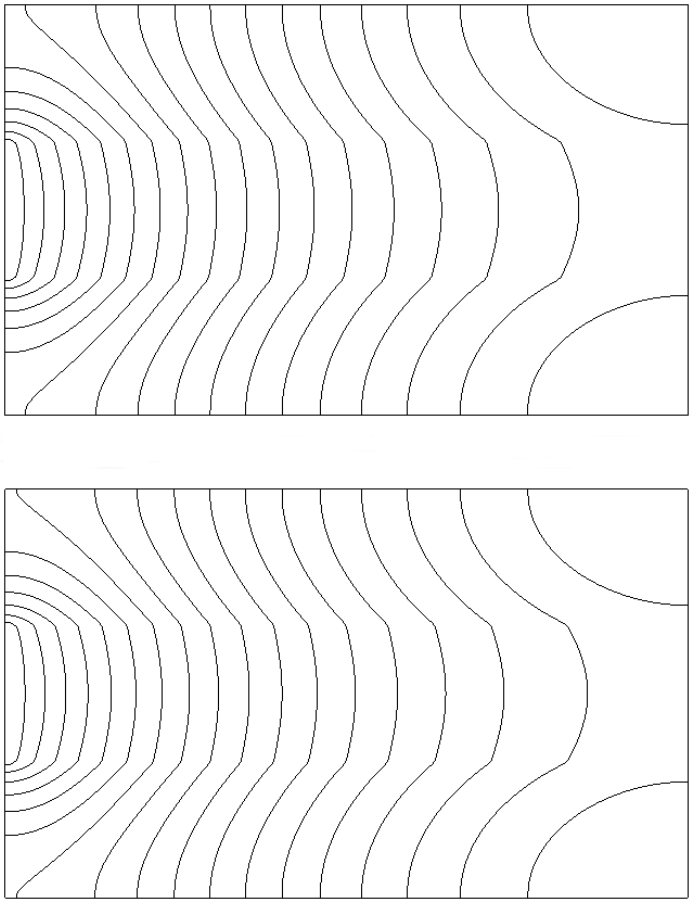

Figure 7.3: Conjugate heat transfer developing temperature profiles, D2Q4 top and D2Q9 bottom.

3D form of the advection-diffusion equation as well.

Table 7.3
Temperate at points along the centerline in the heated channel flow, D2Q4 and D2Q9.

x/N_x	**Q4**	**Q9**
0.2	1.044	1.043
0.4	1.081	1.078
0.5	1.097	1.094
0.6	1.112	1.108
0.8	1.138	1.134

7.2 Particle Transport and Deposition

7.2.1 Diffusion, Advection, and Deposition Bases

An Eulerian-LBE approach is utilized as described in the methodology section 3.1.7. Mass fraction (Y) replaces the transported variable, ρ in the standard LBE. Diffusion of the particles is controlled by the collision relaxation time τ_Y, governed by the mass diffusivity of particles estimated to be 100 nm in air, a Sc value of 95.1, from [127]. This is a departure from the methodology of Yamamoto's papers [43, 44] where τ_Y is set equal to τ with no justification or explanation. This is an inappropriate assignment since particle diffusion is two orders-of-magnitude lower than momentum diffusion. Therefore, based on our circumstances and Sc, $\boldsymbol{\tau_y : \tau = 0.0866}$, not 1 as in the Yamamoto works. Drag on the particles, and the relative momentum of each phase, means the particles share the same velocity field as the fluid flow.

Through the drag and diffusion forces, particles come close to, or in contact with the substrate and will deposit and be removed from the flow. A certain percentage of the particles will be close enough, and the molecular adhesion forces in the proper state, for deposition to occur. The mechanisms of deposition are extremely complex and local-condition-dependent, so the full simulation of the deposition and sticking activity is not conducted here. To the authors knowledge, no such simulation is successful on scales in the μm order-of-magnitude regime. LBE-Lagrange literature discussed in section 2.3.1 simulates some of these molecule, atomic, and subatomic forces, but on scales much smaller than evaluated here, required for application.

7.2.2 Implementation on a Lattice

In this discrete model, close is defined as a lattice node adjacent to the solid. If the lattice node is thought of as the center of a lattice cell, occupied throughout by the concentration of particles, some will actually be closer to the substrate than others and/or be in a better location for the attractive forces to act. Therefore, a probabilistic approach is taken. Particles on a lattice node adjacent to the substrate deposit with probability P_s, and continue to advect and diffuse with probability $1-P_s$.

As a result, two values for Y are tracked. Y_1 is available for transport and is utilized in the LBE evolution equation, and Y_2 which is the amount deposited and unavailable

for transport. Particles are thus being removed from the flow, creating the filtration effect. Eventually a node/cell becomes loaded when $Y_2 = 1$, and that cell can no longer transport particles or fluid. The thermal characteristics are also altered. Figure 7.4 displays the progress of deposition in time. Filtration does not end there, as the nodes adjacent to the now solidified particle-loaded node are available to collect more particles per the defined rules. An erosion model could be introduced here if another probability were to define conversion of Y_2 back to Y_1. To provide additional sophistication to the model, sticking on a particular boundary node can only proceed if a search algorithm concludes there are at least three other nearby boundary nodes. This prevents formation of unrealistic long growths which would be unstable due to fluid flow momentum.

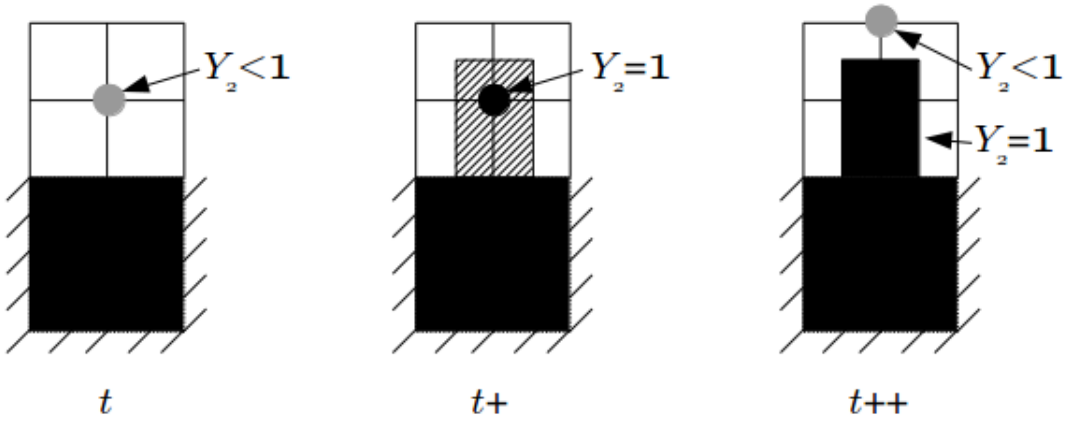

Figure 7.4: Deposition progression.

7.2.3 Numerical Results

The purpose is to assess validity quantitatively with the conservation principles, and qualitatively with what we would expect from the rules implemented. For example, we know that particle mass must be conserved, in addition to fluid mass. In a filtration system where the domain is effectively a control volume, the statement which must be satisfied is

$$\left.\frac{\partial m}{\partial t}\right|_{CV} - \left(\left.\frac{\partial m}{\partial t}\right|_{in} - \left.\frac{\partial m}{\partial t}\right|_{out}\right) = 0. \tag{7.1}$$

Qualitatively, the flow should be dominated by advection over diffusion due to employed Sc, with some diffusion still visible. As a result, the unsteady nature of the particle concentration should follow that of the the velocity field. The creeping Stokes flow present in most filtration means that collection should occur relatively evenly, but with some greater front loading.

7.2.3.1 Backward Facing Step

Only transport mechanisms are first studied with the backward facing step. From initial conditions of zero velocity and zero particle concentration flow begins to enter

the domain with a parabolic profile and constant species concentration. The vortex formation after the step distributes the particles, and the shorter time scale of diffusion transport limits distribution across the flow streamlines.

The definitive D2Q9 incompressible solver is used. The simulation has a velocity inlet and pressure outlet. The walls are no-slip. A constant mass fraction of $1.6\text{E} - 4$ is applied at the inlet and the domain is unpopulated with particles initially. However, all data are presented as nondimensionalized values, so a mass fraction of one here represents a value equal to the inlet. A step height Re of 300 is utilized to demonstrate transport in a complex flow. Development is pictured in figure 7.5 at regular time steps. Viscosity dominates mass diffusion.

At a relatively coarse grid of 721x79 the mass balances to less than 0.5% at the steady state. At a more refined grid of 901x99 the mass balances to 0.125%, and at 1081x119 it is under 0.03%. Mass is conserved and the rate of convergence is higher order.

In examining figure 7.5, it is clear that qualitative metrics are met. Advection dominates and the development of vortices in the flow is immediately followed by the particle concentration Y. Only in more advanced stages is diffusion evident from the lack of sharp edges in the concentration and smearing perpendicular to the local flow direction. In comparison, the same simulation with $Sc = 1$ is shown at $ts = 20000$ in figure 7.6. While advection still clearly dominates, the particles have thoroughly diffused to occupy parts of the domain which do not receive as much direct flow through

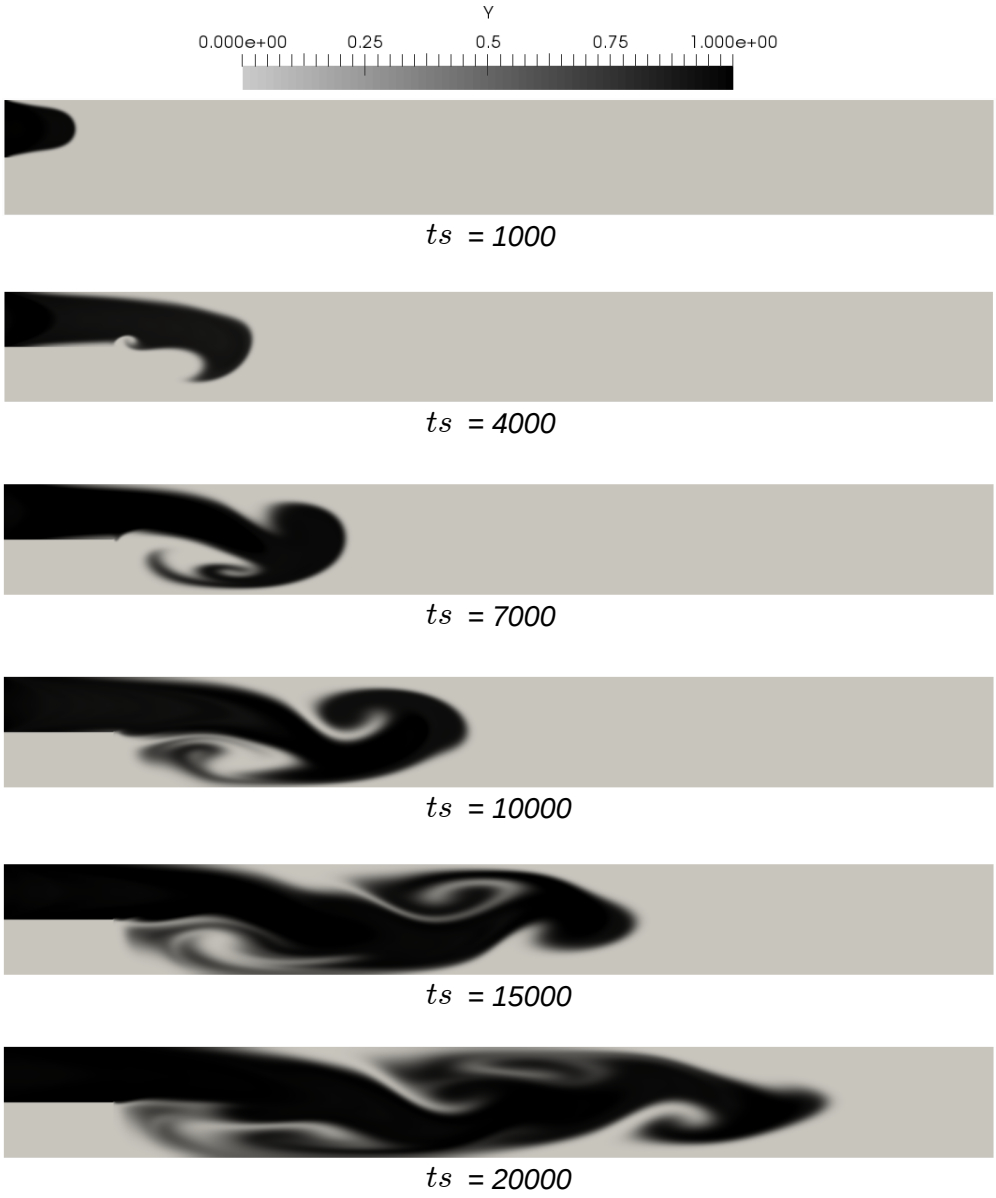

Figure 7.5: Advection and (weak) diffusion of particles in backward facing step.

advection. No sharp distinction remains between particle laden and particle-free flow. The scale of Y is the same to present a clear trend.

This result draws attention to why it is critical to correct the assumption related to

Sc and collision relaxation time in Yamamoto's works [43, 44].

Figure 7.6: Advection and stronger diffusion of particles than figure 7.5 at $ts = 20000$.

7.2.3.2 Cylinder in Flow

To test deposition, a no-slip cylinder in a cross flow is made available for particle sequestration per the capture algorithm. A single cylinder in a flow offers several advantages for validation purposes such as the similarity between a grouping of cylinders and a filter substrate, and focused visualization of the process. In order to accelerate the simulation without altering the bases or validity of the assumption, the inlet mass flow rate of particles in is set high by combining a particle concentration of $1.6\text{E}-4$ with a relatively high $\boldsymbol{u}_{lb} = 0.1$. Additionally, P_s is set to 80%, D is equal to ν, and a coarse grid of 201x100 is utilized.

Quantitatively, mass balance is measured with equation 7.1 by summation of: the known inlet mass, resultant outlet mass, and the sum of mass sequestered in the deposited soot "nodes/cells" around the cylinder. All computation is based on constant PM density and lattice cell "volume". Qualitatively, the pattern of formation around the cylinder and the change in streamlines diverting around the blocked nodes are

tracked in time.

Figures 7.7, 7.8, and 7.9 show the progress of deposition in time. Figure 7.10 shows the change in streamlines in time as deposition diverts flow. As one layer is laid down the next begins collecting on top. As is expected for creeping flow, the collection occurs predominantly at the front where there is a limited stagnation zone. Once this process starts, further deposition favors the front. Flow diverts around any mass collection at each step. This more complex task of balancing mass, analyzed by discretizing the Reynolds transport theorem:

$$\frac{\partial}{\partial t}\int_V Y dV = \int_S Y(\boldsymbol{u}\cdot\boldsymbol{n})dA \tag{7.2}$$

is satisfied to within 3%, which for such a coarse grid, a simulation which can never reach a true steady state, first-order geometry representation, and a tractable process, is considered good.

To test parameter sensitivity and change in qualitative patterns, an additional simulation is run on the same grid, but with a quarter the first sticking probability. Not only is the collected PM at $ts = 300000$ notably lower, but the distribution is more even. This is expected since particles which usually stick to the front half of the cylinder are now available for downstream flow and deposition. Figure 7.11 displays

the PM deposition concentration at $ts = 300000$. Where 80% sticking probability resulted in 7 layers of soot deposition on the front and 5 at the rear, 20% results in only 5 layers at the front, and 4 at the rear.

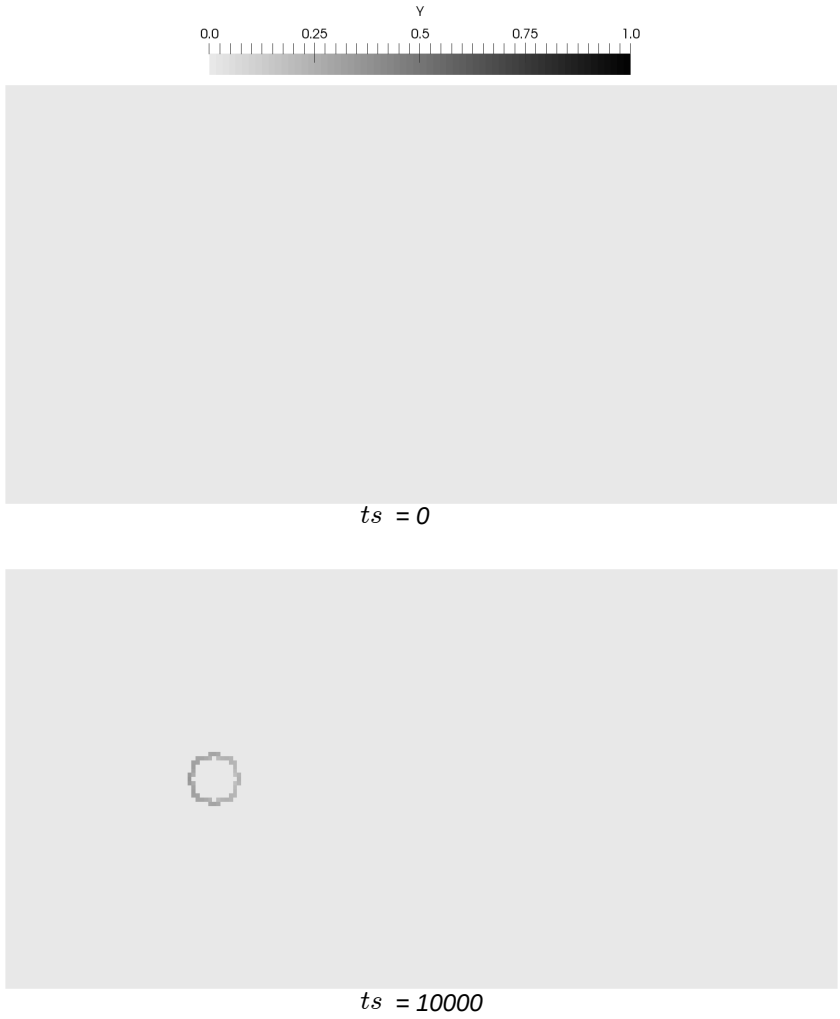

Figure 7.7: PM deposition on cylinder in flow: initial condition and deposition to $ts = 10000$.

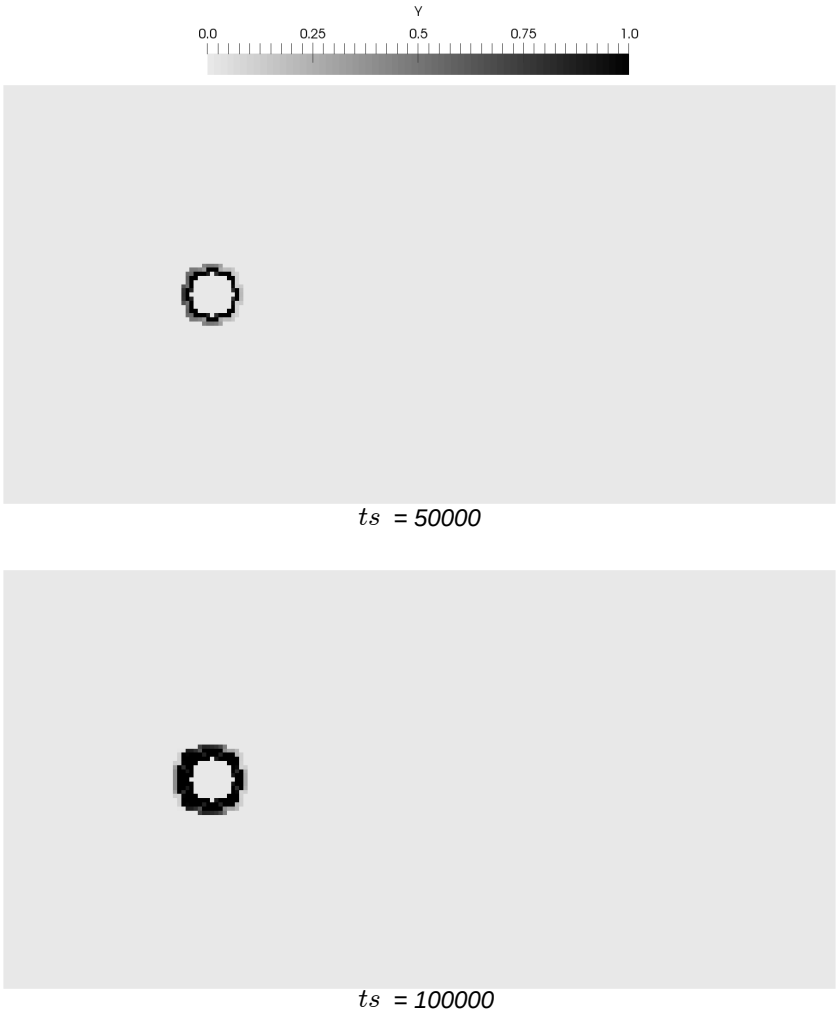

Figure 7.8: PM deposition on cylinder in flow: $ts = 50000 - 100000$.

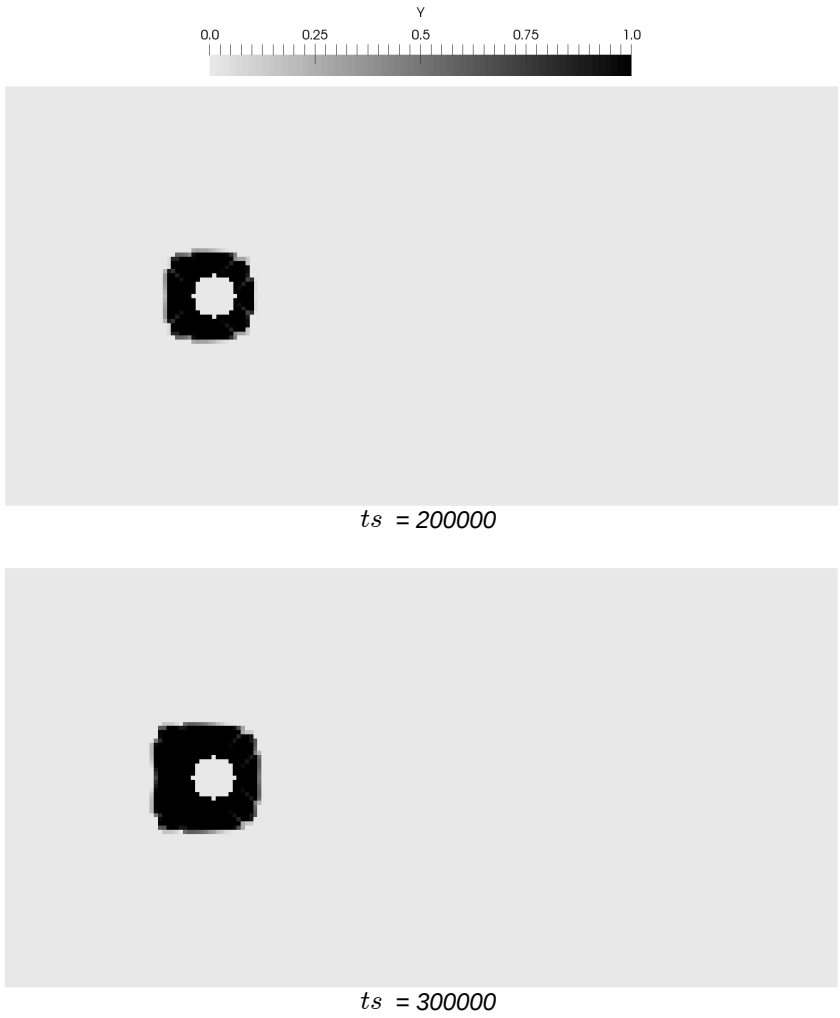

Figure 7.9: PM deposition on cylinder in flow: $ts = 200000 - 300000$.

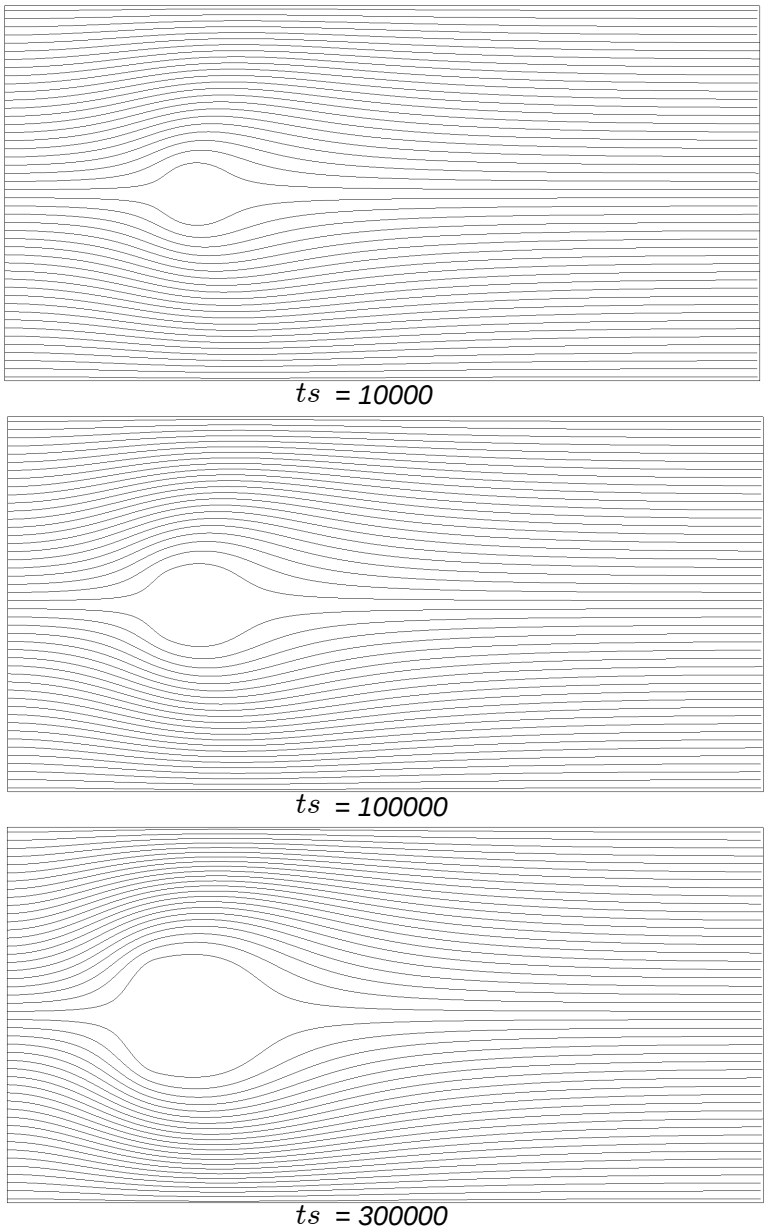

Figure 7.10: Streamline changes due to PM deposition $ts = 100000 - 300000$.

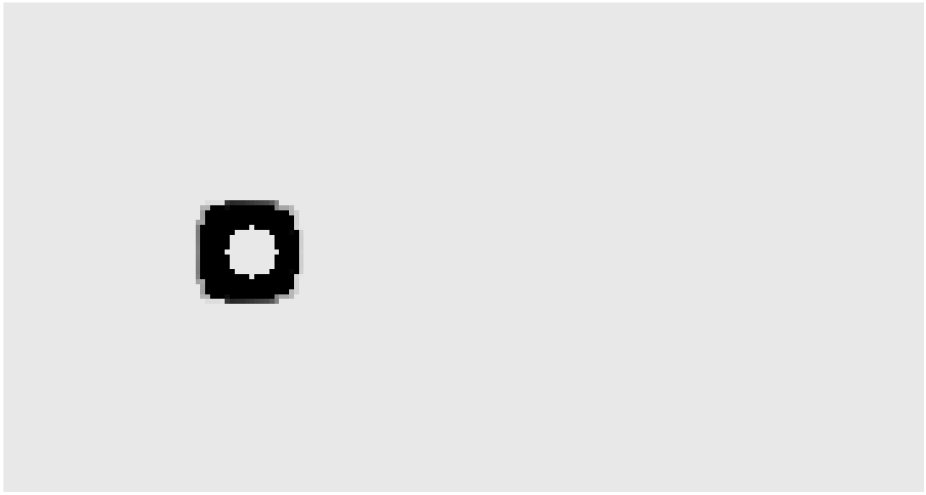

Figure 7.11: PM deposition at $ts = 300000$ with low sticking probability.

7.3 Full Coupling in a Filtration Model

A comprehensive parallelized multiphysics code has been the largest and most central objective of this dissertation. In this section, all prevoius research except the turbulence study has been synthesized and implemented. Several porosities and sticking probabilities will be tested to show the proper patterns of filtration and thermal development. In addition to studying patterns in the filter as a whole through a series of images, all cases track species and temperature development along a line running from inlet to outlet halfway along the substrate, as well as the pressure increase at the inlet. Simulations end when the collection of particulate matter causes a substantial restriction of flow, representative of a loading filter.

Velocities and temperatures are normalized by the inlet value, and pressure by the outlet. Position is normalized by filter wall thickness (L_{filter}). These values are then shifted so that the actual filter wall begins at 0, negative values are the inlet area, and values greater than 1 are the outlet area. Species concentration is reported on a scale of 0 to 1 since these are absolute values and represent no concentration and full deposition, respectively. A characteristic time is defined as

$$t_c = \frac{2L_{filter}}{\boldsymbol{u}_{in}}. \tag{7.3}$$

Additionally, a filter loading percentage is defined as

$$\%\text{loaded} = \frac{\#\text{fully loaded cells}}{\#\text{cells in filter}}\text{x}100, \tag{7.4}$$

which compares the volume of deposited PM to the volume of the filter as a whole (solid and fluid space).

Even though graphical results are presented in normalized or non-dimensional values to achieve the most generalized and useful results, the proposed conversion system of appendix C is applied to the dependent variables in some graphs, and marked in **bold** within the text.

Before presenting specific results, it is important to point out basic trends that provide credibility to subsequent model results. Increases in sticking probability reduce the amount of soot species leaving the domain at any given time step, and over the entire run. Pressure at the inlet increases with the increase in soot buildup. Maximum velocity in the domain also increases with soot buildup, as the effective flow area reduces. The components of velocity at every point are constantly adjusting in response. A reduction in porosity leads to a reduction in species mass flow out of the domain. This is observed both when the filter starting porosity is altered, and when porosity becomes altered by the collection of soot on the filter surfaces. Deposition

occurs on the leading substrate nodes first before proceeding to deep bed filtration. Higher sticking probability leads to predominantly front loading the filter, while more moderate probabilities and porosities experience deep bed filtration.

7.3.1 Low Porosity and High Sticking Probability

Table 7.4 summarizes the parameters utilized for the study in LBM units. Reported results for temperature and velocity are normalized by the inlet value.

Table 7.4
Low porosity & high stick filter test parameters.

Parameter	Value	Parameter	Value
Re	3.26	u_{in}	$0.001\hat{i} + 0\hat{j}$
Pr	0.68	T_{in}	0.01
Sc	95.1	Y_{in}	$1.6\text{E} - 4$
P_s	0.99	T_0	0.005
ϕ	0.603	$\dot{Q}_{substrate}$	$-1.0\text{E} - 6$

Back pressure at the inlet due to the substrate and deposited materials is of great interest to filter simulation. With a fixed atmospheric outlet pressure, the inlet pressure should increase with time (deposition), tending non-linearly toward infinity at a fully loaded filter. In figure 7.12, pressure builds with increasing iterations. The trend accelerates as time passes and the filter experiences greater loading. While the trend is exponential, the actual increases come in uneven intervals. This is due to the nature of soot deposition frequently changing the preferred pathways, and deposition

on secondary, tertiary, etc... layers causing different further deposition patterns and rates (deposits can build upon substrate and old deposits). Over this initial portion of the loading process, pressure has already increased about **900 Pa**, in physical units.

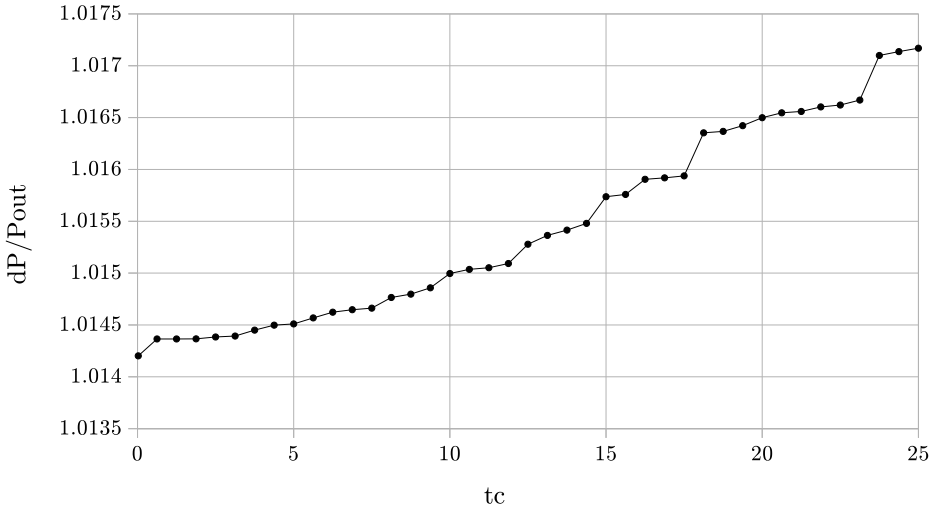

Figure 7.12: Pressure increase with time (soot deposition) (low porosity and high sticking probability).

Specifically along the centerline, the time-dependent pressure trend vs. filter wall depth is presented in figure 7.13. Apparent discontinuities are the result of solid substrate. Not surprisingly, there is a complex downward trend at all times. As the soot levels build the pressures are largely simply scaled upward, always returning to the same outlet value.

Capture of PM is the primary goal of a filter, and in figure 7.14 the center line species concentration is tracked through the filter depth. As a note, a zero concentration is converted to $1.0\text{E}-8$ to allow a logarithmic ordinate in order to more clearly represent

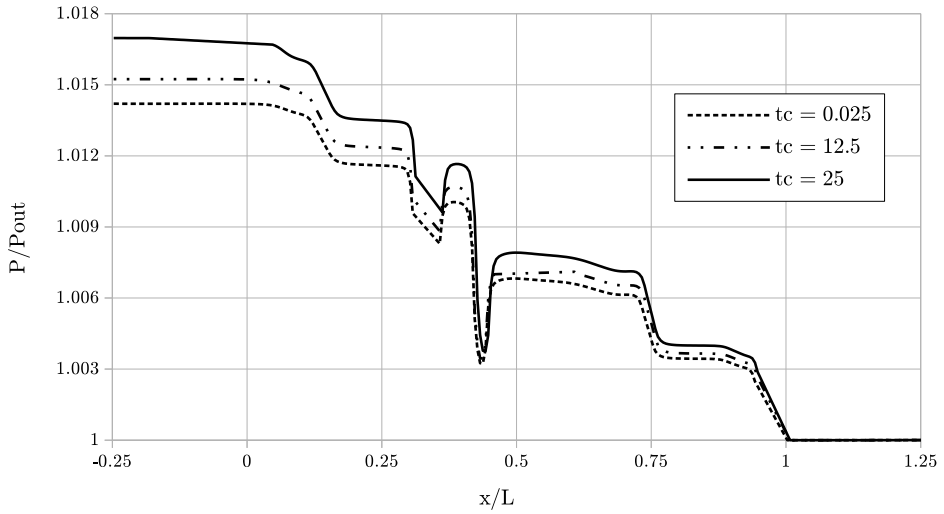

Figure 7.13: Pressure history along the centerline (low porosity and high sticking probability).

the large orders-of-magnitude differences present in species concentration.

The center line of this particular filter is a fairly active site of deposition due to the passage locations of the randomly generated substrate. The high sticking probability and low porosity lead to concentration peaking early on at the start of the susbtrate (x/L = 0). This doesn't exclude deeper deposition, around 10% and 20% into the filter, even though the initial pore blockage restricts flow along the line.

With passing iterations, the initiation sites are the ones that show the most growth. Other sites appear, but remain relatively small. The front loading nature of these parameters is particularly apparent in the final graph where substantial deposition is not only reached, but about a dozen layers ahead become fully loaded.

A better overall picture of the deposition process is seen in figures 7.15 and 7.16.

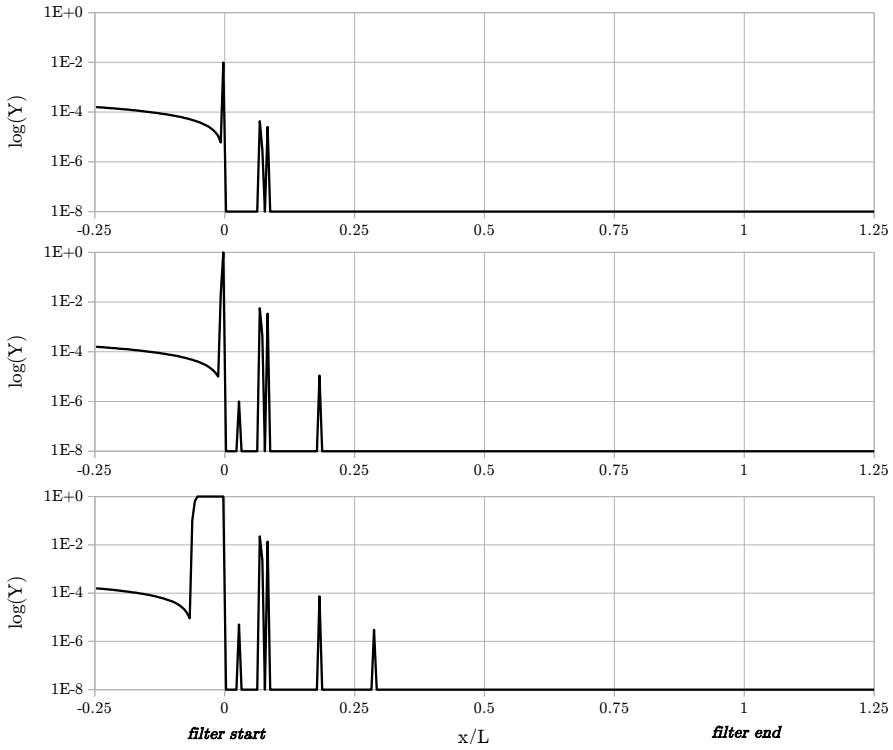

Figure 7.14: PM concentration at the y-center line at $t_c = 0.025$, 2.5, and 25 (low porosity and high sticking probability).

Layers are being built near the entrance initially, and progress deeper with time. It can also been seen that the center line represented in the graphs above is fairly representative of an average section through the substrate normal to the inlet and outlet. At several locations near the the front of the substrate the layered deposition is close to bridging and completely closing passageways. "Horns" are also visible, an expected phenomenon based on the continuously rerouted flow paths and consistent with other deposition processes such as ice accretion on airfoils.

The image and patterns are further verified by comparison to Kang *et al.* [64], which show very similar patterns and progression in their smaller scale deposition analysis

of a fracture.

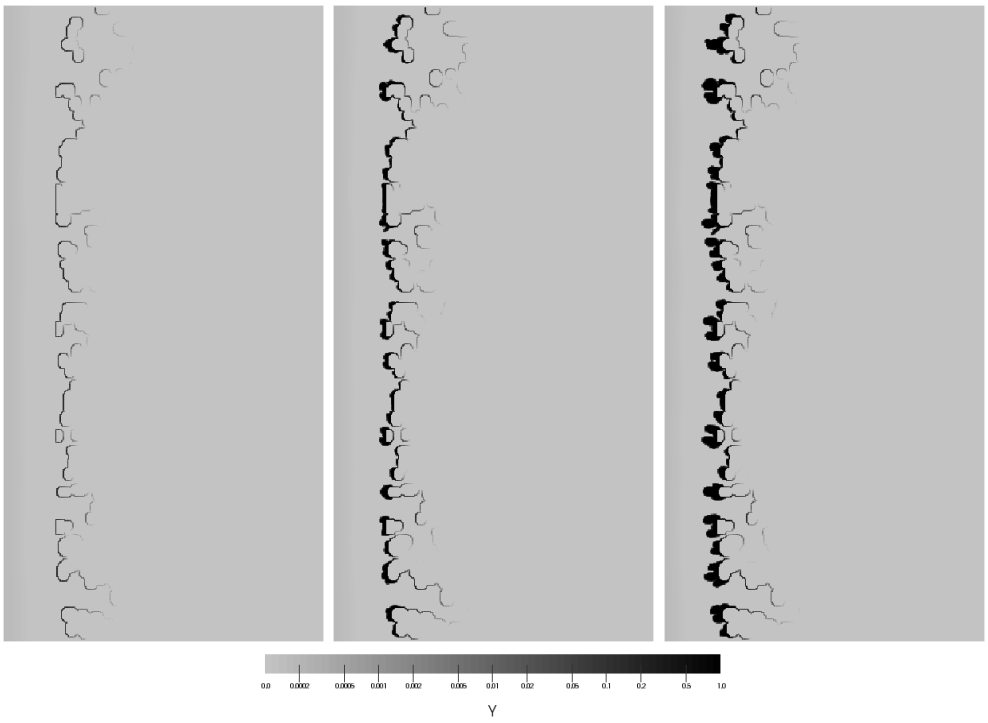

Figure 7.15: PM concentration at $t_c = 0.625$, 12.5, and 25 (low porosity and high sticking probability).

Filter loading levels and trends are important in filration analysis. In figure 7.17, the expected history of substrate loading is met. There is an initial delay, followed by a slow non-linear growth, leading into a roughly linear growth rate as seen in [43].

These deposits alter the flow paths by providing uneven and ever changing constrictions. The initial substrate provides the dominant velocity patterns. Initial deposition largely determines the velocity field change since it is then easier for deposition to occur in successive layers (increased flow contact area). In figure 7.18, the basic velocity field is visible at the initial time steps, but bulk and peak velocities increase as

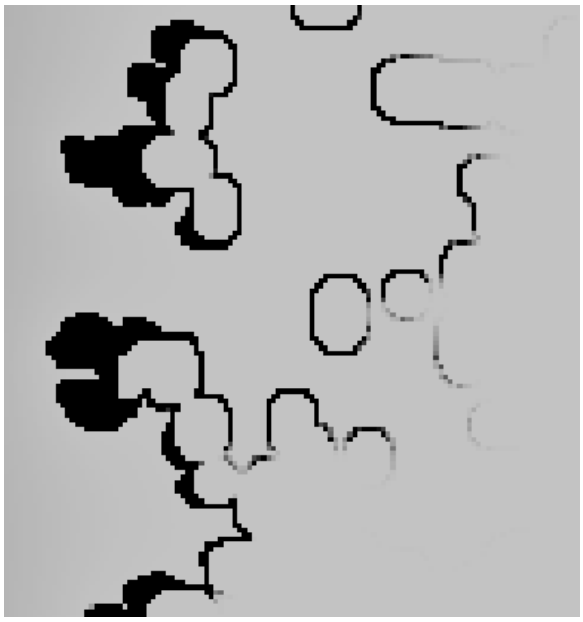

Figure 7.16: PM concentration closeup at $t_c = 25$ (low porosity and high sticking probability).

iterations proceed. There are effectively four or five main flow paths representing the paths of least resistance. No flow takes place in the central region.

The change from image 1 to 2 is relatively minor, although the path nearest the center does appear alterted noticably. Changes between image 2 and 3 are more profound due to the accelerating nature of layered deposition. The most central path is closing down. Paths toward the top of the substrate, and to a certain extent the bottom, are becoming preferred. The white patches, where velocity is zero, but also roughly representing substrate and deposits, are growing towards the inlet.

Temperature is also of concern in filer applications, and in figure 7.19 the progression of temperature is displayed along the same centerline used for the concentration study.

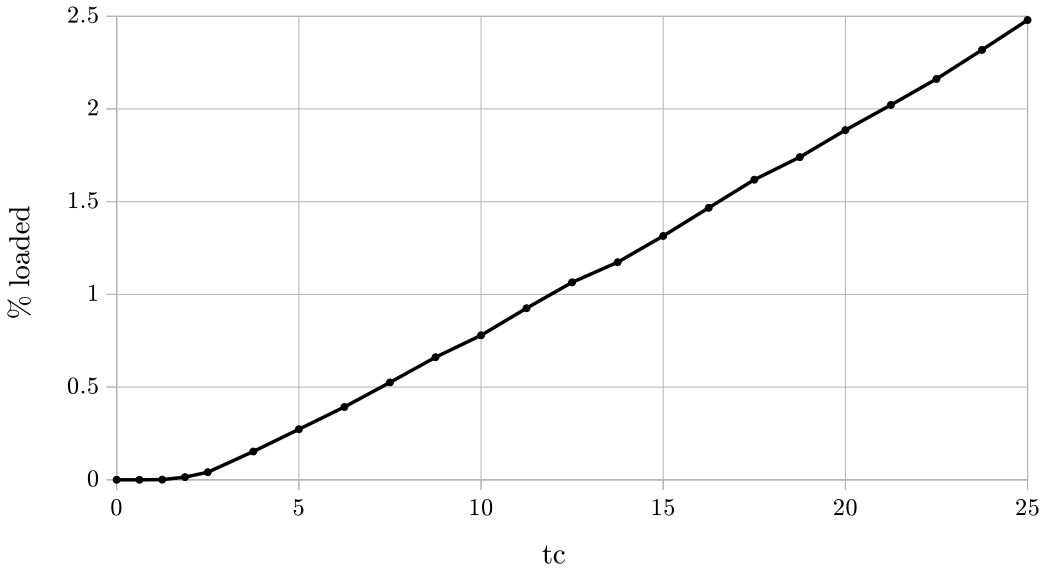

Figure 7.17: PM volumetric loading with time (low porosity and high sticking probability).

Because the substrate was given a fairly large negative energy source term (to remove heat from the incoming "hot" fluid and PM), and the substrate makes up about 60% of the domain, the temperatures drop substantially and quickly.

In a regeneration extension to the model, energy would be added to the domain as a source. The apparent unevenness in the model is as expected since the fluid predominantly convects temperatures, while the substrate the line passes through provides not only conduction, but the aforementioned heat removal. Thus, areas where substantial "jumpiness" is observed are areas of substrate.

An overall view of the domain temperature progression is displayed in figure 7.20. Heat is removed by the substrate as iterations progress. The apparent "blotchiness"

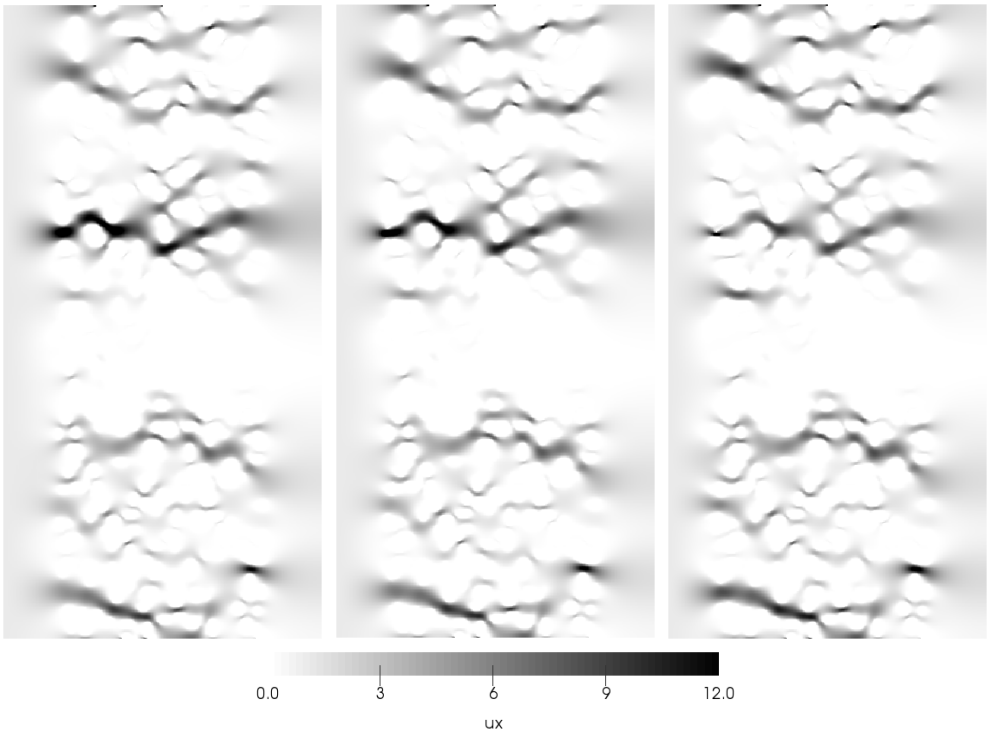

Figure 7.18: x-velocity at $t_c = 0.025$, 12.5, and 25 (low porosity and high sticking probability).

is due to substrate portions removing heat as warmer fluid is convected past. Higher temperatures are sustained deeper into the substrate where blockages aren't as near the inlet.

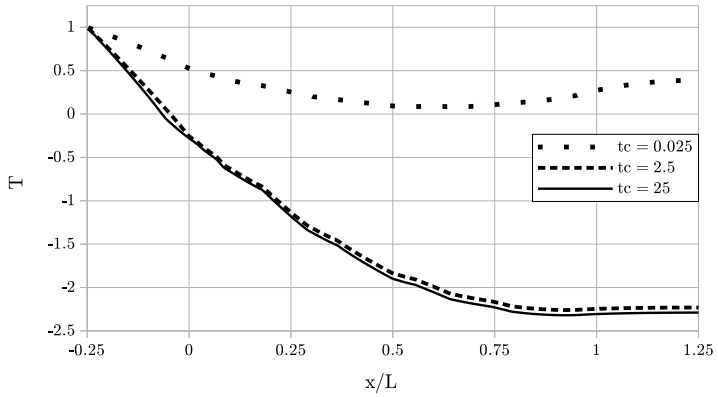

Figure 7.19: Temperature at the y-center line with time (low porosity and high sticking probability).

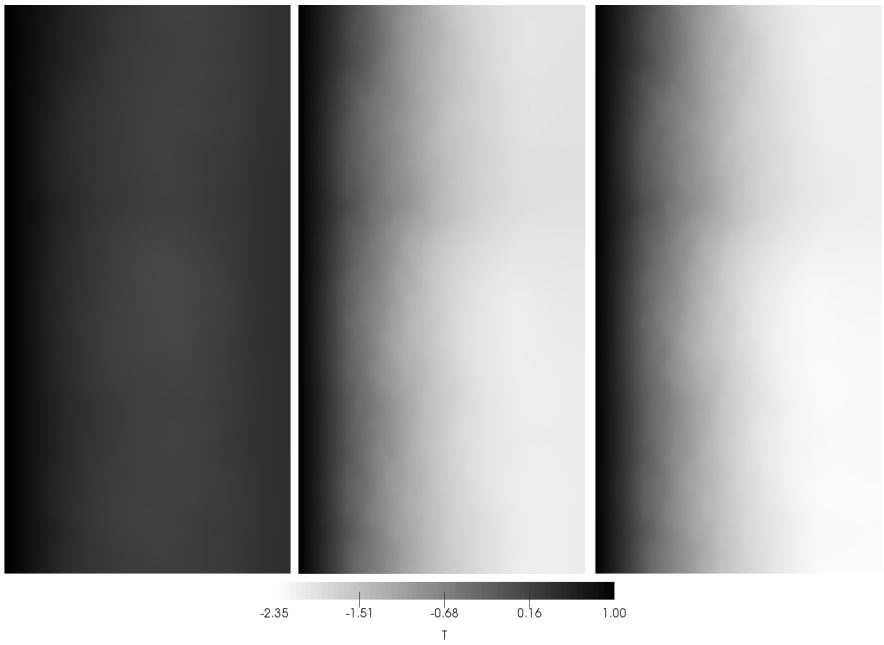

Figure 7.20: Temperature at $t_c = 0.025$, 0.625, and 1.25 (low porosity and high sticking probability).

7.3.2 High Porosity and Moderate Sticking Probability

Table 7.5 summarizes the parameters utilized for the study in LBM units. Reported results for temperature is normalized by the initial value, and velocity by the inlet.

Table 7.5
High porosity & moderate stick filter test parameters.

Parameter	Value	Parameter	Value
Re	49.4	u_{in}	$0.01\hat{i} + 0\hat{j}$
Pr	0.68	T_{in}	0.01
Sc	95.1	Y_{in}	$1.6\text{E} - 4$
P_s	0.8	T_0	0.005
ϕ	0.810	$\dot{Q}_{substrate}$	$-1.0\text{E} - 6$

In figure 7.21, pressure builds with increasing iterations. The trend accelerates as time passes and the filter experiences greater and deeper loading. However, compared to the last section, the loading does not accelerate as rapidly, and produces a smoother time history due to the lower sticking probability. The pressure increase along the center line follows the same basic high-to-low steps and drops, as seen in figure 7.22. However, the pattern is less complex due to the simpler substrate pattern.

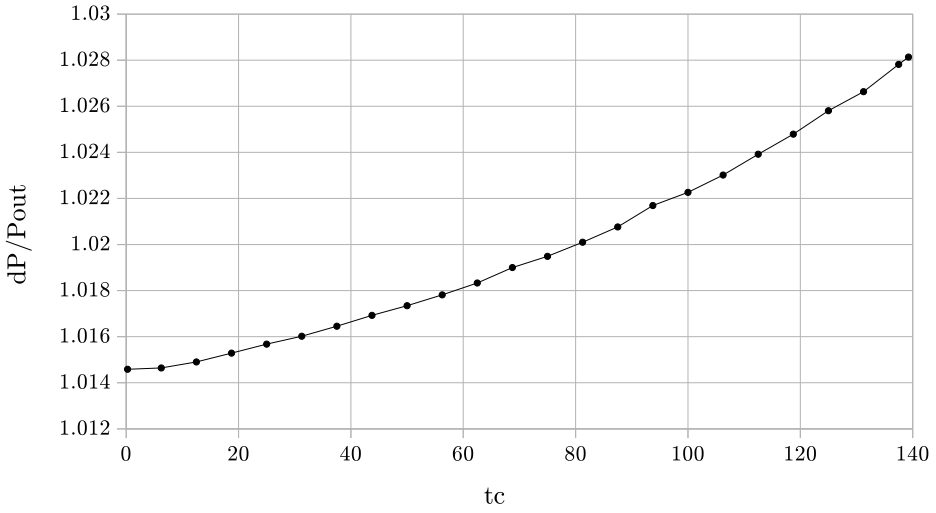

Figure 7.21: Pressure increase with time (soot deposition) (high porosity and moderate sticking probability).

The center line of this particular filter, compared to the previous study, is an active site for deposition due to a larger percentage of the PM being convected to preferred passages. However, since the inlet concentration is fixed and some portion of the concentration both convects and diffuses toward the substrate and deposits, some deposits near the entrance approach fuller loading by the final iterations. These concentrations are visibly growing towards the concentration value of 1 required to

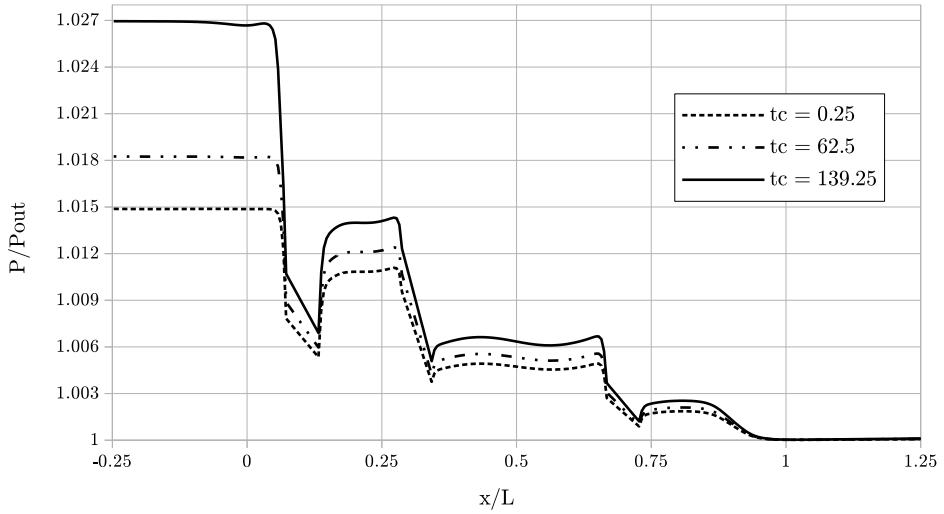

Figure 7.22: Pressure history along the centerline (high porosity and moderate sticking probability).

fill the lattice cell.

A view of the deposition process in the entire substrate is seen in figures 7.24 and 7.25. Concentration leaving the domain initially rises, but as more PM is deposited, the effective filtration area increases, and concentration leaving drops. This is due to collection of PM on top of additional PM. As a result it is as if the porosity of the filter decreases, with the corresponding increase in filtration effectiveness.

Loading percentage follows the same basic pattern with time. A higher percentage is achieved in figure 7.26, partially due to a smaller area to begin with.

New constrictions of various sizes and shapes arise continuously. The initial substrate provides the dominant velocity patterns. Initial deposition largely determines the velocity field change since it is then easier for deposition to occur in successive layers

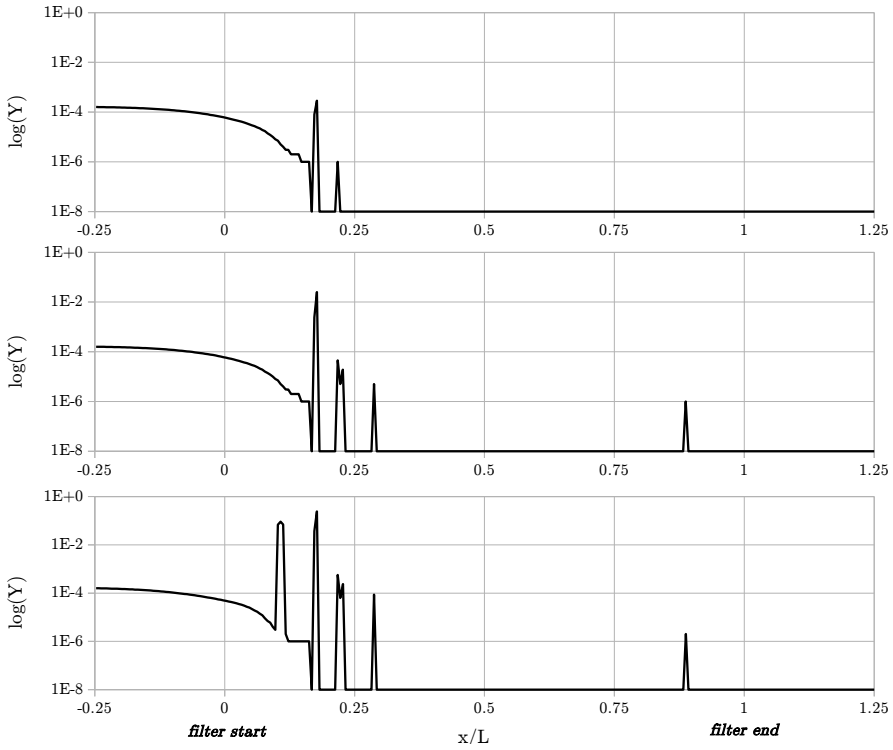

Figure 7.23: PM concentration at the y-center line at $t_c = 0.25$, 12.5, and 140 (high porosity and moderate sticking probability).

(increased flow contact area). In figure 7.27 the basic velocity field is visible at the initial time steps. Velocity increases as iterations proceed due to the reduced effective flow area.

In figure 7.28 the progression of temperature is displayed. Since the substrate occupies less area, despite the same negative source term, the drop in temperature is not as significant as the lower porosity studies.

A domain view of the temperature progression is displayed in figure 7.29. Heat is removed by the substrate as iterations progress. The apparent "blotchiness" is

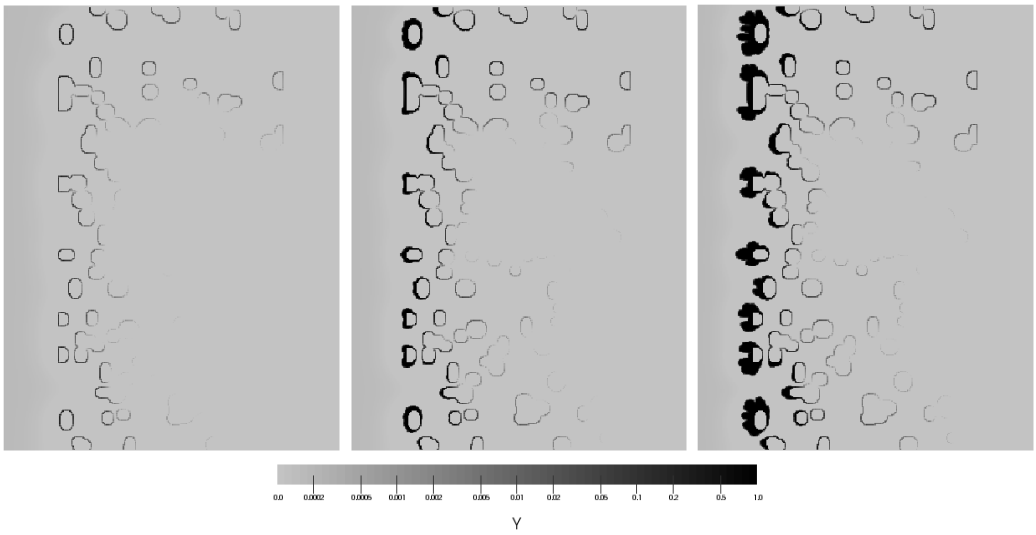

Figure 7.24: PM concentration at $t_c = 5$, 50, and 140 (high porosity and moderate sticking probability).

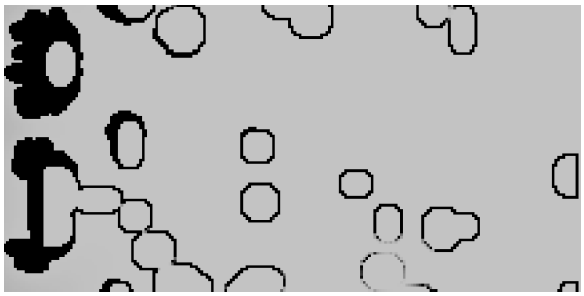

Figure 7.25: PM concentration closeup at $t_c = 140$ (high porosity and moderate sticking probability).

due to substrate portions removing heat as warmer fluid is convected past. Due to the relative low substrate volume, the temperature of the solid actually increases as opposed to low porosity studies.

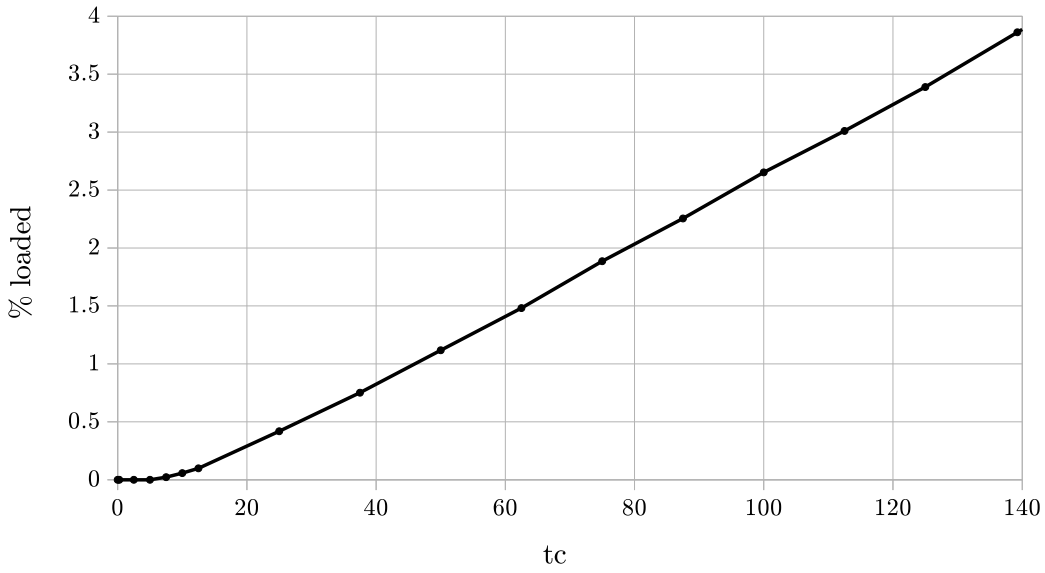

Figure 7.26: PM volumetric loading with time (high porosity and moderate sticking probability).

7.3.3 Low Porosity and Low Sticking Probability

Table 7.6 summarizes the parameters utilized for the study in LBM units. Reported results for temperature is normalized by the initial value, and velocity by the inlet.

Table 7.6
Low porosity & low stick filter test parameters.

Parameter	Value	Parameter	Value
Re	3.70	u_{in}	$0.001\hat{i} + 0\hat{j}$
Pr	0.68	T_{in}	0.01
Sc	95.1	Y_{in}	$1.6\text{E} - 4$
P_s	0.2	T_0	0.005
ϕ	0.593	$\dot{Q}_{substrate}$	$-1.0\text{E} - 6$

A noted increase in initial back pressure is expected over the high porosity case.

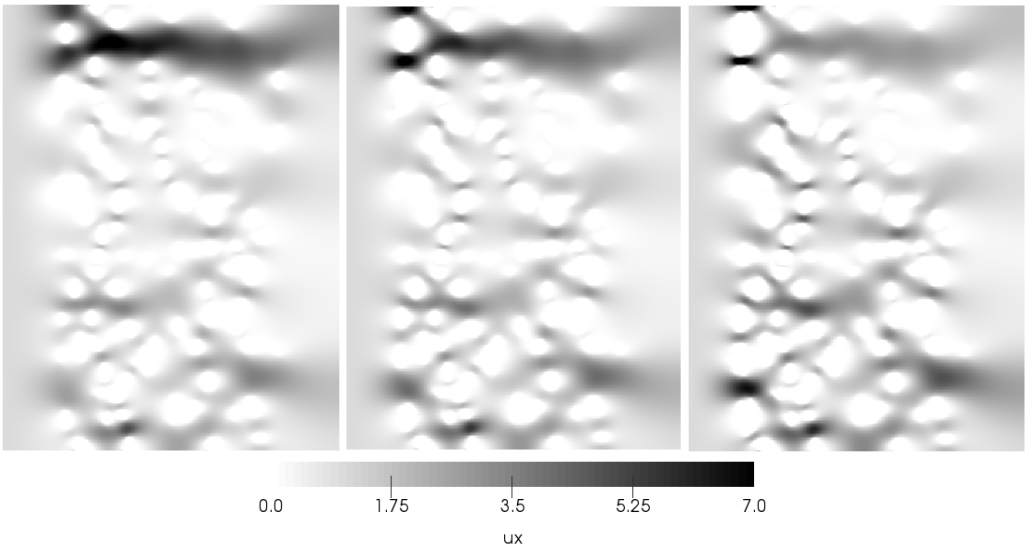

Figure 7.27: x-velocity at $t_c = 0.25$, 72.5, and 140 (high porosity and moderate sticking probability).

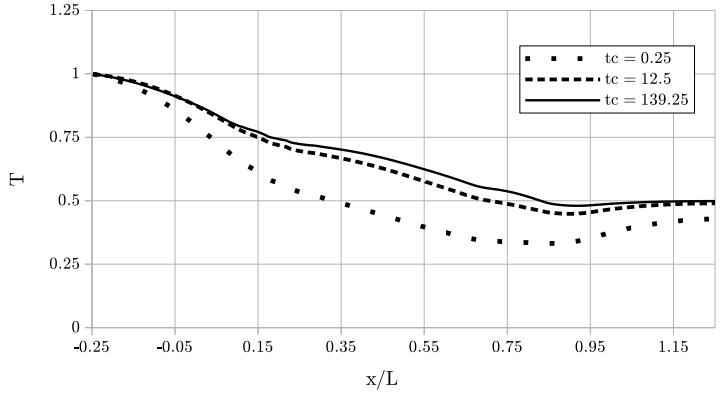

Figure 7.28: Temperature at the y-center line with time (high porosity and moderate sticking probability).

However, with lower sticking probability, it is not as simple as expecting equivalent or greater pressure rise rate. Rise in inlet pressure for this particular set of variables is seen in figure 7.30, where pressure builds with increasing iterations. The trend also accelerates with time and deposition, as well as loading proceeding to deeper portions

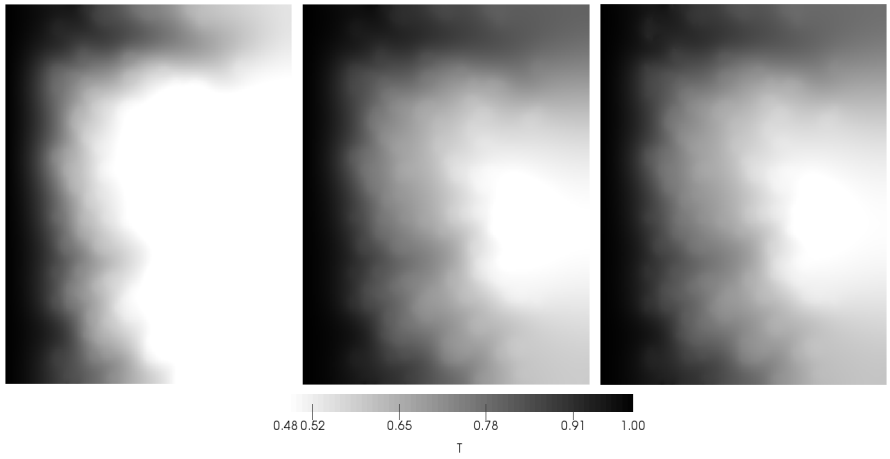

Figure 7.29: Temperature at $t_c = 0.25$, 2.5, and 37.5 (high porosity and moderate sticking probability).

of the filter later.

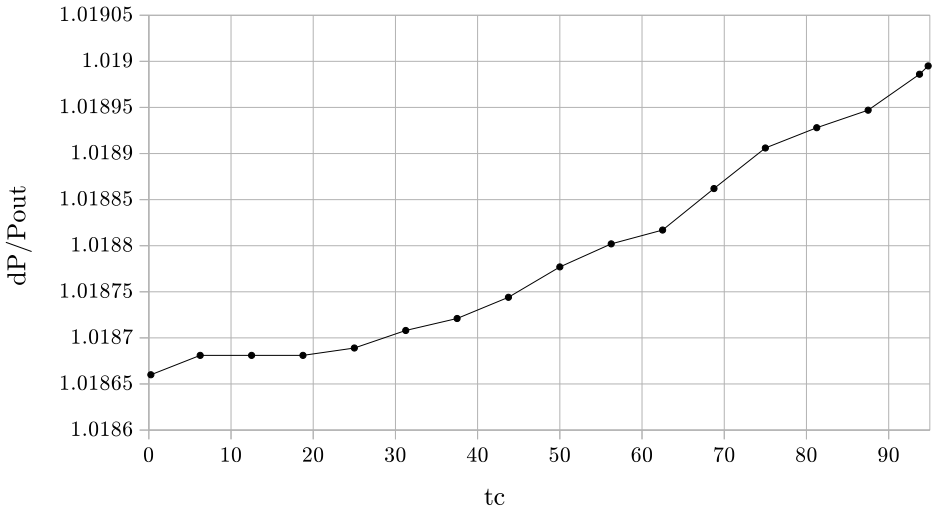

Figure 7.30: Pressure increase with time (soot deposition) (low porosity and low sticking probability).

Figure 7.31 presents a noticeably different trend to previous studies. After an initial rise in pressure there is little change. Partially this could be due to the slower deposition rate, however in this case the flow and thus deposition simple convects toward

other portions of the substrate.

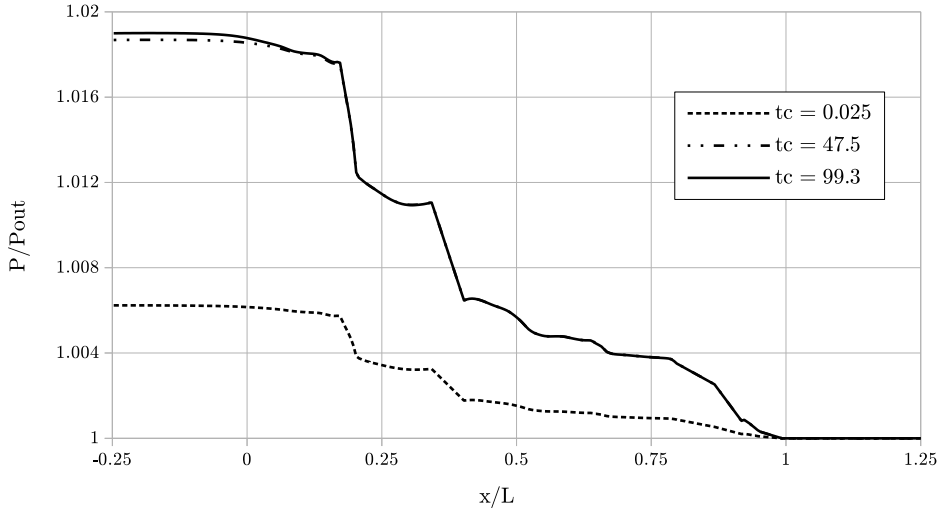

Figure 7.31: Pressure history along the centerline (low porosity and low sticking probability).

Centerline PM capture is displayed in figure 7.32. The centerline is arguably the least active of the tests, not surprisingly. While it is likely that the low sticking probability is responsible, it is also possible that flow diverts around this line. Later plots indicate this is partially the cause.

In figure 7.33 the process is even over the actual substrate entrance. This is a consequence of the low sticking probability, and the more even distribution of sequestration sites in a low porosity filter. In areas where there is a substantial break in the line of substrate nearest the inlet, the collection of PM proceeds deeper as expected. All of these features are clear in figure 7.34. As opposed to the previous tests, the development of "horns" is less visible as the process does not occur swiftly enough to form uneveness.

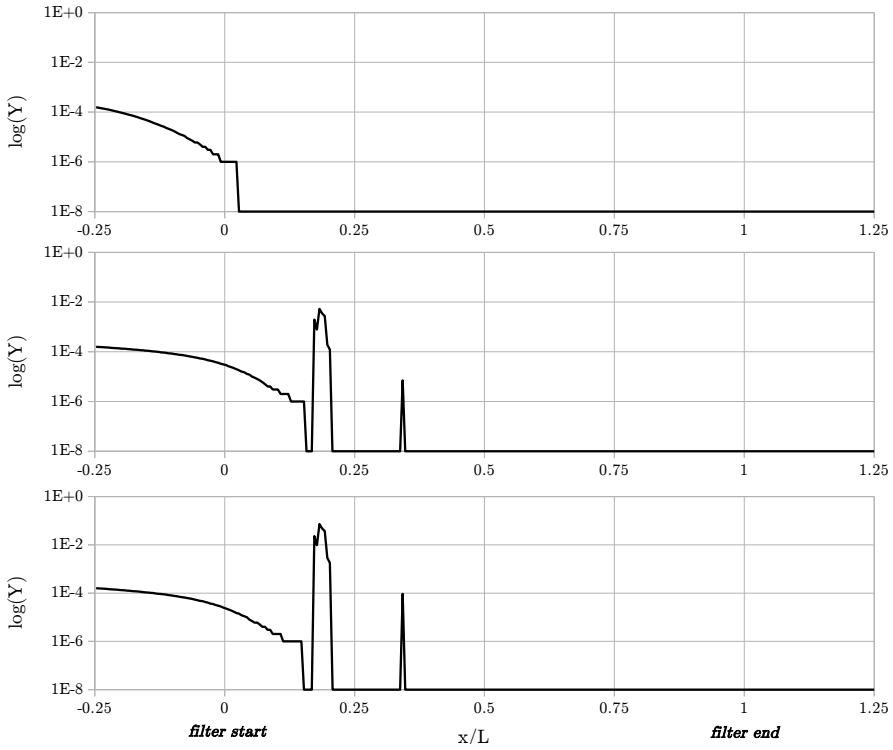

Figure 7.32: PM concentration at the y-center line at $t_c = 5$, 37.5, and 95 (low porosity and low sticking probability).

Filter loading percentage history in figure 7.35 shows some expected variation from previous studies. The initial delay in any loading is substantially extended, as expected from a lower deposition probability. When loading does initialize the growth is still roughly linear, but of course reaches a lower point. With further run time, the loading percentage would not only increase, but be more evenly distributed than higher sticking runs.

As a result of the slower deposition process, the flow paths change less frequently than past tests, and the velocity increases are more mild. It becomes substantially more challenging to find the variation between x-velocity fields in figure 7.36. However,

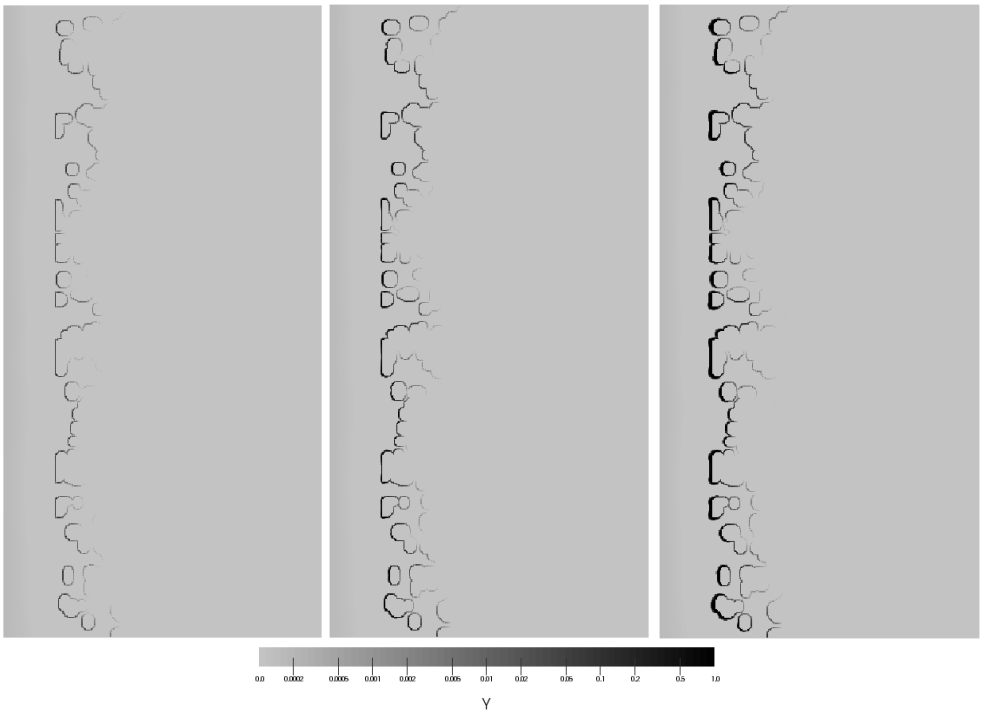

Figure 7.33: PM concentration at t_c = 30, 60, and 95 (low porosity and low sticking probability).

they exist in subtle ways, perhaps most evident near the top of the domain. In this particular scenario, the substrate still has a susbtantial capacity remaining and flow would not need to substantially divert to other areas of similar porosity.

Temperature at the centerline (see figure 7.37) follows a similar general pattern as the low porosity, high sticking probability simulation. Temperature quickly drops very low and stays low. Again, this is due to the large negative energy source term in the advection-diffusion equation combined with the low porosity providing substantial mass.

Temperature progression in the domain is displayed in figure 7.38. Heat is removed by

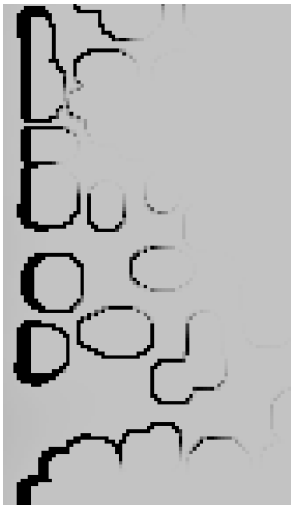

Figure 7.34: PM concentration closeup at $t_c = 95$ (low porosity and low sticking probability).

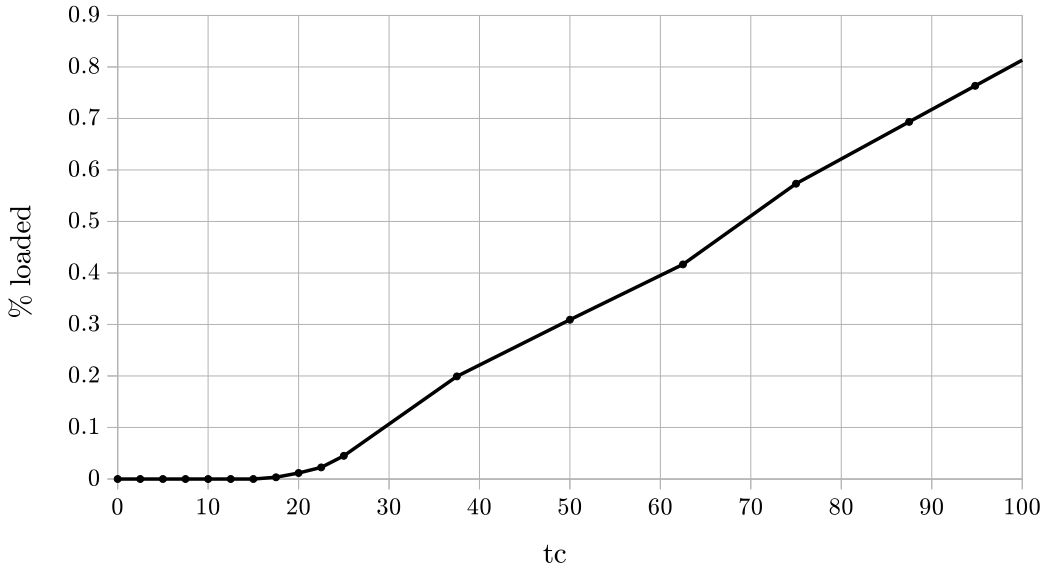

Figure 7.35: PM volumetric loading with time (low porosity and low sticking probability).

the substrate as iterations progress. The apparent "blotchiness" is due to substrate portions removing heat as warmer fluid is convected past. Higher temperatures are sustained deeper into the substrate where blockages aren't as near the inlet.

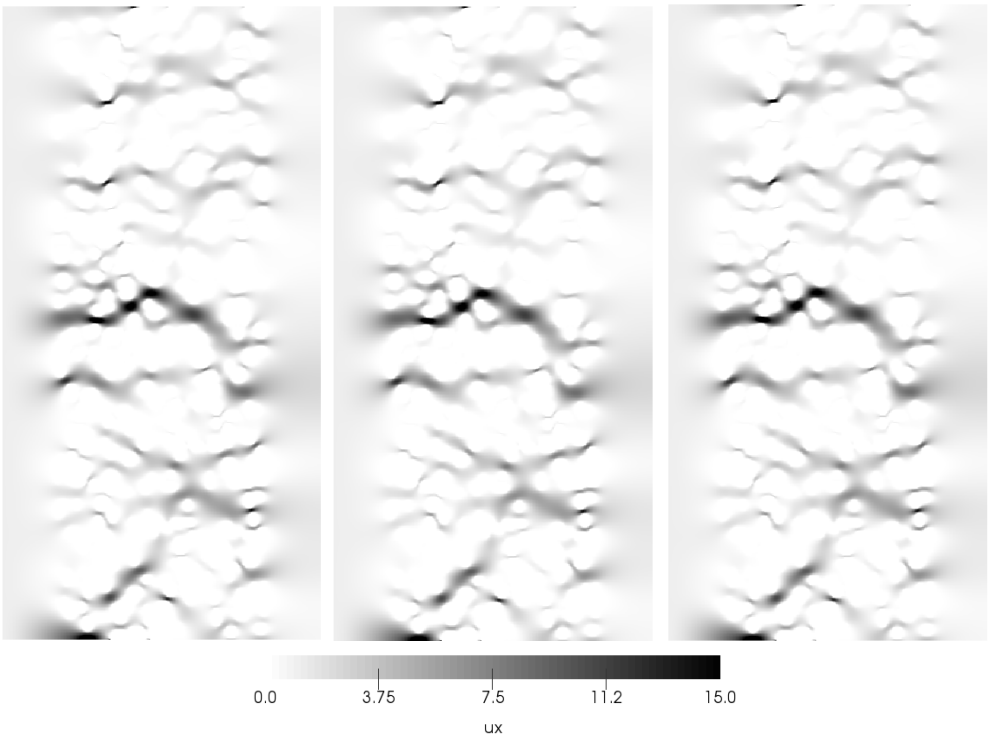

Figure 7.36: x-velocity at $t_c = 0.025$, 50, and 95 (low porosity and low sticking probability).

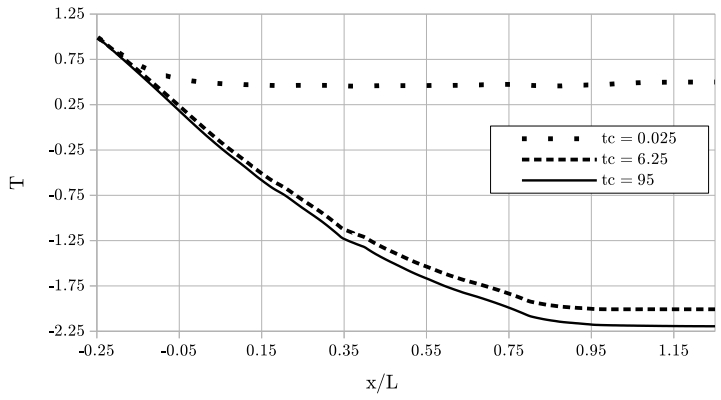

Figure 7.37: Temperature at the y-center line with time (low porosity and low sticking probability).

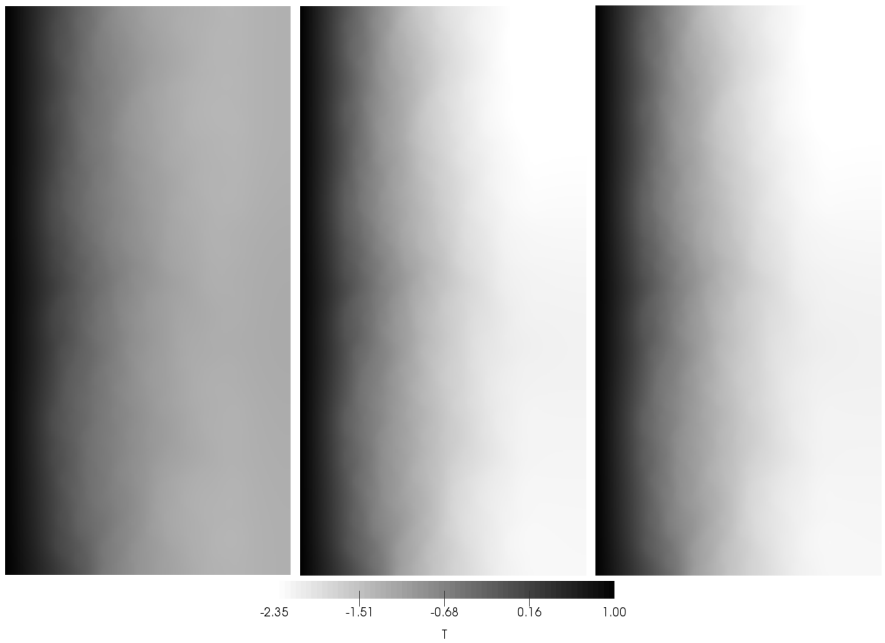

Figure 7.38: Temperature at $t_c = 2.5$, 25, and 95 (low porosity and low sticking probability).

Chapter 8

Conclusions

8.1 Contributions to the Incompressible Lattice Boltzmann Method and its Applications

Within the set of studies presented here, a definitive incompressible lattice Boltzmann equation was derived, and with it, several engineering and physics applications enhanced. Validation was achieved, and unique benefits were found through the simulation of basic laminar flows, complex turbulent flows, and multiphysics particulate matter filtration modeling. A better understanding of the mesoscale approach to mathematical modeling of these physical phenomena was also attained, departing from and adding to previous related literature. Specifically, the primary contributions

to the body of knowledge are:

- An ansatz procedure which defines the values in the equilibrium distribution function for an incompressible lattice Boltzmann equation with any valid velocity space discretization;
- Verification of direct numerical simulation and Vreman large eddy simulation for constant density flows with the incompressible lattice Boltzmann equation, compared with more traditional methods;
- A multiphysics code for particle transport and deposition, and conjugate heat transfer for low speed flows in porous media reliant on only one tuned parameter (for surface adhesion forces);
- A simple algorithm that generates verified 2D filter substrates to a dictated porosity, and measures their characteristics.

8.2 Summary of Findings

8.2.1 Incompressible Lattice Boltzmann Equation

While previous researchers have partially resolved the need for an incompressible lattice Boltzmann equation, the first major finding of this work was that

these answers were incomplete. Due to the rigor introduced in chapter 4, and subsequent comparative simulation tests, the D2Q9 and D3Q19 lattices require specific leading equilibrium distribution terms of $\{C - 5P/3c^2, P/3c^2, P/12c^2\}$ and $\{C - 2P/9c^2, P/54c^2, P/108c^2\}$, respectively, where C is a constant. The results are actually more generally applicable than these two cases, and the ansatz method which provides the previously stated rigor can be employed for any valid lattice discretization. Validation was mathematically provided by the Chapman-Enskog multiscale expansion, which recovers the incompressible Navier-Stokes equations instead of the compressible form in the low Mach limit. Several unique benefits were found in addition to the limit on density variation, such as greater convergence stability and speed.

In canonical flow cases featuring steady complex flow patterns, such as the lid driven cavity, and others featuring transient pressure bounds, such as Womersley flow, performance was found to be excellent. Specifically, data matched solutions from the incompressible Navier-Stokes equations. Additionally, results in several cases better met the expectations of an incompressible flow solver than previously researched methods, such as a pseudo-compressible lattice Boltzmann equation. Study of the previously published fully incompressible lattice Boltzmann equation showed that those leading equilibrium distribution terms often produce unstable and inaccurate results, and that the leading terms found here are essential. Derivation of a multiple relaxation time collision operator form extends these benefits.

8.2.2 Turbulent Transition

Simulation of incompressible flows by the standard, somewhat compressible, lattice Boltzmann equation inevitably introduced some error. One of the most prominent areas where this occurred was turbulent and transitional flow. To demonstrate the value of the multiple relaxation time incompressible lattice Boltzmann equation derived in this work, a thorough study on direct numerical simulation on a 2D canonical flow was conducted on a highly refined lattice. Comparison was made to existing literature utilizing the traditional Navier-Stokes equations, the standard lattice Boltzmann equation, and unique data analysis techniques such as proper orthogonal decomposition. In the laminar regime, center line velocity values were consistently within fractions of a percent to higher resolution simulations. At turbulent Reynolds numbers, the eddy structures found in other works were well replicated here. Most prominently, these methods predicted a first Hopf bifrucation to transience at a Reynolds number of 7,988, and transition at Reynolds number 13,063, both in excellent agreement with high resolution data and mathematical theory. These results showed that the definitive incompressible lattice Boltzmann equation is recommended when approaching turbulent transitional flow simulation with a mesoscopic methodology.

To provide further benefit demonstration in 3D, albeit without all turbulent scales resolved, a large eddy simulation case was performed, and compared to 2D results at

the center plane, as well as closed domain literature. A relatively new subgrid scale model was employed, authored by A.W. Vreman, to also test and recommend its capabilities when paired with the mesoscopic incompressible approach. This method provides transitional capabilities (unlike the standard Smagorinksy model) at relatively low cost (unlike the Dynamic Smagorinsky model). The pairing of the Vreman subgrid scale model with the incompressible lattice Boltzmann equation is recommended for constant density large eddy simulations.

8.2.3 Multiphysics Filtration

An application area which is often fundamentally incompressible is flow through porous media. The lattice Boltzmann method is a particularly promising tool for pore scale simulation due to simple bounce back boundary conditions, a regular and easy to manipulate meshless grid, ability to enter the mesoscale regime, and good scaling when parallelized. It also has the benefit of replacing 0D and 1D simluation techniques, which are reliant on large numbers of tuned parameters not universally valid, and do not provide an inspectable detailed report. Previous pore scale studies utilized the standard lattice Boltzmann equation or a pseudo-compressible form, as well as limiting assumptions on the Schmidt number and number of discrete velocities required for a conjugate heat transfer solver. These studies also utilized a physically scanned filter substrate geometry, which while accurate, can be a cumbersome task

when simplifications are acceptable, or design sweeps are of interest.

Since the first step in simulation is usually definition of the domain/geometry, a substrate generation algorithm was created in the C language. The code generates a random field of blockages of complex shapes with complex torturous flow paths based on a desired porosity. Verification that such an approach is valid was provided by studying Darcy's law, the Ergun equation, and the Nabovati correlation with the incompressible lattice Boltzmann equation as a flow solver. Under a variety of porosity and Reynolds number assignments, Darcy's law was repeatedly obeyed with an exponential and intrinsic relation between porosity and permeability. The relationship between friction factor and Reynolds number provided a tight fit across a broad range of filter characteristics to the experimental Ergun equation. The generated substrate also laid the groundwork for more complex simulation and modeling by being ready for conjugate heat transfer and interaction with multispecies flows.

Several lattice discretizations have historically been applied to non-isothermal incompressible heat transfer solutions. In the case of 2D, 9- and 4-velocity models. If a reduction in discrete velocities is valid, computational cost can be reduced. The case for a reduced number of discrete velocities is based on the linear nature of the advection-diffusion equation of the temperature transport form of the incompressible energy equation. As a result, recovery of the advection-diffusion equation through the

Chapman-Enskog expansion was performed in this work. Subsequent tests of complex convective flow and convective-conductive conjugate heat transfer demonstrated the equivalency of both numerical approximations. The 4-velocity model was then incorporated into the multiphysics filtration model.

Particulate matter transport and deposition methods present in literature were evaluated, and an Euler-Euler approach was chosen. Due to the utilization of a standard lattice Boltzmann equation, the diffusivity term could be directly assigned based on material properties. Previous studies, which utilized a similar approach, assigned the same value to momentum and mass diffusivities. The implementation of a Schmidt number basis for the calculation of the collision relaxation times provides additional fidelity to transport. With the Euler-Euler approach, individual particles are assumed to be small relative to the geometric dimensions and volume of flow. Thus, a concentration was tracked as opposed to individual or representative particle groupings. To account for the many atomic and molecular level mechanisms, a sticking probability was introduced, and rules for controlling growth of soot to replicate likely behavior applied.

A variety of sticking probabilities and porosities were studied to show expected results and patterns. These expected results included:

- Conservation of mass and momentum of all species and phases for the domain

as a whole;

- Conservation of energy for the domain;
- Increased speed of soot deposition with increased sticking probability and porosity;
- Decreased concentration at domain outlet with increasing porosity and sticking probability;
- Initial deposition occurring at substrate inlet and only later proceeding to deep bed filtration;
- Pressure at the inlet increases with increasing soot buildup;
- Maximum velocity in the domain increases with soot building (due to reduction in passage sizes).

All of these expectations were met, as well as more qualitative patterns such as collection zones as a function of Reynolds number and shape.

For a lattice Boltzmann filtration simulation involving heat transfer the results then support the following model choices:

- An incompressible flow solver;
- A 4-velocity energy solver;

- An Euler-Euler multispecies solver;
- A standard bounceback boundary condition for interaction with the substrate;
- A sticking probability parameter for deposition with local search rule to provide physical growths;
- A Schmidt number basis for determining collision relaxation time in the species transport solver.

8.3 Future Work

With the base capabilities for physics and engineering applications developed here, additional complexity can be added for relevant phenomena. Studies on sensitivity to model choices can provide further recommendations for use of the incompressible lattice Boltzmann equation.

Specific to the application of turbulence it would be valuable to clarify the role of higher discrete velocity lattices. While previous literature, and the findings of this study, indicate that only 15 velocity lattices are sufficient for 3D at the studied Re, there is an indication that stability and accuracy could benefit. Traditionally, 3D simulations utilize D3Q15, D3Q19, and D3Q27 models. Studies indicate that, while all are valid, the higher velocity models may improve the stability sufficiently to be

justifiable in certain cases [106]. In the case of LES turbulence modeling, this could mean a coarser mesh. This is of limited value since the accuracy degenerates with larger filter (mesh) sizes. However, it could be valuable to find the magnitude of the improved stability, reduced accuracy, and difference in computational cost.

To extend the capabilities of the filtration model, four main routes can be explored: extension to 3D, deposited soot erosion, regeneration within soot deposits, and validation exercises. The model of this study allows direct extension for all of these. Suggestions on implementation direction for each extension follow.

Substrates are not only fundamentally 3D, but flow in a third dimension changes the range of possible porosities. Below $\sim$50% porosity there are few, if any, connected flow passages in 2D. With a third dimension there is an additional direction flow may take, and with the potential for a "spherical" general shape, for these flow passages to open substantially. The substrate generation algorithm presented here is an excellent basis for extension to 3D. An additional spatial location for the z-direction can be easily dictated (with a nested for loop to assign placement), and the randomness of overlap and larger shapes will be retained. In place of the equation for an ellipse dictating size and shape through two random axes (minor and major), an ellipsoid equation can be used with a third random axis size. Since the shapes will mark a node in a discrete fashion as either solid or fluid, the result will be similarly ready to accept soot deposition and conjugate heat transfer.

Given physical filter scan images of a given porosity, it would be interesting to determine the fractal dimension for comparison to the algorithm presented here. As an example, using the Minkowski-Bouligand dimensional analysis for fractal geometry, the fractal dimension of a generated 80% porosity filter is calculated here at 1.55, and for a 50% porosity filter it is 1.72. In addition to the extensive analytical and empirical comparisons presented in this work, the additional comparison could be useful in moving to 3D confidently.

Due to a complex set of forces, both external and internal to the soot deposits, particulate matter may reenter the flow to deposit again later, or leave the domain. By introducing an "ejection probability" soot deposited to the variable "Y_2" in the filtration code can be re-injected to the free flowing species concentration "Y_1". All other rules on transport and deposition can be retained.

A further level of particulate deposition and erosion fidelity which should be incorporated in future work is dependency on local velocity and shear. In the present work a constant is utilized. In a faster moving flow, momentum can accelerate erosion of the deposited material. For particle capture, it would be expected that sticking would reduce with increased flow velocity due to increased inertia largely orthogonal to the substrate surfaces.

Catalytic filtration is frequently utilized to remove pollutants and particulate matter. It is another valuable addition the filter model developed here. Since particulate

matter is already transported and deposited, and conjugate heat transfer is present, the critical components to regeneration are available. Rules governing the alterations in temperature, and change in soot deposition layers are required. Additionally, more sophisticated treatment of the closed boundaries of the domain, currently simply adiabatic, would enhance overall thermal simulation and thus regeneration modeling.

Since the focus of this work was method development and exploration, work remains on conversion to real parameters and experimental tuning (probability sticking). Some recommended parameters are listed in appendix C based on best practices, previous studies, and the goals of diesel particulate filtration simulation.

All code development for this work has been performed in C with OpenMP as the parallelization paradigm. One limitation is that only the computational cores present on one compute node can be utilized for any given run. An alternative is MPI, which allows inter-node computation, and therefore potentially more cores per simulation run. The downside is that MPI is more complex to implement, and if there are a substantial number of simultaneous simulation runs to be conducted, utilizing more cores per run can cause a bottleneck. This is in fact the main reason OpenMP was utilized; when studying turbulence and soot deposition many different simulations with different parameters were running in parallel on different compute nodes, utilizing a large number of overall cores towards quicker completion of the project as a whole. Additionally, while lattice Boltzmann algorithms provide greater scalability

than traditional Navier-Stokes methods, there is still an asymptotic limit to increased parallelization of any given run (see chapter 3.4. However, MPI is listed here as future work for cases in which a specific set of simulation parameters in a single are of interest. Additional speedup can be gained by improving the C code developed and implemented here. Particularly in the filtration model, once a substantial amount of soot has stuck the time per iteration rises substantially. With the algorithm well defined and explored here, future refinement can be made in the direction of the solid/boundary search and assignment operations which follow particulate matter sequestration and solidification.

Bibliography

[1] Murdock, J.; Yang, S. *International Journal of Computational Engineering Research* **2016**, *6(12)*, 47–59.

[2] Murdock, J.; Yang, S. The Thirteenth International Conference for Mesoscopic Methods in Engineering and Science, Hamburg, Germany, 2016.

[3] Murdock, J.; Ickes, J.; Yang, S. *Advances in Applied Mathematics and Mechanics* **2017**, *9*, 1271–1288.

[4] Murdock, J.; Ibrahim, A.; Yang, S. *Accepted: ASME Journal of Fluids Engineering* **2017**.

[5] Laurendeau, N. M. *Statistical Thermodynamics: Fundamentals and Applications;* Cambridge University Press, 1 ed., 2005.

[6] Boltzmann, L. *Wiener Berichte* **1872**, *66*, 275–370.

[7] President Obama's statement on climate change. Obama, B. *White House Briefing Room*, `https://www.whitehouse.gov/climate-change`, **2015**.

[8] Slotnick, J.; Khodadoust, A.; Alonso, J.; Darmofal, D.; Gropp, W.; Lurie, E.; Mavriplis, D. *NASA/CR-2014-218178* **2014**.

[9] Suluksna, K.; Juntasaro, E. *International Journal of Heat and Fluid Flow* **2008**, *29*, 48–61.

[10] Bissett, E. J.; Shadman, F. *AIChE Journal* **1985**, *31*, 753–758.

[11] Konstandopoulos, A. G.; Johnson, J. H. *SAE Technical Paper* **1989**, *890405*.

[12] Premchand, K. *Development of a 1-D Catalyzed diesel particulate filter model for simulation of the performance and the oxidation of particulate matter and nitrogen oxides using passive oxidation and active regeneration engine experimental data* PhD thesis, Michigan Technological University, **2013**.

[13] White, F. M. *Viscous Fluid Flow;* McGraw-Hill Education: Columbus, OH, 3 ed., 2005.

[14] Anderson, J. D. *Computational Fluid Dynamics: The Basics with Applications;* McGraw-Hill Education: Columbus, OH, 1 ed., 1995.

[15] Langmuir, I. *Office of Scientific Research and Development* **1942**, *865*.

[16] Happel, J. *AIChe Journal* **1959**, *5*, 174–177.

[17] Kuwabara, S. *Journal of the Physical Society of Japan* **1959**.

[18] McNamara, G. R.; Zanetti, G. *Physical Review Letters* **1988**, *61*, 2332–2335.

[19] Gong, J.; Rutland, C. J. *Environmental Science & Technology* **2015**, *49*, 4963–70.

[20] He, X.; Doolen, G. D.; Clark, T. *Journal of Computational Physics* **2002**, *179*, 439–451.

[21] Zou, Q.; Hou, S.; Chen, S.; Doolen, G. D. *Journal of Statistical Physics* **1995**, *81*, 35–48.

[22] Lin, Z.; Fang, H. P.; Tao, R. B. *Physical Review E* **1996**, *54*, 6323–6330.

[23] Chen, Y.; Ohashi, H. *International Journal of Modern Physics C* **1997**, *8*, 793–803.

[24] He, X.; Luo, L. S. *Journal of Statistical Physics* **1997**, *88*, 927–944.

[25] Guo, Z.; Shi, B.; Wang, N. *Journal of Computational Physics* **2000**, *165*, 288–306.

[26] Banda, M. K.; Yong, W. A.; Klar, A. *Journal of Scientific Computing* **2006**, *27*, 2098–2111.

[27] Shi, B.; He, N.; Wang, N. *Progress in Computational Fluid Dynamics* **2005**, *5*, 50–64.

[28] Du, R.; Shi, B.; Chen, X. *Physics Letters A* **2006**, *359*, 564–572.

[29] Martinez, D. O.; Matthaeus, W. H.; Chen, S.; Montgomery, D. C. *Physics of Fluids* **1994**, *6*, 1285.

[30] Lammers, P.; Beronov, K.; Volkert, R.; Brenner, G.; Durst, F. *Computers & Fluids* **2006**, *35*, 1137–1153.

[31] Lallemand, P.; Luo, L. S. *Physical Review E* **2000**, *61*, 6546–6562.

[32] Yu, H.; Girimaji, S. S.; Luo, L.-S. *Journal of Computational Physics* **2005**, *209*, 599–616.

[33] Premnath, K. N.; Pattison, M. J.; Banerjee, S. *Fluid Dynamics Results* **2013**, *45*, 055510.

[34] Stiebler, M.; Freudiger, S.; Krafczyk, M.; Geier, M. In *Notes on Numerical Fluid Mechanics and Multidisciplinary Design;* Springer Science + Business Media, 2011; pages 283–295.

[35] Jain, K.; Roller, S.; Mardal, K. A. *Computers & Fluids* **2016**, *127*, 36–46.

[36] Ladd, A. J. C. *Journal of Fluid Mechanics* **1994**, *271*, 285.

[37] Gschaider, B. F.; Honeger, C. C.; Redl, C. E.; Leixnering, J. *International Journal of Multiscale Computational Engineering* **2006**, *4*, 221–232.

[38] Lantermann, U.; Hänel, D. *Computers & Fluids* **2006**, *36*, 407–422.

[39] Filippova, O.; Hanel, D. *Computers & Fluids* **1997**, *26*, 697–712.

[40] Hardy, J.; Pomeau, Y.; de Pazzis, O. *Physical Review Letters* **1973**, *31*, 276–279.

[41] Masselot, A.; Chopard, B. *Europhysics Letters* **1998**, *42*, 259–264.

[42] Dupuis, A.; Chopard, B. *Journal of Computational Physics* **2002**, *178*, 161–174.

[43] Yamamoto, K.; Ohori, S. *International Journal of Engine Research* **2012**, *14*, 333–340.

[44] Yamamoto, K.; Matsui, K. *Fibers* **2014**, *2*, 128–141.

[45] Murakami, S.; Kato, S.; Nagano, S.; Tanaka, S. *ASHRAE Transactions* **1992**, *98*, 82–97.

[46] Holmberg, S.; Chen, Q. *Indoor Air* **2003**, *13*, 200–204.

[47] Zhao, B.; Zhang, Z.; Li, X.; Huang, D. *ASHRAE Transactions* **2004**, *110*, 88–95.

[48] Gong, J. *Passive Ammonia SCR and Filtration Modeling for Fuel-Neutral Engine Aftertreatment Systems* PhD thesis, University of Wisconsin-Madison, **2014**.

[49] Guo, Z.; Shu, C. *Lattice Boltzmann Method and its Applications in Engineering;* World Scientific Publishing Co. Pte. Ltd.: Hackensack, NJ, 3 ed., 2013.

[50] Bartoloni, A.; Battista, C.; Cabasino, S.; Paolucci, P. S.; Pech, J.; Sarno, R.; Todesco, G. M.; Torelli, M.; Tross, W.; Vicini, P.; Benzi, R.; Cabibbo, N.; Massaioli, F.; Tripiccione, R. *International Journal of Modern Physics C* **1993**, *4*, 993–1006.

[51] Shan, X. *Physical Review E* **1997**, *55*, 2780–2788.

[52] Guo, Z.; Shi, B.; Zheng, C. *International Journal for Numerical Methods in Fluids* **2002**, *39*, 325–342.

[53] Jami, M.; Mezrhab, F.; Fontaine, J. P.; Bouzidi, M. *International Journal of Thermal Science* **2016**, *100*, 98–107.

[54] Wang, J.; Wang, M.; Li, Z. *International Journal of Thermal Science* **2007**, *46*, 228–234.

[55] Tarokh, A.; Mohamad, A. A.; Jiang, L. *Numerical Heat Transfer, Part A: Applications* **2013**, *63*, 159–178.

[56] Pan, C.; Luo, L. S.; Miller, C. T. *Computers & Fluids* **2006**, *35*, 898–909.

[57] Chen, L.; Fang, W.; Kang, Q.; Hyman, J. D.; Viswanathan, H. S.; Tao, W. Q. *Physical Review E* **2015**, *91*, 033004.

[58] Spaid, M. A.; Phelan, F. R. *Physics of Fluids* **1997**, *9*, 2468–2474.

[59] Martys, N. S. *Physics of Fluids* **2001**, *6*, 1807–1810.

[60] Manz, B.; Gladden, L. F.; Warren, P. B. *AIChE Journal* **1999**, *45*, 1845–1854.

[61] Succi, S.; Foti, E.; Higuera, F. *Europhysics Letters* **1989**, *10*, 433–438.

[62] Fattahi, E.; Waluga, C.; Wohlmuth, B.; Rude, U.; Manhart, M.; Helmig, R. *arXiv:1508.02960 [cs.CE]* **2015**.

[63] Muntean, G. G.; Rector, D.; Herling, D.; Lessor, D.; Khaleel, M. *SAE Technical Paper* **2003**, *2003-fl-46*.

[64] Kang, Q.; Lichtner, P.; Janecky, D. *Advances in Applied Mathematics and Mechanics* **2010**, *2*, 545–563.

[65] History of kinetic theory. Levermore, D. *University of Maryland Mathematics Department*, `https://www2.math.umd.edu/~lvrmr/History/`, **2001**.

[66] Bhatnagar, P. L.; Gross, M.; Krook, M. *Physical Review* **1954**, *94*, 511–525.

[67] Chapman, S.; Cowling, T. *The Mathematical Theory of Non-Uniform Gases;* Cambridge University Press: New York, NY, 3 ed., 1990.

[68] Zou, Q.; He, X. *Physics of Fluids* **1997**, *9*, 1591–1598.

[69] Chen, S.; Martinez, D.; Mei, R. *Physics of Fluids* **1996**, *8*, 2527–2531.

[70] d'Humieres, D. *Progress in Aeronautics and Astronautics* **1992**, *159*, 450–458.

[71] d'Humieres, D.; Ginzburg, I.; Krafczyk, M. *Philosophical Transactions of the Royal Society of London A* **2002**, *360*, 437–451.

[72] Bouzidi, M.; d'Humieres, D.; Lallemand, P.; Luo, L. S. *Journal of Computational Physics* **2001**, *172*, 704–717.

[73] Brogioli, D.; Vailati, A. *Physical Review E* **2001**, *63*, 012105.

[74] Wilcox, D. C. *Turbulence Modeling for CFD;* Anaheim: DCW Industries, 2 ed., 1998.

[75] Pasquale, D. D.; Rona, A.; Garrett, S. J. *39th AIAA Fluid Dynamics Conference* **2009**, *3812*, 1–10.

[76] Kolmogorov, A. N. *Proceedings of the USSR Academy of Sciences* **1941**, *32*, 16–18.

[77] Pope, S. B. *Turbulent Flows;* Cambridge University Press, 1 ed., 2000.

[78] Peng, Y.; Shiau, Y.; Hwang, R. R. *Computers & Fluids* **2003**, *32*, 337–352.

[79] Poliashenko, M.; Aidun, C. K. *Journal of Computational Physics* **1995**, *121*, 246–260.

[80] Cazemier, W.; Verstappen, R. W.; Veldman, A. E. *Physics of Fluids* **1998**, *10*, 1685–1699.

[81] Bruneau, C.; Saad, M. *Computers & Fluids* **2006**, *35*, 704–717.

[82] Vreman, A. W. *Physics of Fluids* **2004**, *16*, 3670–3681.

[83] Darcy, H. *Les Fontaines Publiques de la Ville de Dijon;* 1856.

[84] Nabovati, A.; Llewellin, E.; Sousa, A. *Composites: Part A* **2009**, *40*, 860–869.

[85] Bird, R.; Stewart, W.; Lightfoot, E. *Transport Phenomena;* John Wiley & Sons, Inc.: New York, NY, 2 ed., 2002.

[86] Aruoba, S. B.; Fernandez-Villaverde, J. *Journal of Economic Dynamics and Control* **2015**, *58*, 265–273.

[87] On Fair Comparison between CPU and GPU. S. Han.; EECS Dept., Berkeley, **2013**.

[88] Can STAR-CCM+ take advantage of GPU computing? S. Feldman.; Siemens PLM (CD-adapco), **2015**.

[89] Qian, Y. H.; d'Humieres, D.; Lallemand, P. *Europhysics Letters* **1992**, *17*, 479–484.

[90] He, X.; Zou, Q.; Luo, L.; Dembo, M. *Journal of Statistical Physics* **1997**, *87*, 115–123.

[91] Meng, J.; Zhang, Y. *Journal of Computational Physics* **2011**, *230*, 835–849.

[92] Guo, Z.; Zhao, T.; Shi, Y. *Physical Review E* **2004**, *70*, 066706.

[93] Marchi, C.; Suero, R.; Araki, L. *Journal of the Brazilian Society of Mechanical Science & Engineering* **2009**, *31*, 186–198.

[94] Womersley, J. *Journal of Physiology* **1955**, *127*, 553–563.

[95] Erturk, E. *Computers & Fluids* **2008**, *37*, 633–655.

[96] Wong, K. L.; Baker, A. J. *International Journal for Numerical Methods in Fluids* **2002**, *38*, 99–123.

[97] Anupindi, K.; Lai, W.; Frankel, S. *Computers & Fluids* **2015**, *92*, 7–21.

[98] Burggraf, O. *Journal of Fluid Mechanics* **1966**, *24*, 113–151.

[99] Ghia, U.; Ghia, K.; Shin, C. *Journal of Computational Physics* **1982**, *48*, 387–411.

[100] Hou, S.; Zou, Q.; chen, S.; Doolen, G.; Cogley, A. *Journal of Computational Physics* **1995**, *118*, 329–347.

[101] Marie, S.; Ricot, D.; Sagaut, P. *Journal of Computational Physics* **2008**, *228*, 1056–1070.

[102] Wang, R.; Fang, H. *Communications in Theoretical Physics* **2000**, *35*, 593–596.

[103] Li, J.; Wang, Z. *Mathematical Problems in Engineering* **2010**, *2010*, 724578.

[104] Zhang, C.; Cheng, Y.; Huang, S.; Wu, J. *Advances in Applied Mathematics and Mechanics* **2016**, *8*, 37–51.

[105] Zhang, W.; Shi, B.; Wang, Y. *Computers & Mathematics with Applications* **2015**, *69*.

[106] Kruger, T.; Kusumaatmaja, H.; Kuzmin, A.; Shardt, O.; Silva, G.; Viggen, E. *The Lattice Boltzmann Method: Principles and Practice;* Springer International Publishing: Switzerland, 1 ed., 2017.

[107] Bear, J. *Dynamics of Fluids in Porous Media;* Dover Publications: Dover, NY, 1972.

[108] Whitaker, S. *Transport in Porous Media* **1986**, *1*, 3–25.

[109] Elkatatny, S.; Mahmoud, M.; Nasr-El-Din, H. *ASME Journal of Engery Resources Technology* **2013**, *135*, 042201–042201–9.

[110] Pilotti, M. *Transport in Porous Media* **1998**, *33*, 257–278.

[111] Maier, R.; Kroll, D.; Benard, R. *Physics of Fluids* **2000**, *12*, 2065–2079.

[112] Madadi, M.; Sahimi, M. *Physical Review E* **2003**, *67*, 026309.

[113] Zhang, H.; Ge, X.; Ye, H. *Journal of Physics D* **2006**, *39*, 220–226.

[114] Wellein, G.; Lammers, P. *Proceedings of the 2005 International Conference on Parallel Computational Fluid Dynamics* **2006**, pages 31–40.

[115] Hudong, C.; Chen, S.; Matthaeus, W. *Physical Review A* **1992**, *45*, R5339.

[116] Yuan, P.; Schaefer, L. *ASME Journal of Fluids Engineering* **2005**, *128*, 151–156.

[117] Karani, H.; Huber, C. *Physical Review E* **2015**, *91*, 023304.

[118] Inamuro, T.; Yoshino, M.; Inoue, H.; Mizuno, R.; Ogino, F. *Journal of Computational Physics* **2002**, *179*, 201–215.

[119] Koponen, A. *Physical Review Letters* **1998**, *80*.

[120] Jackson, G.; James, D. *Canadian Journal of Chemical Engineering* **1986**, *64*, 364–374.

[121] Dulien, F. *Porous Media: Fluid Transport and Pore Structure;* Academic Press, Inc.: New York, NY, 1979.

[122] Hutten, I. *Handbook of Nonwoven Filter Media;* Butterworth-Heinemann: Burlington, MA, 2007.

[123] Gebart, B. *Journal of Composite Materials* **1992**, *26*, 1100–1133.

[124] Brinkmann, H. *Flow, Turbulence and Combustion* **1949**, *1*.

[125] Delaney, D.; Weaire, S.; Murphy, S. *Philosophical Magazine Letters* **2005**, *85*, 89–96.

[126] Buick, J.; Greated, C. *Physical Review E* **2000**, *61*, 5307–5320.

[127] Flagan, R. C.; Seinfeld, J. *Fundamentals of air pollution engineering;* Prentice-Hall, Inc.: Englewood Cliffs, NJ, 1 ed., 1988.

Appendix A

iLBE Derivations

A.1 Chapman-Enskog Expansion for the iLBE

From [89] we have some important relationships based on the Knudsen number (Kn)

$$\epsilon \equiv Kn \tag{A.1}$$

Scaling x,

$$\epsilon^{-1} x_1 \Rightarrow \frac{\partial}{\partial x} = \epsilon \frac{\partial}{\partial x_1}, \tag{A.2}$$

and for the same order of magnitude of ϵ, scaling t through the equation

$$\frac{\partial}{\partial t} = \epsilon \frac{\partial}{\partial t_1} + \epsilon^2 \frac{\partial}{\partial t_2}. \tag{A.3}$$

The slower diffusion time scale is t_2 and the faster convection time scale is t_1.

Performing the perterbation expansion of f_a in terms of ϵ,

$$f_a(\boldsymbol{x}, t) = f_a^{(0)}(\boldsymbol{x}, t) + \epsilon f_a^{(1)}(\boldsymbol{x}, t) + \epsilon^2 f_a^{(2)}(\boldsymbol{x}, t) + \mathcal{O}(\epsilon^3), \;\; f_a^{(0)} = f_a^{eq}. \tag{A.4}$$

Combining the Taylor Series Expansion of f_a with the LBE,

$$\begin{aligned} \frac{1}{\lambda}(f_a^{(0)} - f_a) = & \left(\frac{\partial}{\partial t} + \nabla_{\boldsymbol{x}} \cdot c\boldsymbol{e}_a \right) f_a \\ & + \frac{\Delta t}{2} \left[\frac{\partial}{\partial t} \left(\frac{\partial}{\partial t} \right) + 2 \frac{\partial}{\partial t} (\nabla_{\boldsymbol{x}} \cdot c\boldsymbol{e}_a) + (\nabla_{\boldsymbol{x}} \nabla_{\boldsymbol{x}}) : (c\boldsymbol{e}_a c\boldsymbol{e}_a) \right] f_a \\ & + \mathcal{O}(\Delta t^2), \end{aligned} \tag{A.5}$$

with the aforementioned expansions utilized we obtain

$$\begin{aligned}\frac{1}{\lambda}(f_a^{(0)} - f_a) = &\left(\epsilon\frac{\partial f_a}{\partial t_1} + \epsilon^2\frac{\partial f_a}{\partial t_2}\right) + \epsilon(\nabla_{x_1}\cdot c\boldsymbol{e}_a)f_a \\ &+ \frac{\Delta t}{2}\epsilon^2\left[\frac{\partial^2 f_a}{\partial t_1^2} + 2\frac{\partial}{\partial t_1}(\nabla_{x_1}\cdot c\boldsymbol{e}_a)f_a + (\nabla_{\boldsymbol{x}}\nabla_{\boldsymbol{x}}) : [(c\boldsymbol{e}_a c\boldsymbol{e}_a)f_a]\right] \\ &+ \frac{\Delta t}{2}\epsilon^3\left[2\frac{\partial}{\partial t_1}\frac{\partial f_a}{\partial t_2} + 2\frac{\partial}{\partial t_2}(\nabla_{x_1}\cdot c\boldsymbol{e}_a)f_a\right] + \frac{\Delta t}{2}\epsilon^4\left(\frac{\partial^2 f_a}{\partial t_2^2}\right) \\ &+ \mathcal{O}(\Delta t^2).\end{aligned} \tag{A.6}$$

We retain 1^{st} and 2^{nd} order terms of ϵ for the incompressible case.

Considering Terms of 1^{st} order for mass,

$$\begin{aligned}-\frac{1}{\lambda}f_a^{(1)} &= \frac{\partial f_a^{(0)}}{\partial t_1} + (\nabla_{x_1}\cdot c\boldsymbol{e}_a)f_a^{(0)} \Rightarrow \\ -\frac{1}{\lambda}\sum_a f_a^{(1)} &= \frac{\partial\left(\sum_a f_a^{(0)}\right)}{\partial t_1} + \nabla_{x_1}\cdot\left(\sum_a c\boldsymbol{e}_a f_a^{(0)}\right),\end{aligned} \tag{A.7}$$

and with one of the bases (4.12) for our incompressible scheme,

$$\sum_{a=0}^{8} f_a^{eq} = \sum_{a=0}^{8} f_a = 1 \tag{A.8}$$

we arrive at

$$\nabla_{x_1} \cdot \boldsymbol{u} = 0. \tag{A.9}$$

Looking at 1^{st} order for momentum,

$$\begin{aligned} -\frac{1}{\lambda} c\boldsymbol{e}_a f_a^{(1)} &= \frac{\partial c\boldsymbol{e}_a f_a^{(0)}}{\partial t_1} + \nabla_{x_1} \cdot c\boldsymbol{e}_a c\boldsymbol{e}_a f_a^{(0)} \Rightarrow \\ -\frac{1}{\lambda} \sum_a c\boldsymbol{e}_a f_a^{(1)} &= \frac{\partial \left(\sum_a c\boldsymbol{e}_a f_a^{(0)} \right)}{\partial t_1} + \nabla_{x_1} \cdot \left(\sum_a c\boldsymbol{e}_a f_a^{(0)} \right), \end{aligned} \tag{A.10}$$

and with the additional basis (4.13) for our incompressible scheme

$$\sum_{a=0}^{8} c\boldsymbol{e}_a f_a^{eq} = \sum_{a=0}^{8} c\boldsymbol{e}_a f_a = \boldsymbol{u}, \tag{A.11}$$

we arrive at

$$\frac{\partial \boldsymbol{u}}{\partial t_1} + \nabla_{x_1} \cdot \Pi^{(0)} = 0, \tag{A.12}$$

$$\Pi^{(0)}(0^{th} \text{ order momentum flux tensor}),\ \ \Pi^{(0)} = \sum_a c\boldsymbol{e}_a c\boldsymbol{e}_a f_a^{(0)} = \frac{P}{\rho_0}\boldsymbol{I} + \boldsymbol{uu} \quad \text{(A.13)}$$

Now looking at 2^{nd} order terms of ϵ for the dissipative terms in the Navier-Stokes equation, for mass conservation,

$$\begin{aligned} -\frac{1}{\lambda}\sum_a f_a^{(2)} = &\left[\frac{\partial}{\partial t_1}\left(\sum_a f_a^{(1)}\right) + \nabla_{x_1}\cdot\left(\sum_a c\boldsymbol{e}_a f_a^{(1)}\right)\right] \\ &+ \frac{\partial}{\partial t_2}\left(\sum_a f_a^{(0)}\right) \\ &+ \frac{\Delta t}{2}\left[\frac{\partial^2}{\partial t_1^2}\left(\sum_a f_a^{(0)}\right) + 2\frac{\partial}{\partial t_1}\left(\nabla_{x_1}\cdot\left(\sum_a c\boldsymbol{e}_a f_a^{(0)}\right)\right)\right] \\ &+ \frac{\Delta t}{2}\left[(\nabla_{x_1}\nabla_{x_1}) : \left[\sum_a (c\boldsymbol{e}_a c\boldsymbol{e}_a) f_a^{(0)}\right]\right] \end{aligned} \quad \text{(A.14)}$$

Noting that

$$\sum_a f_a^{(G)} = 0 \ \text{ and } \ \sum_a \boldsymbol{e}_a f_a^{(G)} = 0,\ \ G > 0, \quad \text{(A.15)}$$

we reduce the 2^{nd} order terms of ϵ to

$$\frac{\Delta t}{2}\left[2\frac{\partial}{\partial t_1}\left(\nabla_{x_1}\cdot\sum_a c\boldsymbol{e}_a f_a^{(0)}\right)\right]=\Delta t\frac{\partial}{\partial t_1}\left[\nabla_{x_1}\cdot\boldsymbol{u}\right], \tag{A.16}$$

$$\frac{\Delta t}{2}(\nabla_{x_1}\nabla_{x_1}):\left[\sum_a(c\boldsymbol{e}_a c\boldsymbol{e}_a)f_a^{(0)}\right]=\frac{\Delta t}{2}\nabla_{x_1}\cdot\left(-\frac{\partial\boldsymbol{u}}{\partial t_1}\right). \tag{A.17}$$

Knowing that $\nabla_{x_1}\cdot\boldsymbol{u}=\partial(\nabla_{x_1}\cdot\boldsymbol{u})=0$ from above, and using (4.13) we obtain no contribution to the mass equation.

For the contribution to the momentum equation we have

$$-\frac{1}{\lambda}\sum_a c\boldsymbol{e}_a f_a^{(2)}=\frac{\partial}{\partial t_2}\left(\sum_a c\boldsymbol{e}_a f_a^{(0)}\right)+\left(1-\frac{\Delta t}{2\lambda}\right)\left[\frac{\partial}{\partial t_1}\left(\sum_a c\boldsymbol{e}_a f_a^{(1)}\right)+\nabla_{x_1}\cdot\Pi^{(1)}\right] \tag{A.18}$$

And similarly to the 0^{th} order momentum flux tensor, $\Pi^{(1)}$ is the 1^{st} order momentum flux tensor which, for small Ma, can be expanded as

$$\begin{aligned}\Pi^{(1)}=\sum_a c^2\boldsymbol{e}_a\boldsymbol{e}_a f_a^{(1)}\approx-\lambda\left(\frac{c^2}{3}\right)\left[\nabla_{x_1}\boldsymbol{u}+(\nabla_{x_1}\boldsymbol{u})^T\right]\Rightarrow\\ 0=\frac{\partial\boldsymbol{u}}{\partial t_2}-\nu\left[\nabla_{x_1}\cdot\left[\nabla_{x_1}\boldsymbol{u}+(\nabla_{x_1}\boldsymbol{u})^T\right]\right],\ \ \nu=\left(\frac{c^2}{3}\right)\left(\tau-\frac{1}{2}\right)\delta t\end{aligned} \tag{A.19}$$

Studying terms of $\mathcal{O}(\epsilon)$, and reversing our scaling of x, we recover the incompressible mass conservation equation

$$\nabla \cdot \boldsymbol{u} = 0 \tag{A.20}$$

Studying terms of $\mathcal{O}(\epsilon)$ and $\mathcal{O}(\epsilon^2)$, recalling our momentum flux tensors, and reversing the scaling of t we recover the incompressible momentum equation

$$\begin{aligned} \frac{\partial \boldsymbol{u}}{\partial t} + \nabla \cdot \Pi^{(0)} &= \nu \nabla \cdot \Pi^{(1)} \Rightarrow \\ \frac{\partial \boldsymbol{u}}{\partial t} + \nabla \cdot (\boldsymbol{u}\boldsymbol{u}) &= -\frac{1}{\rho_0} \nabla p + \nu \nabla^2 \boldsymbol{u} \end{aligned} \tag{A.21}$$

A.2 MRT-iLBE

A.2.1 D2Q9

Starting from the SRT-iLBE

$$\boldsymbol{f}(\boldsymbol{x}+\boldsymbol{c}_i\delta t, t+\delta t) - \boldsymbol{f}(\boldsymbol{x},t) = -\frac{1}{\tau}(\boldsymbol{f}(\boldsymbol{x},t) - \boldsymbol{f}^{eq}(\boldsymbol{x},t)) \tag{A.22}$$

and introducing the identity matrix $\boldsymbol{I} = \boldsymbol{M}^{-1}\boldsymbol{M}$, the collision step is modified as

$$\begin{aligned}\boldsymbol{f}(\boldsymbol{x}+\boldsymbol{c}_i\delta t, t+\delta t) - \boldsymbol{f}(\boldsymbol{x},t) &= -\boldsymbol{M}^{-1}\boldsymbol{M}\frac{1}{\tau}(\boldsymbol{f}(\boldsymbol{x},t) - \boldsymbol{f}^{eq}(\boldsymbol{x},t)) \\ &= -\boldsymbol{M}^{-1}\frac{1}{\tau}\boldsymbol{I}(\boldsymbol{M}\boldsymbol{f}(\boldsymbol{x},t) - \boldsymbol{M}\boldsymbol{f}^{eq}(\boldsymbol{x},t)) \\ &= -\boldsymbol{M}^{-1}\boldsymbol{S}(\boldsymbol{m}(\boldsymbol{x},t) - \boldsymbol{m}^{eq}(\boldsymbol{x},t)),\end{aligned} \tag{A.23}$$

where $\boldsymbol{S} = \frac{1}{\tau}\boldsymbol{I}$, a diagonal matrix of inverse relaxation times. $\boldsymbol{m}$ and $\boldsymbol{m}^{eq}$ are the moment and equilibrium moment vectors defined as $\boldsymbol{m} = \boldsymbol{M}\boldsymbol{f}$ and $\boldsymbol{m}^{eq} = \boldsymbol{M}\boldsymbol{f}^{eq}$, respectively, and $\boldsymbol{M}$ is the transformation matrix for mapping velocity to moment space. To provide a unique relaxation time for each moment, $\boldsymbol{S}$ is further defined as $\text{diag}(\frac{1}{\tau_0}, ..., \frac{1}{\tau_{q-1}})$.

Moment vectors refer to velocity moments of the iLBE distribution functions, some being easy to identify from equations 4.12 and 4.13, such as the 0^{th} and 1^{st}-order moments

$$\begin{aligned} \rho_0 &= \sum_i f_i = 1 \\ j_x &= \sum_i c_{ix} f_i = u_x \\ j_y &= \sum_i c_{iy} f_i = u_y, \end{aligned} \tag{A.24}$$

density, x-mass flux, and y-mass flux, respectively. In each case this produces a vector of i elements, making up a row of the transformation matrix $\boldsymbol{M}$. Expanded, they are

$$\begin{aligned} \rho_0 &= (1,1,1,1,1,1,1,1,1) \\ j_x &= (0,1,0,-1,0,1,-1,-1,1) \\ j_y &= (0,0,1,0,-1,1,1,-1,-1). \end{aligned} \tag{A.25}$$

The remaining six are produced from the polynomials $c_{ix}^m c_{iy}^n$, $m, n \in \{0,1,2\}$. These moments are selected to be related to other macroscopic properties, and are summarized as

$$\boldsymbol{m} = (\rho_0, e, e^2, j_x, q_x, j_y, q_y, P_{xx}, P_{xy})^T, \tag{A.26}$$

where e is related to energy, q is related to energy flux, and P is related to the diagonal and non-diagonal elements of the stress tensor. For example, $m_{P_{xy}} = m_8 =$

$(0,0,0,0,0,1,-1,1,-1) = u_x u_y$.

These vectors (referred to as $\boldsymbol{v}_i$) are next orthogonalized (referred to as $\boldsymbol{u}_i$) via the Gram-Schmidt procedure

$$\begin{aligned}
\boldsymbol{u}_0 &= \boldsymbol{v}_0 \\
\boldsymbol{u}_1 &= \boldsymbol{v}_1 - \boldsymbol{u}_0 \frac{\boldsymbol{u}_0 \cdot \boldsymbol{v}_1}{\boldsymbol{u}_0 \cdot \boldsymbol{u}_0} \\
\boldsymbol{u}_2 &= \boldsymbol{v}_2 - \boldsymbol{u}_0 \frac{\boldsymbol{u}_0 \cdot \boldsymbol{v}_2}{\boldsymbol{u}_0 \cdot \boldsymbol{u}_0} - \boldsymbol{u}_1 \frac{\boldsymbol{u}_1 \cdot \boldsymbol{v}_2}{\boldsymbol{u}_1 \cdot \boldsymbol{u}_1} \\
&\cdots \\
\boldsymbol{u}_{q-1} &= \boldsymbol{v}_{q-1} - \sum_{i=0}^{q-2} \boldsymbol{u}_i \frac{\boldsymbol{u}_i \cdot \boldsymbol{v}_{q-1}}{\boldsymbol{u}_i \cdot \boldsymbol{u}_i}
\end{aligned} \tag{A.27}$$

yielding the final form of the transformation matrix

$$\boldsymbol{M} = \begin{bmatrix} 1 & 1 & 1 & 1 & 1 & 1 & 1 & 1 & 1 \\ -4 & -1 & -1 & -1 & -1 & 2 & 2 & 2 & 2 \\ 4 & -2 & -2 & -2 & -2 & 1 & 1 & 1 & 1 \\ 0 & 1 & 0 & -1 & 0 & 1 & -1 & -1 & 1 \\ 0 & -2 & 0 & 2 & 0 & 1 & -1 & -1 & 1 \\ 0 & 0 & 1 & 0 & -1 & 1 & 1 & -1 & -1 \\ 0 & 0 & -2 & 0 & 2 & 1 & 1 & -1 & -1 \\ 0 & 1 & -1 & 1 & -1 & 0 & 0 & 0 & 0 \\ 0 & 0 & 0 & 0 & 0 & 1 & -1 & 1 & -1 \end{bmatrix}, \tag{A.28}$$

Recalling that $\boldsymbol{m}^{eq} = \boldsymbol{M}\boldsymbol{f}^{eq}$, the resultant equilibrium moments of the transformation are

$$\begin{aligned} m_0^{eq} &= 1 & m_3^{eq} &= u_x & m_6^{eq} &= -u_y \\ m_1^{eq} &= 6P + 3u^2 & m_4^{eq} &= -u_x & m_7^{eq} &= u^2 \\ m_2^{eq} &= -9P - 3u^2 & m_5^{eq} &= u_y & m_8^{eq} &= u_x u_y. \end{aligned} \tag{A.29}$$

To obtain the matrix for mapping the moment space back to velocity space, $\boldsymbol{M}$ is inverted,

$$\boldsymbol{M}^{-1} = \begin{bmatrix} \frac{1}{9} & -\frac{1}{9} & \frac{1}{9} & 0 & 0 & 0 & 0 & 0 & 0 \\ \frac{1}{9} & -\frac{1}{36} & -\frac{1}{18} & \frac{1}{6} & -\frac{1}{6} & 0 & 0 & \frac{1}{4} & 0 \\ \frac{1}{9} & -\frac{1}{36} & -\frac{1}{18} & 0 & 0 & \frac{1}{6} & -\frac{1}{6} & -\frac{1}{4} & 0 \\ \frac{1}{9} & -\frac{1}{36} & -\frac{1}{18} & -\frac{1}{6} & \frac{1}{6} & 0 & 0 & \frac{1}{4} & 0 \\ \frac{1}{9} & -\frac{1}{36} & -\frac{1}{18} & 0 & 0 & -\frac{1}{6} & \frac{1}{6} & -\frac{1}{4} & 0 \\ \frac{1}{9} & \frac{1}{18} & \frac{1}{36} & \frac{1}{6} & \frac{1}{12} & \frac{1}{6} & \frac{1}{12} & 0 & \frac{1}{4} \\ \frac{1}{9} & \frac{1}{18} & \frac{1}{36} & -\frac{1}{6} & -\frac{1}{12} & \frac{1}{6} & \frac{1}{12} & 0 & -\frac{1}{4} \\ \frac{1}{9} & \frac{1}{18} & \frac{1}{36} & -\frac{1}{6} & -\frac{1}{12} & -\frac{1}{6} & -\frac{1}{12} & 0 & \frac{1}{4} \\ \frac{1}{9} & \frac{1}{18} & \frac{1}{36} & \frac{1}{6} & \frac{1}{12} & -\frac{1}{6} & -\frac{1}{12} & 0 & -\frac{1}{4} \end{bmatrix}, \tag{A.30}$$

A symbolic mathematical package is very useful for these large calculations.

The relaxation time matrix is the remaining undefined component of the MRT operation. Certain elements must have exact values (S_7 and S_8 for viscosity), some are of no consequence (S_0, S_3, S_5) since the moment space collision yields zero (i.e. $S_3(m_3 - m_3^{eq})) = S_3(u_x - u_x)) = 0$), and others can be chosen to enhance stability as long as they are in the range (0,2). Here the values are chosen to be

$$\boldsymbol{S} = \left[1, 1.1, 1, 1, 1.2, 1, 1.2, \frac{1}{\tau}, \frac{1}{\tau}\right], \quad \nu = \frac{1}{3}\left(\tau - \frac{1}{2}\right). \tag{A.31}$$

A.2.2 D3Q15

Starting from the same point as the D2Q9 MRT derivation (equation A.22), followed by the conversion to moment space of the collision term (equation A.23), the moments are built from the polynomials $c_{ix}^m c_{iy}^n c_{iz}^l$, $m, n, l \in \{0, 1, 2\}$. Several are the familiar macroscopic moments such as ρ_0, or related to recognizable properties such as diagonal terms of the stress tensor. To accommodate the 15 distribution functions of the D3Q15 lattice, additional relevant moments are required. They are

$$\boldsymbol{m} = (\rho_0, e, e^2, j_x, q_x, j_y, q_y, j_z, q_z, 3P_{xx}, P_{ww}, P_{xy}, P_{yz}, P_{xz}, t_{xyz})^T. \tag{A.32}$$

The z-dimension is added to some elements of $\boldsymbol{m}$, expounded in section A.2.1. A new moment, t_{xyz} is related to the 3D stress tensor, and is defined as

$$t_{xyz} = c_{ix} c_{iy} c_{iz} = (0, 0, 0, 0, 0, 0, 0, 1, -1, -1, 1, -1, 1, -1, 1) = u_x u_y u_z. \tag{A.33}$$

Through the Gram-Schmidt procedure (A.27), these moments are orthogonalized and result in the transformation matrix

$$\mathbf{M} = \begin{bmatrix}
1 & 1 & 1 & 1 & 1 & 1 & 1 & 1 & 1 & 1 & 1 & 1 & 1 & 1 & 1 \\
-2 & -1 & -1 & -1 & -1 & -1 & -1 & 1 & 1 & 1 & 1 & 1 & 1 & 1 & 1 \\
16 & -4 & -4 & -4 & -4 & -4 & -4 & 1 & 1 & 1 & 1 & 1 & 1 & 1 & 1 \\
0 & 1 & -1 & 0 & 0 & 0 & 0 & 1 & -1 & 1 & -1 & 1 & -1 & -1 & 1 \\
0 & -4 & 4 & 0 & 0 & 0 & 0 & 1 & -1 & 1 & -1 & 1 & -1 & -1 & 1 \\
0 & 0 & 0 & 1 & -1 & 0 & 0 & 1 & -1 & 1 & -1 & -1 & 1 & 1 & -1 \\
0 & 0 & 0 & -4 & 4 & 0 & 0 & 1 & -1 & 1 & -1 & -1 & 1 & 1 & -1 \\
0 & 0 & 0 & 0 & 0 & 1 & -1 & 1 & -1 & -1 & 1 & 1 & -1 & 1 & -1 \\
0 & 0 & 0 & 0 & 0 & -4 & 4 & 1 & -1 & -1 & 1 & 1 & -1 & 1 & -1 \\
0 & 2 & 2 & -1 & -1 & -1 & -1 & 0 & 0 & 0 & 0 & 0 & 0 & 0 & 0 \\
0 & 0 & 0 & 1 & 1 & -1 & -1 & 0 & 0 & 0 & 0 & 0 & 0 & 0 & 0 \\
0 & 0 & 0 & 0 & 0 & 0 & 0 & 1 & 1 & 1 & 1 & -1 & -1 & -1 & -1 \\
0 & 0 & 0 & 0 & 0 & 0 & 0 & 1 & 1 & -1 & -1 & -1 & -1 & 1 & 1 \\
0 & 0 & 0 & 0 & 0 & 0 & 0 & 1 & 1 & -1 & -1 & 1 & 1 & -1 & -1 \\
0 & 0 & 0 & 0 & 0 & 0 & 0 & 1 & -1 & -1 & 1 & -1 & 1 & -1 & 1
\end{bmatrix}, \tag{A.34}$$

Applying $\boldsymbol{m}^{eq} = \boldsymbol{M}\boldsymbol{f}^{eq}$, the equilibrium moments are

$$\begin{array}{lll}
m_0^{eq} = 1 & m_5^{eq} = u_y & m_{10}^{eq} = u_y^2 - u_z^2 \\
m_1^{eq} = -2 + 3P + u^2 & m_6^{eq} = -\frac{7}{3}u_y & m_{11}^{eq} = u_x u_y \\
m_2^{eq} = 16 - 45P - 5u^2 & m_7^{eq} = u_z & m_{12}^{eq} = u_y u_z \\
m_3^{eq} = u_x & m_8^{eq} = -\frac{7}{3}u_z & m_{13}^{eq} = u_x u_z \\
m_4^{eq} = -\frac{7}{3}u_x & m_9^{eq} = 2u_x^2 - u_y^2 - u_z^2 & m_{14}^{eq} = 0.
\end{array} \tag{A.35}$$

A symbolic mathematical package is even more useful here than in the D2Q9 derivation.

The inverse of $\boldsymbol{M}$ is required for transformation back to velocity space.

$$\begin{bmatrix}
\frac{1}{15} & -\frac{1}{9} & \frac{2}{45} & 0 & 0 & 0 & 0 & 0 & 0 & 0 & 0 & 0 & 0 & 0 & 0 \\
\frac{1}{15} & -\frac{1}{18} & -\frac{1}{90} & \frac{1}{10} & -\frac{1}{10} & 0 & 0 & 0 & 0 & \frac{1}{6} & 0 & 0 & 0 & 0 & 0 \\
\frac{1}{15} & -\frac{1}{18} & -\frac{1}{90} & -\frac{1}{10} & \frac{1}{10} & 0 & 0 & 0 & 0 & \frac{1}{6} & 0 & 0 & 0 & 0 & 0 \\
\frac{1}{15} & -\frac{1}{18} & -\frac{1}{90} & 0 & 0 & \frac{1}{10} & -\frac{1}{10} & 0 & 0 & -\frac{1}{12} & \frac{1}{4} & 0 & 0 & 0 & 0 \\
\frac{1}{15} & -\frac{1}{18} & -\frac{1}{90} & 0 & 0 & -\frac{1}{10} & \frac{1}{10} & 0 & 0 & -\frac{1}{12} & \frac{1}{4} & 0 & 0 & 0 & 0 \\
\frac{1}{15} & -\frac{1}{18} & -\frac{1}{90} & 0 & 0 & 0 & 0 & \frac{1}{10} & -\frac{1}{10} & -\frac{1}{12} & -\frac{1}{4} & 0 & 0 & 0 & 0 \\
\frac{1}{15} & -\frac{1}{18} & -\frac{1}{90} & 0 & 0 & 0 & 0 & -\frac{1}{10} & \frac{1}{10} & -\frac{1}{12} & -\frac{1}{4} & 0 & 0 & 0 & 0 \\
\frac{1}{15} & \frac{1}{18} & \frac{1}{360} & \frac{1}{10} & \frac{1}{40} & \frac{1}{10} & \frac{1}{40} & \frac{1}{10} & \frac{1}{40} & 0 & 0 & \frac{1}{8} & \frac{1}{8} & \frac{1}{8} & \frac{1}{8} \\
\frac{1}{15} & \frac{1}{18} & \frac{1}{360} & -\frac{1}{10} & -\frac{1}{40} & -\frac{1}{10} & -\frac{1}{40} & -\frac{1}{10} & -\frac{1}{40} & 0 & 0 & \frac{1}{8} & \frac{1}{8} & \frac{1}{8} & -\frac{1}{8} \\
\frac{1}{15} & \frac{1}{18} & \frac{1}{360} & \frac{1}{10} & \frac{1}{40} & \frac{1}{10} & \frac{1}{40} & -\frac{1}{10} & -\frac{1}{40} & 0 & 0 & \frac{1}{8} & -\frac{1}{8} & -\frac{1}{8} & -\frac{1}{8} \\
\frac{1}{15} & \frac{1}{18} & \frac{1}{360} & -\frac{1}{10} & -\frac{1}{40} & -\frac{1}{10} & -\frac{1}{40} & \frac{1}{10} & \frac{1}{40} & 0 & 0 & \frac{1}{8} & -\frac{1}{8} & -\frac{1}{8} & -\frac{1}{8} \\
\frac{1}{15} & \frac{1}{18} & \frac{1}{360} & \frac{1}{10} & \frac{1}{40} & -\frac{1}{10} & -\frac{1}{40} & \frac{1}{10} & \frac{1}{40} & 0 & 0 & -\frac{1}{8} & -\frac{1}{8} & \frac{1}{8} & -\frac{1}{8} \\
\frac{1}{15} & \frac{1}{18} & \frac{1}{360} & -\frac{1}{10} & -\frac{1}{40} & \frac{1}{10} & \frac{1}{40} & -\frac{1}{10} & -\frac{1}{40} & 0 & 0 & -\frac{1}{8} & -\frac{1}{8} & \frac{1}{8} & \frac{1}{8} \\
\frac{1}{15} & \frac{1}{18} & \frac{1}{360} & -\frac{1}{10} & -\frac{1}{40} & \frac{1}{10} & \frac{1}{40} & \frac{1}{10} & \frac{1}{40} & 0 & 0 & -\frac{1}{8} & \frac{1}{8} & -\frac{1}{8} & -\frac{1}{8} \\
\frac{1}{15} & \frac{1}{18} & \frac{1}{360} & \frac{1}{10} & \frac{1}{40} & -\frac{1}{10} & -\frac{1}{40} & -\frac{1}{10} & -\frac{1}{40} & 0 & 0 & -\frac{1}{8} & \frac{1}{8} & -\frac{1}{8} & \frac{1}{8}
\end{bmatrix} \tag{A.36}$$

Again there are several conserved moments, m_0, m_3, m_5, and m_7, fixed density, x-, y-, and z-momentum, respectively. Also, there are moments related to viscosity/shear, m_{9-13}. Thus, conserved moment relaxation rates are non-specific, shear moments are fixed, and other moments can be tuned with freedom between 0 and 2 for stability.

Appendix B

Thermal D2Q4 LBE Derivations

B.1 Equilibrium Distribution Form: Ansatz Method

Assuming linearity based on the advection-diffusion equation, the form of g_i^{eq} takes,

$$g_i^{eq} = A + B(\boldsymbol{c}_i \cdot \boldsymbol{u}). \tag{B.1}$$

Calling on the first definition of B.12 and performing the summation of B.1,

$$A = \frac{T}{4}. \tag{B.2}$$

Introducing the flux summation,

$$\sum_{i=1}^{4} \boldsymbol{c}_i g_i^{eq} = \boldsymbol{u} T \Rightarrow g_1^{eq} - g_3^{eq} = u_x T, \tag{B.3}$$

resolves,

$$B = \frac{T}{2}, \tag{B.4}$$

yielding the final form:

$$g_i^{eq} = \frac{T}{4} \left[1 + 2(\boldsymbol{c}_i \cdot \boldsymbol{u}) \right]. \tag{B.5}$$

B.2 Chapman-Enskog Expansion for the Thermal D2Q4 LBE

As in Appendix A,

$$\epsilon \equiv Kn, \quad \epsilon^{-1}x_1 \Rightarrow \frac{\partial}{\partial x} = \epsilon\frac{\partial}{\partial x_1}, \quad \frac{\partial}{\partial t} = \epsilon\frac{\partial}{\partial t_1} + \epsilon^2\frac{\partial}{\partial t_2}. \tag{B.6}$$

Performing the perturbation expansion of g_i in terms of ϵ,

$$g_i(\boldsymbol{x},t) = g_i^{(0)}(\boldsymbol{x},t) + \epsilon g_i^{(1)}(\boldsymbol{x},t) + \epsilon^2 g_i^{(2)}(\boldsymbol{x},t) + \mathcal{O}(\epsilon^3), \quad g_i^{(0)} = g_i^{eq}, \tag{B.7}$$

and the Taylor series expansion of the LBE with g_i,

$$\begin{aligned}\frac{1}{\lambda}(g_i^{(0)} - g_i) = &\left(\frac{\partial}{\partial t} + \nabla_{\boldsymbol{x}}\cdot\boldsymbol{c}_i\right)g_i \\ &+ \frac{\Delta t}{2}\left[\frac{\partial}{\partial t}\left(\frac{\partial}{\partial t}\right) + 2\frac{\partial}{\partial t}(\nabla_{\boldsymbol{x}}\cdot\boldsymbol{c}_i) + (\nabla_{\boldsymbol{x}}\nabla_{\boldsymbol{x}}) : (\boldsymbol{c}_i\boldsymbol{c}_i)\right]g_i \\ &+ \mathcal{O}(\Delta t^2),\end{aligned} \tag{B.8}$$

and with expansions B.6,

$$\begin{aligned}\frac{1}{\lambda}(g_i^{(0)} - g_i) = &\left(\epsilon\frac{\partial g_i}{\partial t_1} + \epsilon^2\frac{\partial g_i}{\partial t_2}\right) + \epsilon(\nabla_{x_1}\cdot\boldsymbol{c}_i)g_i \\ &+ \frac{\Delta t}{2}\epsilon^2\left[\frac{\partial^2 g_i}{\partial t_1^2} + 2\frac{\partial}{\partial t_1}(\nabla_{x_1}\cdot\boldsymbol{c}_i)g_i + (\nabla_{\boldsymbol{x}}\nabla_{\boldsymbol{x}}) : [(\boldsymbol{c}_i\boldsymbol{c}_i)g_i]\right] \\ &+ \frac{\Delta t}{2}\epsilon^3\left[2\frac{\partial}{\partial t_1}\frac{\partial g_i}{\partial t_2} + 2\frac{\partial}{\partial t_2}(\nabla_{x_1}\cdot\boldsymbol{c}_i)g_i\right] + \frac{\Delta t}{2}\epsilon^4\left(\frac{\partial^2 g_i}{\partial t_2^2}\right) \\ &+ \mathcal{O}(\Delta t^2)\,.\end{aligned} \tag{B.9}$$

The first and second order terms of ϵ, respectively are:

$$-\frac{1}{\lambda}g_i^{(1)} = \frac{\partial g_i^{(0)}}{\partial t_1} + (\nabla_{x_1}\cdot\boldsymbol{c}_i)g_i^{(0)}, \quad \text{and} \tag{B.10}$$

$$\begin{aligned}-\frac{1}{\lambda}g_i^{(2)} = &\frac{\partial g_i^{(1)}}{\partial t_1} + (\nabla_{x_1}\cdot\boldsymbol{c}_i)g_i^{(1)} + \frac{\partial g_i^{(0)}}{\partial t_2} \\ &+ \frac{\Delta t}{2}\left[\frac{\partial^2 g_i^{(0)}}{\partial t_1^2} + 2\frac{\partial}{\partial t_1}\left(\nabla_{x_1}\cdot\boldsymbol{c}_i\right)g_i^{(0)} + (\nabla_{x_1}\nabla_{x_1}) : \left(\boldsymbol{c}_i\boldsymbol{c}_i g_i^{(0)}\right)\right].\end{aligned} \tag{B.11}$$

Introducing,

$$\sum_{i=1}^{4} g_i^{(0)} = T, \quad \text{and} \quad \sum_{i=1}^{4} g_i^{(G)} = 0 \quad \text{for} \quad G \neq 0, \tag{B.12}$$

applying summation over i, and utilizing B.10 in B.11 yields:

$$\frac{\partial T}{\partial t_1} + \boldsymbol{u} \cdot \nabla_{x_1} T = 0, \quad \text{and} \tag{B.13}$$

$$\frac{\partial T}{\partial t_2} + \left(1 - \frac{\Delta t}{2\lambda}\right) \nabla_{x_1} \cdot \Pi^{(1)} = 0, \tag{B.14}$$

where

$$\begin{aligned} \Pi^{(1)} &= \sum_{i=1}^{4} \boldsymbol{c}_i g_i^{(1)} \approx -\lambda \left(\frac{1}{2}\right) \nabla_{x_1} \left(\sum_{i=1}^{4} g_i\right) \\ &= \alpha \nabla_{x_1} T, \quad \alpha = \frac{1}{2}\left(\tau_T - \frac{1}{2}\right). \end{aligned} \tag{B.15}$$

Combining these last three results and reversing the scaling of B.6 forms the advection-diffusion temperature transport equation,

$$\frac{\partial T}{\partial t} + \boldsymbol{u} \cdot \nabla T = \alpha \nabla^2 T. \tag{B.16}$$

Appendix C

Units

Table C.1 establishes a datum for conversion to physical units, and table C.2 provides the conversion factors from solver units to physical meaning at any point in the domain for any value of interest. Material properties are based on air at $T = 573$ K, 100 nm PM, and cordierite substrate. Diffusivities are based on Pr (0.68) and Sc ($\approx$95.1) [127].

Below these tables are detailed derivations of the conversions to provide logic and justification for their values.

Table C.1
Possible simulation datum points for solver to physical unit conversion

Metric	Physical Unit	LB Unit
L_{filter}	200 μm	200
ν	$4.7559\text{E}-5$ m^2 s^{-1}	0.16667
ρ_0	0.6172 kg m^{-3}	1.0
T_{in}	573 K	0.01
α	$6.9940\text{E}-5$ m^2 s^{-1}	0.24559
D	$5.0\text{E}-7$ m^2 s^{-1}	0.0017522

Table C.2
Multipliers for solver to physical unit conversion

Physical Result	Multiplier
$L(\delta_x)$	$1.0\text{E}-6$ m
ν	$2.8535\text{E}-4$ m^2/s
$t(\delta_t)$	$3.5044\text{E}-9$ s
$\boldsymbol{u}$	285.35 m/s
ρ	0.6172 kg/m^3
P	50256.7 Pa
T	57300 K
α	$2.8535\text{E}-4$ m^2/s
D	$2.8535\text{E}-4$ m^2/s
κ	$1.0\text{E}-12$ m^2

As an additional note, filter PM loading density can be computed through multiplying the density of carbon black (380 kg/m^3) by the ratio of PM filled lattice cells to total filter lattice cells.

Conversion Derivations

In this section, variables labeled C_q represent the conversion factor for physical quantity q. Values with a tilde are lattice Boltzmann units.

In the filter simulations, viscosity, length, and τ all have established fixed values, and thus fixed conversions. With these datums, the time value conversion can be computed from

$$\frac{\nu}{\tilde{\nu}} = \frac{C_L^2}{C_t}, \tag{C.1}$$

and utilizing the relationship between $\tilde{\nu}$ and τ, C_t is found through

$$C_t = \frac{(\tau - \frac{1}{2})C_L^2}{3\nu}. \tag{C.2}$$

With C_L and C_t established, $C_{\boldsymbol{u}}$ can be defined as

$$C_{\boldsymbol{u}} = \frac{C_L}{C_t}. \tag{C.3}$$

Density is also fixed both in physical and lattice Boltzmann units, so the conversion is

$$C_\rho = \frac{\rho_0}{\tilde{\rho}}. \tag{C.4}$$

Pressure can be defined in terms of established conversion factors based on unit consistency:

$$[P] = \frac{N}{m^2} = \frac{kg}{m^3}\frac{m^2}{s^2} = \frac{[C_\rho][C_L^2]}{[C_t^2]}, \tag{C.5}$$

yielding

$$C_P = \frac{C_\rho C_L^2}{C_t^2}. \tag{C.6}$$

Temperature is independent of previously established units and conversions, so

$$C_T = \frac{T}{\tilde{T}}. \tag{C.7}$$

Using the equivalency of the dimensionless values Pr and Sc

$$\tilde{\alpha} = \frac{\tilde{\nu}}{Pr} \tag{C.8}$$

$$\tilde{D} = \frac{\tilde{\nu}}{Sc}, \tag{C.9}$$

yielding

$$C_\alpha = \frac{\alpha}{\tilde{\alpha}} \tag{C.10}$$

$$C_D = \frac{D}{\tilde{D}}. \tag{C.11}$$

Permability can be derived in a similar way as pressure,

$$[\kappa] = m^2 = [C_L^2], \tag{C.12}$$

yielding

$$C_\kappa = C_L^2. \tag{C.13}$$

PM loading measures the ratio of the mass of PM deposited to the total filter volume. Assuming unit thickness, as is standard in 2D CFD, the volume of PM deposits is computed as

$$(\#\text{filled cells}) \cdot C_L^3 \tag{C.14}$$

and the volume of the filter is

$$(\#\text{cells}) \cdot C_L^3. \tag{C.15}$$

Since the ratio is of interest, the conversion C_L^3 drops. The physical unit most common for filter loading is g/L, and no conversion is necessary from kg/m^3. Finally, the loading is computed by

$$\%\text{loading} \cdot \rho_{PM}. \tag{C.16}$$

Appendix D

Filter Pseudocode

function *Flag*

---

define L_{filter} //length of filtration area

define L_{inlet} //length of inlet area

define $\#_{seeds}$ //number of seed sites

define r_{min} //minimum radius

define r_{max} //maximum radius

for $a = 0$ to $\#_{seeds}$

generate random number *(1)* between L_{filter} and $L_{filter} + L_{inlet}$

generate random number *(2)* between 0 and N_y

generate random number *(3)* between r_{min} and r_{max}

generate random number *(4)* between r_{min} and r_{max}

for $i = 0$ to N_x

for $j = 0$ to N_y

compute ellipse where:

(1) is the x-position of the center

(2) is the y-position of the center

(3) is the first radius

(4) is the second radius

if i and j are within ellipse

node(i,j)="solid"

else

node(i,j)="fluid"

//Reset inlet and outlet areas to only fluid

for $i = 0$ to N_x

for $j = 0$ to N_y

if inlet or outlet area

node(i,j) = "fluid"

function *Boundary*

---

for $i = 0$ to N_x

for $j = 0$ to N_y

if it is a "fluid" node

"count" = 0

for $k = 1$ to number of lattice velocities

id = neighbor x-node along link

jd = neighbor y-node along link

if $jd < 0$

$jd = 0$

if $jd > N_y$

$jd = N_y$

if nodes(id, jd)="solid"

add 1 to the "count"

record node position and lattice link as broken

else

record node position and lattice link as unbroken

for $i = 0$ to N_x

for $j = 0$ to N_y

if it is a "solid" node

for $k = 1$ to number of lattice velocities

id = neighbor x-node along link

jd = neighbor y-node along link

if $jd < 0$

$jd = 0$

if $jd > N_y$

$jd = N_y$

if nodes(id, jd)="fluid"

mark as perimeter

else

mark as not a perimeter

function *Measure*

---

define A_{filter} //area of filtration area

define A_{pore} //pore space

define e //porosity

define P_f //filter perimeter

//Initialize

$A_{filter} = 0$

$A_{pore} = 0$

$P_f = 0$

for $i = L_{inlet}$ to $L_{filter} + L_{inlet}$

for $j = 0$ to N_y

add 1 to A_{filter}

if it is a "fluid" node

add 1 to A_{pore}

if it is a "perimeter" node

add 1 to P_f

$e = A_{pore}/A_{filter}$

Appendix E

Copyright Agreements and Permissions

Chapter 4 Reprint Permission

The *International Journal of Computational Engineering Research* requires agreement that the research work is original in nature, but not agreement in signing over reprint rights `http://www.ijceronline.com/copyright.html`. For clarity, the entirety of the author signed document is:

"I/we agree with the publishing policy of the **International Journal of Computational Engineering Research**. I/we understand that my manuscript contains

data, figures, photos, etc... in original and nothing has been plagiarized from the research work undertaken by any other person/author. I take full responsibility that this research work has not previously appeared elsewhere for publication and if found to be plagiarized in any way IJCER has full authority to declare it so without any intimation or prior notice and blacklist the authors."

Additionally, the journal makes the following statement about academic reproduction at `http://www.ijceronline.com/Ethics.html`:

"Journal does not view the following uses of work as prior publication: publication in the form of an abstract; **publication as an academic thesis**; publication as an electronic preprint." (emphasis mine)

Chapter 5 Reprint Permission

Copyright terms for authors published in *Advances in Applied Mathematics and Mechanics* can be found at `http://www.global-sci.org/aamm/` > "Instructions for Authors" > "Copyright Transfer Statement". Reprint policies allowing reproduction in this dissertation are described in the following section of that document:

"4. The Work may be reproduced by any means for educational and scientific purposes by the Author(s) or by others without fee or permission with the exception of

reproduction by services that collect fees for delivery of documents. The Author(s) may use part or all of this Work or its image in any further work of his/her (their) own. In any reproduction, the original publication by the Publisher must be credited in the following manner: "First published in [Publication] in [volume and number, or year], published by Global Science Press," and the copyright notice in proper form must be placed on all copies. Any publication or other form of reproduction not meeting these requirements will be deemed unauthorized."

Chapter 6 Reprint Permission

Copyright terms for authors published in *ASME Journal of Fluids Engineering* can be found at `http://journaltool.asme.org/Help/AuthorHelp/WebHelp/JournalsHelp.htm?_ga=2.63826031.1106457254.1503792097-1067151223.1494105592#Guidelines/Copyright_Transfer.htm`. Reprint policies allowing reproduction in this dissertation are described in the following section of that site:

"**RETAINED RIGHTS OF AUTHORS**

Authors retain all proprietary rights in any idea, process, procedure, or articles of manufacture described in the Paper, including the right to seek patent protection for them. Authors may perform, lecture, teach, conduct related research, display all or part of the Paper, and create derivative works in print or electronic format.